Estimation of Standard Model Effective Field Theory parameters in WZ leptonic decays using the ATLAS Detector

by

Juan Cristóbal Rivera Vergara
B.Sc., Pontificia Universidad Católica de Chile, 2015
M.Sc., Pontificia Universidad Católica de Chile, 2018

A Dissertation Submitted in Partial Fulfillment of the
Requirements for the Degree of

DOCTOR OF PHILOSOPHY

in the Department of Physics and Astronomy

We acknowledge and respect the Lək̓ʷəŋən (Songhees, Xʷsepsəm/Esquimalt) Peoples on whose territories the university stands, and the Lək̓ʷəŋən and W̱SÁNEĆ Peoples, whose historical relationships with the land continue to this day.

Estimation of SMEFT parameters in WZ leptonic decays using the ATLAS Detector

by

Juan Cristóbal Rivera Vergara
B.Sc., Pontificia Universidad Católica de Chile, 2015
M.Sc., Pontificia Universidad Católica de Chile, 2018

Supervisory Committee

Dr. R. McPherson, Supervisor
(Department of Physics and Astronomy)

Dr. I. Trigger, Inside Member
(Department of Physics and Astronomy & TRIUMF)

Dr. R. Keeler, Inside Member
(Department of Physics and Astronomy)

Dr. Cornelia Bohne, Outside Member
(Department of Chemistry)

ABSTRACT

The discovery of the Higgs boson in 2012 became the last missing piece to complete the puzzle of the Standard Model. While able to withstand an extensive array of precision tests, the model is still unable to explain some crucial observed phenomena in the universe, such as dark matter, gravity, and baryon asymmetry. Various theories that extend the Standard Model while seeking to answer some of these questions have been proposed; among these is the Standard Model Effective Field Theory (SMEFT), that assumes the Standard Model to be an effective theory only applicable up to energies not exceeding a certain scale. This theory includes six-dimensional terms in the Lagrangian, which would affect various SM processes. The ATLAS experiment at the Large Hadron Collider was constructed to seek signs of physics beyond the Standard Model, using the data from high energy proton-proton collisions. The extra terms proposed by SMEFT would affect various processes observed in the Standard Model, resulting in small differences in kinematic and angular observables, and those differences could be measured in the events produced at ATLAS. In particular, this dissertation focuses on a set of terms that would affect the electro-weak sector of the SM, and aims to make use of angular distributions to better observe the effects on the spin and polarization of the particles. New physics is not observed, and limits are set for the values of the relevant SMEFT parameters, which were found to be consistent with SM values.

Contents

List of Tables

List of Figures

DEDICATION

To my parents, who've supported me all the way.

PREFACE

After I received my MSc. in Physics in Chile in 2018, I moved to Canada to start this PhD. I knew that I wanted my research to focus on something that would help us understand better the Standard Model and its limitations, so that's how with the help of my supervisors we settled on an analysis of the triple gauge coupling WWZ decaying into leptons, in the context of the 6-dimensional effective field theory for weak boson pair production, also called *EWdim6*. This is considered to be a somewhat niche model, and after about a year of working with it, it became clear that if we wanted to be able to collaborate with other groups and compare results, we would have to switch to the more popular model called "SMEFT". This expanded the scope of the research from 5 parameters to over 20, but we ended up bringing it down to a more manageable 12 parameters. Also during this time most of my simulated samples were being generated using a reweighting method, which had started to show some problems related to the extrapolation of the samples, so we switched to the so-called decomposition method, explained in chapter 4. In 2020 I moved to CERN to help with the integration and commissioning of the ATLAS New Small Wheel. This served as a continuation of the work I did during my MSc in the production and testing of the Chilean QS1 modules for the New Small Wheel. In that same year, just a few months after I had moved, the COVID pandemic broke out in the world, which shut down work and travel in most places. While this slowed down most types of work, the commissioning of the NSW took this as a blessing in disguise, since the project was already late at that point, so this came as an opportunity to catch up while other types of work were stopped. So for most of the pandemic, I worked mostly on the commissioning of wheels A and C, by connecting hundreds of fiber cables, running pulser tests, and even learning how to operate a cherry-picker crane. During my last few months at CERN I worked inside the ATLAS cavern, helping with the integration of both wheels into the ATLAS detector. In the 2 years I lived in Europe most of my time was dedicated to working on the NSW project, which unfortunately slowed down a bit the progress of my own research, so after I moved back to Canada in 2022 I dedicated 100% of my time to work on this dissertation. This included some aspects that would end up being abandoned, but that still taught me a lot, such as trying to program my own reconstruction framework, using Legendre polynomials to perform the fits, attempting to use the decomposition method alongside NLO production of SMEFT samples, among others.

The following list outlines the contributions from me and other people to this analysis:

- I was responsible for the production of the simulated LO SMEFT MC samples used in this analysis, where both truth samples and detector-simulated samples were produced.
- The NNLO QCD and NLO electroweak corrections for the SM sample were implemented by José Pretel.
- I implemented a framework to analyze the detector-simulated SMEFT samples to check for consistency with the existing LAPP framework. My framework did not end up being used, as the analysis evolved to use truth samples compared with unfolded data.
- The decomposition validation studies and the shape analysis studies were done by me.
- The EFT-fun framework was made by the multiboson group, and the script used in this analysis was made by Joseph Lambert.
- The fits use unfolded distributions that come from published HEPdata.

All figures that do not have a citation in the caption were made by me. Figures with citations are available under CC-BY licenses, or follow the terms of use for CERN audiovisual media, with the exception of Figure 3.8, which has been reproduced in this dissertation with the permission of IOP Publishing.

ACKNOWLEDGEMENTS

This dissertation would not have been possible without the help of many wonderful people who I met over the past few years. First, I'd like to thank my supervisors, Rob, Isabel and Richard. I don't think I would have been able to finish this dissertation without your guidance. I'd also like to thank the rest of the TRIUMF/UVic WZ group, Maheyer, Leesa, Joseph and José. Thank you for the helpful discussions, for assisting me with coding, and more.

I'd like to thank the people at the TRIUMF ATLAS office, Evan, Marco, Elena, Callum, Matt, Kelvin, and Emily, as well all as the people from GAPS. Thank you for keeping me company and making TRIUMF a fun place to work at.

I'd also like to thank the people I worked with during my stay at CERN, Gerardo, Orianne, John, Henso, Olesia, Charly, Roberto, JP, Matías, Nicolás, Rimsky, and many more. Thank you for helping me contribute to such a big project as was the ATLAS New Small Wheel.

I'd like to thank my roommates, Katie, Thomas and Michael. Thank you for giving me a home and family in a foreign country.

I'd like to thank all my friends back in Chile, for keeping in contact with me, playing video games with me, and for keeping me from forgetting how to speak Spanish.

Finally, I'd like to thank my family: my parents, my sisters, my grandparents, and everyone else, thank you for your continued support.

1 Introduction

The Standard Model of particle physics describes all the known particles of the universe and their interactions. Developed throughout the second half of the 20th century, it was slowly expanded to include more phenomena as science progressed, and by the 1970s it had taken its current mathematical form. It would still take decades to discover all the particles predicted by it, ending with the discovery of the Higgs boson in 2012. As it stands, most aspects of the model have been confirmed using high-energy particle accelerators, and while it manages to explain a multitude of phenomena, it still falls short of being a theory of everything. Most notably, gravity, one of the four fundamental forces in the universe, is unaccounted for. In addition to that, there are many other unanswered problems that the model does not address, like the asymmetry of matter and antimatter in the universe, dark energy and dark matter, and the nature of the mass of neutrinos, just to name a few. In an effort to answer these problems, physicists have come up with a multitude of theories that expand on the Standard Model, keeping what works, but adding new mechanisms, particles, interactions, or dimensions, in order to solve the existing issues and to hopefully end up with a real theory of everything. These new theories are then tested against the data collected from various experiments around the world, and then they are adjusted or discarded depending on the results.

This dissertation focuses on one such model, the Standard Model Effective Field Theory, or SMEFT, and in an estimate of some of the parameters of the model based on data from the ATLAS detector at the LHC. Chapter 2 will introduce the theoretical framework of the study, where first the Standard Model, and all the known particles and interactions are explored. Then SMEFT is introduced, which does not explicitly add any new particles, but new interactions between the existing SM particles. Special attention is given to the aspects of the model that affect the $WZ \to \ell\nu\ell\ell$ process, the main focus of this study.

Chapter 3 describes CERN, the Large Hadron Collider, and the ATLAS Experiment, which are used to accelerate protons to speeds close to the speed of

light, collide them, and collect the data from the resulting events. This chapter also describes in detail the subsystems of ATLAS and their functions, in addition to a brief exploration of the phenomenology of proton-proton collisions.

Chapter 4 describes the various data and simulation samples used in the study. The various stages of the the simulation are explained, going from the initial matrix element calculation, to the parton shower, detector simulation, and reconstruction. This chapter also introduces the so-called decomposition method, where the terms of the SMEFT samples are simulated independently, to be then rescaled and recombined to obtain new valid samples at various values of the corresponding SMEFT parameters.

Chapter 5 describes how the data is processed, in what is called the object and event selection. The different types of signals measured in the detectors are reconstructed into objects depending on their characteristics, giving as a result an approximation of what the event really looked like inside the detector. Afterwards, selection cuts are applied to the reconstructed particles to preserve the events that match the event of interest, and to discard events that might be background.

Chapter 6 describes the various sources of systematic uncertainties that affect the data. Experimental uncertainties include the uncertainty in the measurements of various particle types, as well as luminosity and pileup uncertainty. Theoretical uncertainties come from the renormalization and factorization scales, the uncertainties in the PDF modeling, and uncertainties in the value of physical constants used in the analysis.

Chapter 7 goes into the statistical analysis used in the study. The statistical model used to describe the data, and the likelihood function used to fit the data to the model, are explained. Finally, a profile likelihood test is used to estimate confidence intervals for the values of the SMEFT parameters based on the previous fits.

Chapter 8 discusses the results obtained in the study. For each of the 12 SMEFT parameters studied, 4 fits are performed, using 4 different observables, resulting in 4 best-fit values, each with their corresponding confidence intervals.

Chapter 9 concludes this dissertation, summarizing the results and discussing the future of SMEFT studies at CERN.

2 Theoretical framework

2.1 The Standard Model of Particle Physics

The Standard Model (SM) of particle physics is the most widely accepted model in the scientific community to explain the phenomena of the sub-atomic scale. Developed during the second half of the 20th century, it describes three of the four known fundamental forces, and it classifies all known elementary particles and their interactions.

2.1.1 SM fields

All known matter in the universe is made up of particles. If one were to divide matter into its smallest, most fundamental ingredients, we would reach what we call elementary or fundamental particles. At this scale, conventional physics breaks down, and particles can behave in non-intuitive ways, like appearing to be in two places at the same time, or having their allowed energies quantized. The theoretical framework commonly used to explain these and other phenomena is Quantum Field Theory (QFT). In QFT's, the fundamental objects are quantum fields that permeate all space, and the particles are excitations of the corresponding field (as such, we may sometimes refer to field and particle interchangeably). The SM in particular, is a mixture of several QFTs. The fundamental fields of the SM are classified into different types: fermions, gauge fields, and the Higgs boson, and are summarized in Figure 2.1.

Fermions

Fermions are the particles that make up visible matter. Their defining characteristic is that they have a spin of 1/2, and thus follow Fermi-Dirac statistics [2]. And

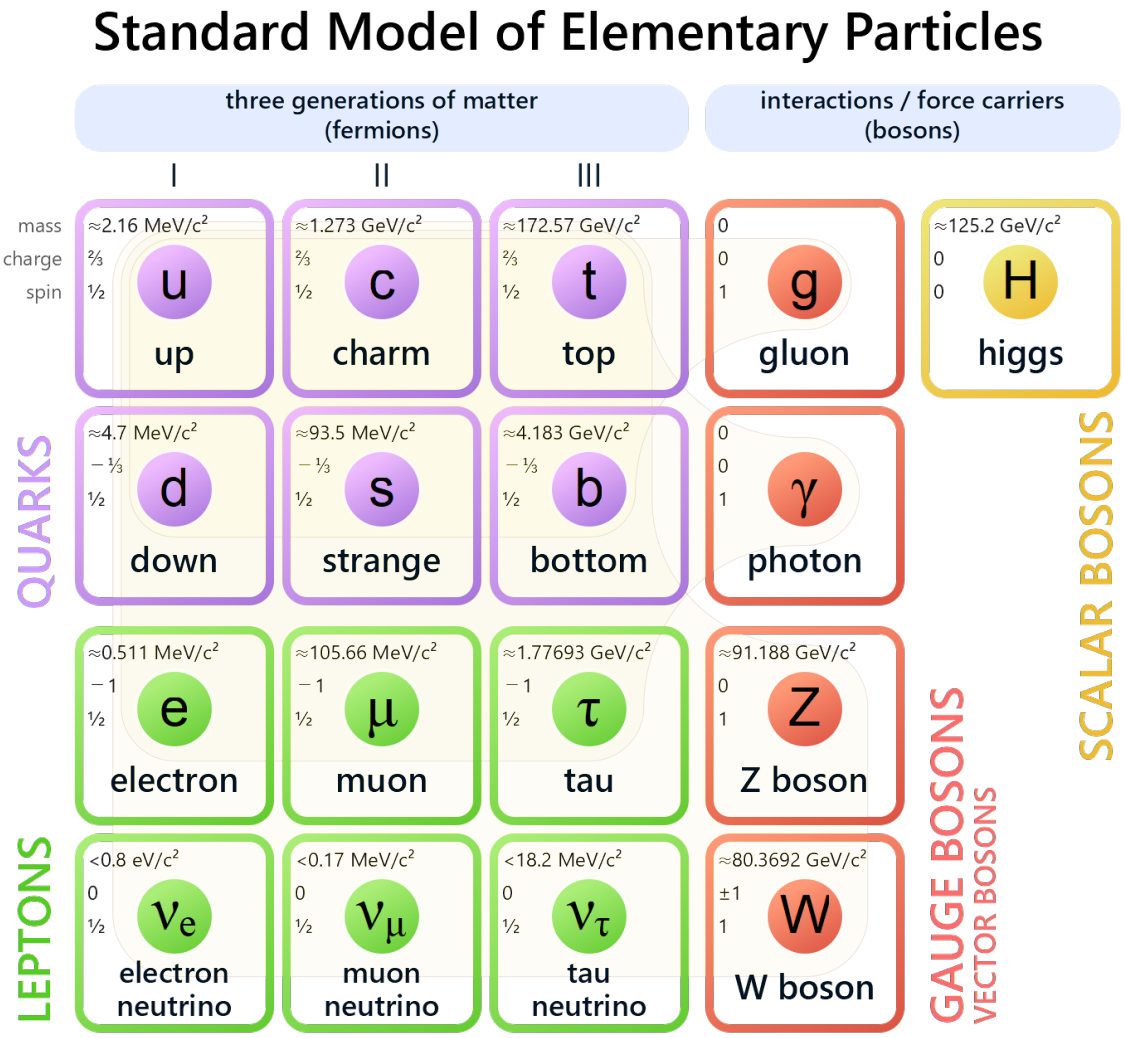

Figure 2.1: The particles of the SM [1]

even though they are not shown in the figure, each fermion has an anti-particle equivalent, usually denoted with a bar over their symbol (e.g., an anti-up quark is $\bar{u}$). They have the same mass and spin as the normal particles, but opposite charges and helicity. The fermions can be subdivided further into two categories: quarks and leptons.

Quarks Quarks are most commonly found in the nuclei of atoms. They have color charge, weak isospin, and electromagnetic charge, meaning they feel all 3 fundamental forces described by the SM. They obey color-confinement, meaning

they can never be observed individually, and can only exist as a mixture forming colorless objects, known as hadrons. Groups of two quarks (quark anti-quark pair) are called mesons, such as pions or kaons, while groups of three quarks are called baryons, like the proton and neutron. Groups or 4 or more are very rare and unstable, and are only produced in extreme conditions. Quarks are divided into 3 generations, where the masses of the particles in each generation are a few orders of magnitude larger than the masses of the previous one.

Quark	**Symbol**	**Q**	**T_3**	**Mass**
First generation				
up	u	+2/3	+1/2	2.16 ± 0.04 MeV
down	d	-1/3	-1/2	4.70 ± 0.04 MeV
Second generation				
charm	c	+2/3	+1/2	1.2730 ± 0.0028 GeV
strange	s	-1/3	-1/2	93.5 ± 0.5 MeV
Third generation				
top	t	+2/3	+1/2	172.56 ± 0.31 GeV
bottom	b	-1/3	-1/2	4.183 ± 0.004 GeV

Table 2.1: Quarks and their corresponding symbol, charge (Q), isospin (T_3) and mass [3].

Leptons Unlike the quarks, the leptons do not have color charge, so they are not confined to the nuclei of atoms. The are also divided into 3 generations, where each generation has an electromagnetically charged lepton, and an associated neutral one, called the neutrino. The charged leptons feel the electromagnetic and the weak nuclear force, while the neutrinos interact only through the weak force. This makes them very hard to measure, since they tend to pass through matter completely unimpeded. Large tanks filled with water, heavy water or other materials and lined with phototubes can be used to measure a tiny fraction of them, even though on Earth, the neutrinos from the Sun flow at a rate of around 70 billion per cm^2 per second.

Lepton	Symbol	Q	T_3	Mass
First generation				
electron	e	-1	-1/2	0.51099895000 ± 0.00000000015 MeV
electron neutrino	ν_e	0	+1/2	< 0.8 eV
Second generation				
muon	μ	-1	-1/2	105.6583755 ± 0.0000023 MeV
muon neutrino	ν_μ	0	+1/2	< 0.19 MeV
Third generation				
tau	τ	-1	-1/2	1776.93 ± 0.09 MeV
tau neutrino	ν_τ	0	+1/2	< 18.2 MeV

Table 2.2: Leptons and their corresponding symbol, charge, isospin and mass [3].

Gauge fields

The gauge fields are the particles that mediate the forces of the SM. They are a product of the symmetries of the SM: the symmetry group of the SM is $SU(3)_C \times SU(2)_L \times U(1)_Y$, which introduces 3 vector gauge fields:

- The G_μ field arises from the $SU(3)_C$ symmetry. The particles associated with this field are called Gluons, and they are the mediators of the strong nuclear force.
- The W_μ field arises from the $SU(2)_L$ symmetry. This field however, is not the physical field that is observed in nature, but it participates in the Spontaneous Symmetry Breaking (SSB) of the $SU(2) \times U(1)$ symmetry of the SM, which generates the fields that are actually responsible for the remaining SM forces.
- The B_μ field arises from the $U(1)$ symmetry. This field mixes with the W_μ after SSB and generates the physical fields of the model.

For completeness' sake, we will also introduce the physical fields that emerge after SSB:

- The $W_\mu^\pm$ fields correspond to the charged particles that mediate the weak nuclear force, and they are involved in weak charged current interactions, such as neutrino absorption/emission, or quark flavor change.

- The Z^0_μ field is the neutral mediator of the weak force. Since it has no charge, it only participates in weak neutral current interactions, which only change spin, momentum or energy, but leave the other quantum numbers (charge, flavor, baryon number, lepton number, etc) unchanged.
- The γ, or photon, is a neutral, massless field, and the mediator of the electromagnetic force.

Boson	**Symbol**	**Q**	**T_3**	**Mass**
Gluon	g	0	0	0
W	$W^\pm$	±1	±1	80.3692 ± 0.0133 GeV
Z	Z^0	0	0	91.1880 ± 0.0020 GeV
Photon	γ	0	0	$< 1 \times 10^{-18}$ eV

Table 2.3: Bosons and their corresponding symbol, charge, isospin and mass [3].

Higgs field

The Higgs field (H) is the only elementary scalar field of the SM. It is a complex doublet, with two charged and two neutral components. Its potential has non-zero minima, which introduces a spontaneous symmetry breaking, turning the two charged and one of the neutral components into Goldstone Bosons, which are then absorbed by the W_μ fields, giving them mass. The remaining neutral component is the only physical field that remains, and is commonly known as the Higgs Boson, denoted by h.

Boson	**Symbol**	**Q**	**T_3**	**Mass**
Higgs	h	0	0	125.20 ± 0.11 GeV

Table 2.4: Higgs boson and its corresponding symbol, charge, isospin and mass [3].

2.1.2 SM Lagrangian

Now that we know the fields of the SM, we can start to build the SM Lagrangian. This Lagrangian will describe not only the kinematics of the particles, but also

the interactions between them. This is because each term in a Lagrangian is associated with a process described by the theory. As an example, the Lagrangian of Quantum Electrodynamics (QED) is:

$$\mathcal{L}_{QED} = -\frac{1}{4}F_{\mu\nu}F^{\mu\nu} + i\bar{\psi}\gamma^{\mu}\partial_{\mu}\psi - e\bar{\psi}\gamma^{\mu}A_{\mu}\psi - m\bar{\psi}\psi \tag{2.1}$$

Looking at the fields in each term can tell us a bit about what each term represents. The first term is the kinetic term of the photon, while the second term is the kinetic term of the electron. The third term on the other hand, is the coupling of the photon and a positron-electron pair, while the last term is the mass term of the electrons. The SM Lagrangian is more complicated, but it follows the same principle: when fully expanded, each term will be associated with a particle or process allowed by the SM. The following sections are roughly based on the textbook "*An Introduction to Quantum Field Theory*", by Peskin and Schroeder [4].

Gauge Lagrangian

Let's start with the gauge fields. For the $SU(3)_C$ group, we can define the field strength $G^a_{\mu\nu}$ as:

$$G^a_{\mu\nu} = \partial_{\mu}G^a_{\nu} - \partial_{\nu}G^a_{\mu} + g_S f^{abc}G^b_{\mu}G^c_{\nu} \qquad (a = 1, ..., 8) \tag{2.2}$$

where f^{abc} are the group structure constants of $SU(3)$, which satisfy:

$$[T^a, T^b] = if^{abc}T^c \tag{2.3}$$

where T^a are the generators of the group. In the SM, $T^a = \frac{\lambda^a}{2}$, where λ^a are the Gell-Mann matrices. Similarly, we can define a field strength for the $SU(2)$ group:

$$W^a_{\mu\nu} = \partial_{\mu}W^a_{\nu} - \partial_{\nu}W^a_{\mu} + g\epsilon^{abc}W^b_{\mu}W^c_{\nu} \qquad (a = 1, 2, 3) \tag{2.4}$$

where ϵ^{abc} is the 3-dimensional Levi-civita symbol. And finally we define a field strength for the $U(1)$ group:

$$B_{\mu\nu} = \partial_{\mu}B_{\nu} - \partial_{\nu}B_{\mu} \tag{2.5}$$

With the field strengths we can construct the first term of the SM Lagrangian: a kinetic term for the gauge fields:

$$\mathcal{L}_{Gauge} = -\frac{1}{4}G^a_{\mu\nu}G^{\mu\nu a} - \frac{1}{4}W^a_{\mu\nu}W^{\mu\nu a} - \frac{1}{4}B_{\mu\nu}B^{\mu\nu} \tag{2.6}$$

While this term is usually treated as the kinetic term for the gauge fields, the definitions of the strength tensors add extra terms for gauge self interaction in the case of massive bosons and gluons, adding triple and quartic gauge couplings.

Fermion Lagrangian

In order to write terms for the fermions, we first must define the covariant derivatives of their symmetry groups. Let's start with the covariant derivative of the $SU(3)$ group:

$$D^{SU(3)}_\mu = (\partial_\mu - ig_s G^a_\mu T^a) \tag{2.7}$$

Here, we once again have the T^a generators of the group, the Gell-Mann matrices ($T^a = \frac{\lambda^a}{2}$). Next, the covariant derivative of the $SU(2)$ group:

$$D^{SU(2)}_\mu = (\partial_\mu - igW^a_\mu T^a) \tag{2.8}$$

Where this time the generators of the group T^a correspond to the Pauli matrices ($T^a = \frac{\sigma^a}{2}$). Finally, the covariant derivative of the $U(1)$ group is:

$$D^{U(1)}_\mu = (\partial_\mu - ig'YB_\mu) \tag{2.9}$$

Where $Y = Q - T_3$ is the hypercharge of the field.

Now that we know the covariant derivatives for the groups, we can construct the total covariant derivative for each field type, depending on how that particle transforms. We can start with the quarks, which transform under all 3 groups: $SU(3)\times SU(2)\times U(1)$. However, we must remember that the SM is a chiral theory: any fermion field ψ can be divided into its left and right handed components ($\psi = \psi_L + \psi_R$), where $\psi_{L,R} = \frac{1\pm\gamma^5}{2}\psi$. These fields interact differently from each other, and in the SM in particular, only left handed fermions couple to the W bosons. This means that the total covariant derivative of the left handed quarks will be:

$$D^{q_L}_\mu = (\partial_\mu - ig_s G^a_\mu T^a_{SU(3)} - igW^a_\mu T^a_{SU(2)} - ig'YB_\mu) \tag{2.10}$$

Whereas the total covariant derivative of the right handed quarks is:

$$D_\mu^{q_R} = (\partial_\mu - ig_s G_\mu^a T_{SU(3)}^a - ig'YB_\mu) \tag{2.11}$$

This leaves the quark term as:

$$\mathcal{L}_{Quark} = \sum_{Q_L} i\bar{Q}_L \gamma^\mu D_\mu^{q_L} Q_L + \sum_{u_R} i\bar{u_R}\gamma^\mu D_\mu^{q_R} u_R + \sum_{d_R} i\bar{d}_R \gamma^\mu D_\mu^{q_R} d_R \tag{2.12}$$

Where we have paired the left handed quarks as a doublet $Q_L = \binom{u}{d}_L$, leaving the right handed quarks as singlets u_R and d_R, for reasons that will become apparent later. When fully expanded, this term includes the kinetic term for the quarks, as well as their couplings to the gluons, the $W^\pm$ and Z^0 fields, and to the photon. Moving on to the leptons, we once again run into chirality. The left handed leptons transform under $SU(2) \times U(1)$, which means that their total covariant derivative is:

$$D_\mu^{\ell_L} = (\partial_\mu - igW_\mu^a T_{SU(2)}^a - ig'YB_\mu) \tag{2.13}$$

Whereas the total covariant derivative of the right handed leptons is simply:

$$D_\mu^{\ell_R} = (\partial_\mu - ig'YB_\mu) \tag{2.14}$$

This leaves the lepton term as:

$$\mathcal{L}_{Lepton} = \sum_{L_L} i\bar{L_L}\gamma^\mu D_\mu^{\ell_L} L_L + \sum_{\ell_R} i\bar{\ell_R}\gamma^\mu D_\mu^{\ell_R} \ell_R \tag{2.15}$$

Where we have paired the left handed leptons and neutrinos as a doublet $L_L = \binom{\nu}{\ell}_L$, leaving the right handed lepton as a singlet ℓ_R, similar to the quark case. When fully expanded, this term includes the kinetic term for the leptons, as well as their couplings to the $W^\pm$, Z^0, and to the photon.

Higgs Lagrangian and Spontaneous Symmetry Breaking

Let us write the Higgs part of the SM lagrangian:

$$\mathcal{L}_H = (D_\mu H)^\dagger (D^\mu H) - V(H) \tag{2.16}$$

Where $H = \binom{\varphi^+}{\varphi^0}$ is a complex scalar doublet, $D_\mu H$ is the covariant derivative of the doublet under the $SU(2) \times U(1)$ gauge symmetry:

$$D_\mu H = \left(\partial_\mu - \frac{ig}{2} W_\mu^a \sigma^a - \frac{ig'}{2} B_\mu\right) H \tag{2.17}$$

And the potential $V(H)$ has the form:

$$V(H) = -\mu^2 H^\dagger H + \lambda (H^\dagger H)^2 \tag{2.18}$$

This means that the field has degenerate minima at:

$$H_0 = \langle 0|H|0\rangle = \frac{e^{i\theta}}{\sqrt{2}} \begin{pmatrix} 0 \\ v \end{pmatrix} \tag{2.19}$$

Where $v = \sqrt{\mu^2/\lambda}$ and $e^{i\theta}$ is a random phase. Let's reparametrize the complex scalar doublet (which has 4 degrees of freedom) into 4 real scalar fields, α^a (with $a = 1, 2, 3$) and h:

$$H = \begin{pmatrix} \varphi^+ \\ \varphi^0 \end{pmatrix} = \frac{1}{\sqrt{2}} e^{i\sigma^a \alpha^a / 2v} \begin{pmatrix} 0 \\ v + h \end{pmatrix} \tag{2.20}$$

We want to get rid of the a^a fields and leave only the H field, which we can do by doing the unitary SU(2) transformation:

$$U(\alpha) = e^{-i\sigma^a \alpha^a / 2v} \tag{2.21}$$

The fields will transform as follows:

$$H \to H' = U(\alpha) H = \frac{1}{\sqrt{2}} \begin{pmatrix} 0 \\ v + h \end{pmatrix} \tag{2.22}$$

$$\vec{\mathbf{W}}_\mu \to \vec{\mathbf{W}}'_\mu = U(\alpha) \vec{\mathbf{W}}_\mu U^\dagger(\alpha) - \frac{i}{g} \big(\partial_\mu U(\alpha)\big) U^\dagger(\alpha) \tag{2.23}$$

$$B_\mu \to B'_\mu = B_\mu \tag{2.24}$$

Where $\vec{\mathbf{W}}_\mu = \frac{1}{2} W^a_\mu \sigma^a$. With this, the covariant derivative transforms as:

$$\begin{aligned} D_\mu H &= \big(\partial_\mu - ig \vec{\mathbf{W}}'_\mu - \frac{ig'}{2} B'_\mu\big) H' \\ &= (\partial_\mu U) H + U(\partial_\mu H) - igU \vec{\mathbf{W}}_\mu \cancel{U^\dagger U} H + ig \frac{i}{g} (\partial_\mu U) \cancel{U^\dagger U} H - \frac{ig'}{2} B'_\mu U H \\ &= \cancel{(\partial_\mu U) H} + U(\partial_\mu H) - U \frac{ig}{2} W^a_\mu \sigma^a H - \cancel{(\partial_\mu U) H} - U \frac{ig'}{2} B_\mu H \\ &= U\big(\partial_\mu - \frac{ig}{2} W^a_\mu \sigma^a - \frac{ig'}{2} B_\mu\big) H = U D_\mu H = U D_\mu U^\dagger H' \equiv D'_\mu H' \end{aligned}$$

We can see that the first term of the Higgs lagrangian is unchanged:

$$(D_\mu H)^\dagger (D_\mu H) \to (D'_\mu H')^\dagger (D'_\mu H') = (U D_\mu \cancel{U^\dagger U} H)^\dagger (U D_\mu \cancel{U^\dagger U} H)$$

$$= (D_\mu H)^\dagger \cancel{U^\dagger U} D_\mu H = (D_\mu H)^\dagger (D_\mu H)$$

Also, since the potential $V(H)$ is only dependent on terms of the form $O(H^\dagger H)$, it is also conserved, since:

$$H^\dagger H \to (H')^\dagger H' = (UH)^\dagger UH = H^\dagger \cancel{U^\dagger U} H = H^\dagger H$$

After the unitary transform, it becomes easier for us to calculate the first term of the lagrangian (from now on we will omit the prime symbol in the fields):

$$\begin{aligned}
(D_\mu H)^\dagger (D^\mu H) &= \left(\partial_\mu H^\dagger + \frac{ig}{2} W^a_\mu H^\dagger \sigma^a + \frac{ig'}{2} B_\mu H^\dagger\right)\left(\partial^\mu H - \frac{ig}{2} W^{b\mu} \sigma^b H - \frac{ig'}{2} B^\mu H\right) \\
&= (\partial_\mu H^\dagger)(\partial^\mu H) - \frac{ig}{2} W^{\mu a}(\partial_\mu H^\dagger \sigma^a H) - \frac{ig'}{2} B^\mu (\partial_\mu H^\dagger H) + \frac{ig}{2} W^a_\mu (H^\dagger \sigma^a \partial^\mu H) \\
&\quad + \frac{g^2}{4} W^a_\mu W^{b\mu} (H^\dagger \sigma^a \sigma^b H) + \frac{gg'}{4} W^a_\mu B^\mu (H^\dagger \sigma^a H) + \frac{ig'}{2} B_\mu (H^\dagger \partial^\mu H) \\
&\quad + \frac{gg'}{4} W^{\mu a} B_\mu (H^\dagger \sigma^a H) + \frac{g'^2}{4} B_\mu B^\mu (H^\dagger H) \\
&= (\partial_\mu H^\dagger)(\partial^\mu H) + \frac{g^2}{4} W^a_\mu W^{b\mu} (H^\dagger \sigma^a \sigma^b H) + \frac{gg'}{2} W^a_\mu B^\mu (H^\dagger \sigma^a H) + \frac{g'^2}{4} B_\mu B^\mu (H^\dagger H) \\
&= \frac{1}{2}(\partial_\mu h)(\partial^\mu h) + \left(\frac{g^2}{8}\left((W^1)^2 + (W^2)^2 + (W^3)^2\right) - \frac{gg'}{4} W^3 B + \frac{g'^2}{8} B^2\right)(v^2 + 2vh + h^2)
\end{aligned}$$

We can now isolate the mass terms of the bosons (i.e. terms that are quadratic in the fields), which we can see are:

$$\begin{aligned}
\mathcal{L}_{mass} &= \frac{g^2 v^2}{8}\left((W^1)^2 + (W^2)^2 + (W^3)^2\right) - \frac{gg' v^2}{4} W^3 B^\mu + \frac{g'^2 v^2}{8} B^2 \\
&= \frac{v^2}{8}\left(g^2 (W^1)^2 + g^2 (W^2)^2 + (gW^3 - g'B)^2\right)
\end{aligned}$$

Here we can introduce a few redefinitions. First, let's redefine the W^1 and W^2 fields as charged fields, where:

$$W^\pm = \frac{W^1 \mp iW^2}{\sqrt{2}}$$

This results in the first two terms of the equation adding up: $\frac{g^2 v^2}{8}\left((W^1)^2 + (W^2)^2\right) = \frac{g^2 v^2}{4} W^+ W^-$, meaning that the W bosons end up with a mass of $m_W = \frac{1}{2} g v$.

For the remaining terms we have a mixed one (with W^3B), which we will need to diagonalize. To do that we write it in matrix form:

$$\frac{v^2}{8}\begin{pmatrix} W^3_\mu & B_\mu \end{pmatrix}\begin{pmatrix} g^2 & -gg' \\ -gg' & g^2 \end{pmatrix}\begin{pmatrix} W^{3\mu} \\ B^\mu \end{pmatrix}$$

this can be diagonalized into:

$$= \frac{v^2}{8}\begin{pmatrix} Z_\mu & A_\mu \end{pmatrix}\begin{pmatrix} g^2+g'^2 & 0 \\ 0 & 0 \end{pmatrix}\begin{pmatrix} Z^\mu \\ A^\mu \end{pmatrix} = \frac{v^2}{8}(g^2+g'^2)Z_\mu Z^\mu$$

where

$$\begin{pmatrix} Z^\mu \\ A^\mu \end{pmatrix} = \begin{pmatrix} \cos\theta_W & -\sin\theta_W \\ \sin\theta_W & \cos\theta_W \end{pmatrix}\begin{pmatrix} W^{3\mu} \\ B^\mu \end{pmatrix}$$

with $\cos\theta_W = \frac{g}{\sqrt{g^2+g'^2}}$ and $\sin\theta_W = \frac{g'}{\sqrt{g^2+g'^2}}$. This leaves us with a massive neutral vector boson Z of mass $m_Z = \frac{m_W}{\cos\theta_W} = \frac{1}{2}v\sqrt{g^2+g'^2}$, and a massless neutral boson A_μ, which we identify with the photon.

$$\mathcal{L}_{mass} = \frac{1}{2}m_W^2 W^+_\mu W^{\mu-} + \frac{1}{2}m_Z^2 Z_\mu Z^\mu \tag{2.25}$$

The remaining terms of the covariant derivative are the kinetic term of the h field $\left(\frac{1}{2}(\partial_\mu h)(\partial^\mu h)\right)$, and the couplings of the gauge bosons to it. Adding them all together we get all the terms coming from the covariant derivative:

$$\begin{aligned}\mathcal{L}_{DH} =& \frac{1}{2}(\partial_\mu h)(\partial^\mu h) + \frac{1}{2}m_W^2 W^+_\mu W^{\mu-} + \frac{1}{2}m_Z^2 Z_\mu Z^\mu + \frac{m_W^2}{v}W^+_\mu W^{\mu-}h \\ &+ \frac{m_Z^2}{v}Z_\mu Z^\mu h + \frac{m_W^2}{2v^2}W^+_\mu W^{\mu-}h^2 + \frac{m_W^2}{2v^2\cos\theta_W}Z_\mu Z^\mu h^2\end{aligned} \tag{2.26}$$

We must not forget the Higgs potential, which after the unitary $SU(2)$ transformation, ends up with the following form:

$$V(H) = -\mu^2 H^\dagger H + \lambda (H^\dagger H)^2 = \frac{-\mu^2}{2}(v^2 + 2vh + h^2) + \frac{\lambda}{4}(v^2 + 2vh + h^2)^2$$

Replacing $\lambda = \frac{\mu^2}{v^2}$ and expanding, we get:

$$V(H) = \frac{-\mu^2 v^2}{2} - \cancel{\mu^2 vh} - \cancel{\frac{-\mu^2 h^2}{2}} + \frac{\mu^2 v^2}{4} + \mu^2 h^2 + \frac{\mu^2 h^4}{4v^2} + \cancel{\mu^2 vh} + \cancel{\frac{\mu^2 h^2}{2}} + \frac{\mu^2 h^3}{v}$$

$$= \frac{-\mu^2 v^2}{4} + \mu^2 h^2 + \frac{\mu^2 h^3}{v} + \frac{\mu^2 h^4}{4v^2}$$

Here, the first term is constant, and can be ignored since it does not affect the Lagrangian. The second term is the mass term of the Higgs, which means the Higgs mass is $m_h = \sqrt{2}\mu$. The third and fourth term are the Higgs self-interaction terms.

To recap, we started with:

- 4 massless vector fields (non-longitudinal, non-physical): W^1, W^2, W^3, B_μ
- 4 real scalar fields: the 3 α_i fields (goldstone bosons) and the h field

And after SSB, the goldstone bosons have been absorbed into the W fields, which after diagonalization leave us with:

- 3 massive vector fields (longitudinal, physical): W^+, W^-, Z^0
- 1 massless vector field: γ
- 1 massive scalar field: h

But not only that, because the first term of the lagrangian gives us the Higgs kinetic term, the mass terms of the W^+, W^- and Z^0 bosons, and the W^+, W^-, and

Z^0 couplings to the Higgs field, while the second term, the Higgs potential, gives us the Higgs mass term as well as its self-couplings.

$$\begin{aligned}\mathcal{L}_{Higgs} = &\frac{1}{2}(\partial_\mu h)(\partial^\mu h) + \frac{1}{2}m_W^2 W_\mu^+ W^{\mu-} + \frac{1}{2}m_Z^2 Z_\mu Z^\mu + \frac{m_W^2}{v} W_\mu^+ W^{\mu-} h \\ &+ \frac{m_Z^2}{v} Z_\mu Z^\mu h + \frac{m_W^2}{2v^2} W_\mu^+ W^{\mu-} h^2 + \frac{m_W^2}{2v^2 \cos\theta_W} Z_\mu Z^\mu h^2 \\ &+ \frac{1}{2}m_h^2 h^2 + \frac{g m_h^2}{4 m_W} h^3 + \frac{g^2 m_h^2}{32 m_W^2} h^4\end{aligned} \tag{2.27}$$

Yukawa Lagrangian

The Yukawa couplings describe the interaction between the Higgs field and the Fermions. Before SSB, the Yukawa Lagrangian is:

$$\mathcal{L}_{Yukawa} = -\bar{L}_L Y_\ell \, H \, \ell_R - \bar{Q}_L Y_d \, H \, d_R - \bar{Q}_L Y_u \, \tilde{H} \, u_R + h.c. \tag{2.28}$$

Where again we have the L_L left-handed lepton doublet $\binom{\nu}{\ell}_L$, the Q_L left-handed quark doublet $\binom{u}{d}_L$, and the right handed lepton and quark singlets ℓ_R, u_R, d_R. We also have the Higgs doublet H ($\tilde{H} = i\sigma_2 H^*$), and the 3×3 matrices of Yukawa couplings Y_ℓ, Y_u, and Y_d. After SSB, the Higgs field becomes $H = \frac{1}{\sqrt{2}}\binom{0}{v+h}$, which generates mass terms for the fermions, alongside their couplings to the Higgs boson:

$$\begin{aligned}\mathcal{L}_{Yukawa} = &-\frac{v}{\sqrt{2}}\,\bar{\ell}_L\, Y_\ell\, \ell_R - \frac{1}{\sqrt{2}}\,\bar{\ell}_L\, Y_\ell\, h\, \ell_R - \frac{v}{\sqrt{2}}\,\bar{d}_L\, Y_d\, d_R - \frac{1}{\sqrt{2}}\,\bar{d}_L\, Y_d\, h\, d_R \\ &- \frac{v}{\sqrt{2}}\,\bar{u}_L\, Y_u\, u_R - \frac{1}{\sqrt{2}}\,\bar{u}_L\, Y_u\, h\, u_R + h.c.\end{aligned} \tag{2.29}$$

The mass terms can be diagonalized by choosing the appropriate unitary transformations:

$$\begin{aligned} &\bar{\ell}_L = \bar{\ell}'_L\, U^\dagger_{\ell L} && \bar{u}_L = \bar{u}'_L\, U^\dagger_{uL} && \bar{d}_L = \bar{d}'_L\, U^\dagger_{dL} \\ &\ell_R = U_{\ell R}\, \ell'_R && u_R = U_{uR}\, u'_R && d_R = U_{dR}\, d'_R \end{aligned} \tag{2.30}$$

such that:

$$\begin{aligned}
\frac{v}{\sqrt{2}}\, U_{\ell L}^{\dagger}\, Y_{\ell}\, U_{\ell R} &= M_{\ell} = diag(m_e, m_\mu, m_\tau) \\
\frac{v}{\sqrt{2}}\, U_{uL}^{\dagger}\, Y_{u}\, U_{uR} &= M_{u} = diag(m_u, m_c, m_t) \\
\frac{v}{\sqrt{2}}\, U_{dL}^{\dagger}\, Y_{d}\, U_{dR} &= M_{d} = diag(m_d, m_s, m_b)
\end{aligned} \tag{2.31}$$

This unitary transformation, however, also has an effect on some of the terms in the fermion Lagrangian. While the couplings to the Z boson and the photon remain diagonal, the couplings to the W boson mix the upper and lower components of the lepton and quarks doublets. In the case of the lepton doublet, since the SM doesn't include a mass term for the neutrinos, we're free to transform them to leave the coupling to the W diagonal:

$$\mathcal{L}_{W\ell\, coup.} = \frac{ig}{\sqrt{2}} \bar{L}_L \gamma^\mu (W_\mu^+ \sigma^+ + W_\mu^- \sigma^-) L_L = \frac{ig}{2} (\bar{\nu}_L \gamma^\mu W_\mu^+ \ell_L + \bar{\ell}_L \gamma^\mu W_\mu^- \nu_L) \tag{2.32}$$

$$\Rightarrow \frac{ig}{2} (\bar{\nu}'_L\, U_{\ell L}^{\dagger}\, \gamma^\mu\, W_\mu^+\, U_{\ell L}\, \ell'_L + \bar{\ell}'_L\, U_{\ell L}^{\dagger}\, \gamma^\mu\, W_\mu^-\, U_{\ell L}\, \nu'_L) \tag{2.33}$$

$$= \frac{ig}{2} (\bar{\nu}'_L\, V\, \gamma^\mu\, W_\mu^+\, \ell'_L + \bar{\ell}'_L\, V\, \gamma^\mu\, W_\mu^-\, \nu_L) \tag{2.34}$$

where we chose $\nu_L = U_{\ell L}\, \nu'_L$, so that $V = U_{\ell L}^{\dagger}\, U_{\ell L} = 1$. On the contrary, for the quarks, the couplings to the W boson cannot be diagonalized at the same time as the masses, which mixes the quark generations:

$$\mathcal{L}_{Wq\, coup.} = \frac{ig}{\sqrt{2}} \bar{Q}_L \gamma^\mu (W_\mu^+ \sigma^+ + W_\mu^- \sigma^-) Q_L = \frac{ig}{2} (\bar{u}_L \gamma^\mu W_\mu^+ d_L + \bar{d}_L \gamma^\mu W_\mu^- u_L) \tag{2.35}$$

$$\Rightarrow \frac{ig}{2} (\bar{u}'_L\, U_{uL}^{\dagger}\, \gamma^\mu\, W_\mu^+\, U_{dL}\, d'_L + \bar{d}'_L\, U_{dL}^{\dagger}\, \gamma^\mu\, W_\mu^-\, U_{uL}\, u'_L) \tag{2.36}$$

$$= \frac{ig}{2} (\bar{u}'_L\, V\, \gamma^\mu\, W_\mu^+\, d'_L + \bar{d}'_L\, V^{\dagger}\, \gamma^\mu\, W_\mu^-\, u'_L) \tag{2.37}$$

where

$$V = U_{uL}^{\dagger}\, U_{dL} \tag{2.38}$$

is the Cabibbo-Kobayashi-Maskawa (CKM) matrix, which describes the mixing of the different quark generations in their couplings to the W boson.

Full Lagrangian

Finally, we can write the full SM lagrangian, by combining equations 2.6, 2.12, 2.15, 2.27 and 2.29:

$$\mathcal{L}_{SM} = \mathcal{L}_{Gauge} + \mathcal{L}_{Quark} + \mathcal{L}_{Lepton} + \mathcal{L}_{Higgs} + \mathcal{L}_{Yukawa} \tag{2.39}$$

Here we're still missing some terms that are needed to make the Lagrangian mathematically consistent, in particular we need a gauge fixing term, and a term for the Fadeev-Popov ghosts [5]. However, these are beyond the scope of this thesis, and so will not be included.

2.2 Beyond the Standard Model

Despite the success of the SM, it is not considered a complete model: it fails to incorporate the fourth fundamental force, gravity, and it also fails to explain a few phenomena, like the baryon asymmetry or the nature of neutrino mass. Nevertheless, the SM has been tested to great precision, and given its success with various physics predictions, it still stands as the main theory of particle physics, with most new theories attempting to expand the SM instead of replacing it. These theories are collectively called "Beyond the Standard Model", or BSM for short. One of these theories treats the SM as an effective field theory which is applicable up to energies not exceeding a certain scale Λ. In particular, we will look at the case of the so-called Standard Model Effective Field Theory (SMEFT).

2.3 The Standard Model Effective Field Theory

In order to understand effective field theories better, we must first learn about dimensional analysis. In the SM, the Lagrangian must have units of mass/energy to the fourth power. This is because the Lagrangian is what is used to find the Action, given by:

$$S = \int \mathcal{L}\, d^4x \tag{2.40}$$

The integration in 4 dimensions has units $[d^4x] = [\text{mass}]^{-4}$, and since Action must be dimensionless, then $[\mathcal{L}] = [\text{mass}]^4$. From this, the dimensions of the couplings and the fields in the terms of the Lagrangian are assigned, and it is found that fermions have a mass dimension of $[\phi] = [\text{mass}]^{\frac{3}{2}}$, while bosons have a mass dimension of $[B] = [\text{mass}]^1$.

In 1933 Enrico Fermi proposed a theory to explain the beta decay. In his theory, the neutron, proton, electron and neutrino share a direct coupling, which can be seen in the form of a Feynman diagram in Figure 2.2.

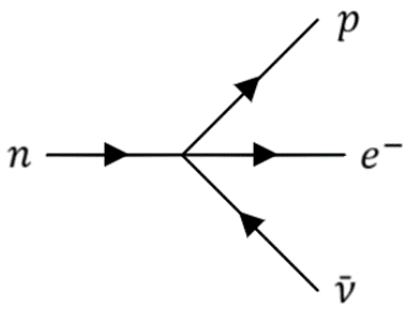

Figure 2.2: Fermi's proposed coupling to explain the neutron beta decay.

If we were to do a dimensional analysis of this type of coupling, we would find that it is forbidden: all particles involved are fermions, meaning that the dimension of the coupling is $\frac{3}{2} \cdot 4 = 6$. In reality, this interaction is mediated by a W boson, but the energy of the experiments at the time made it impossible to observe this. Only later, as the technology improved, were physicists able to observe the high energy behavior.

Figure 2.3 shows the real underlying process, which has not one, but two couplings. We can see that each coupling: the up-down-W coupling, and the W-electron-neutrino coupling, obeys the dimension restriction, adding up to 4 (bosons have a mass dimension of 1). Fermi's theory of beta decay is what is called an effective field theory: a low energy approximation of a high energy phenomenon which can't be observed due to the limitations in the energy of the experiments.

The Standard Model Effective Field Theory follows the same principle: it takes the same gauge symmetry as the SM $\left((SU(3)_C \times SU(2)_L \times U(1)_Y)\right)$ as a baseline, but expands it, and is constructed using the same fields. However, it adds

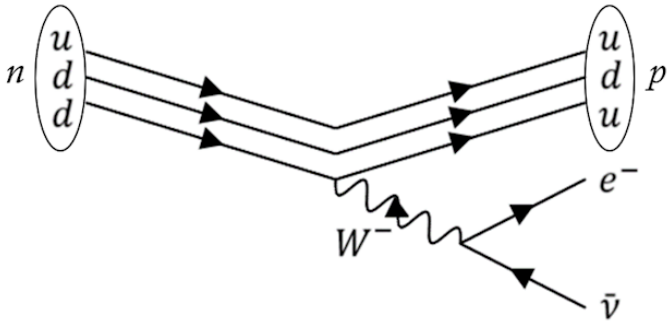

Figure 2.3: Beta decay showing the emission of a W boson, which then decays into an electron and an anti-neutrino. This can only be observed at high energies.

interactions that would normally be forbidden due to dimensional restrictions, and it is assumed that SMEFT is actually a low energy approximation of a higher energy theory, similar to the case of Fermi's beta decay theory. SMEFT has a Lagrangian of the form:

$$\mathcal{L}_{SMEFT} = \mathcal{L}_{SM}^{(4)} + \frac{1}{\Lambda}\sum_k C_k^{(5)} Q_k^{(5)} + \frac{1}{\Lambda^2}\sum_k C_k^{(6)} Q_k^{(6)} + O\left(\frac{1}{\Lambda^3}\right)$$

Where $\mathcal{L}_{SM}^{(4)}$ is the usual SM Lagrangian, $Q_k^{(n)}$ are n-dimensional operators, with $C_k^{(n)}$ being the corresponding dimensionless coupling constants (Wilson coefficients). To de-clutter the notation ahead, we will absorb the theory cut-off scale Λ in the definitions of the Wilson coefficients, rescaling them appropriately as $C_k^{(5)}/\Lambda \to C_k^{(5)}$, $C_k^{(6)}/\Lambda^2 \to C_k^{(6)}$.

2.3.1 Operators and Wilson parameters

For this analysis we'll use the so-called "Warsaw" basis of SMEFT [6], which is made of all the gauge invariant, independent dimension-6 operators. This basis has multiple "schemes" depending on the assumptions made on flavor symmetry. In the most general case, the theory is described by over 2000 parameters, however here we will use the so-called "top" flavor scheme. It assumes the following:

- The quarks of the first two generations and quarks of the 3rd generation are described by independent fields. They are denoted by (q_p, u_p, d_p)

with $p = 1, 2$ and by (Q, t, b) respectively, where q_p and Q are left-handed doublets, and u_p, d_p, t and b are right-handed singlets.

- A symmetry $U(2)_3 = U(2)_q \times U(2)_u \times U(2)_d$ is imposed on the Lagrangian, under which only the light quarks transform:

$$q \to \Omega_q q, \quad u \to \Omega_u u, \quad d \to \Omega_d d, \quad Q \to Q, \quad t \to t, \quad b \to b.$$

- Mixing effects in the quark sector are neglected and $V_{CKM} \equiv 1$.
- The lepton sector has a $U(1)^3_{\ell+e} = U(1)_e \times U(1)_\mu \times U(1)_\tau$ symmetry under which the fields transform as:

$$\begin{aligned} \ell_1 &\to e^{i\alpha_e}\ell_1, & \ell_2 &\to e^{i\alpha_\mu}\ell_2, & \ell_3 &\to e^{i\alpha_\tau}\ell_3, \\ e_1 &\to e^{i\alpha_e}e_1, & e_2 &\to e^{i\alpha_\mu}e_2, & e_3 &\to e^{i\alpha_\tau}e_3. \end{aligned}$$

These flavor assumptions reduce the number of free parameters to a more manageable 260. However, in this work we only focus on some of them that affect the electroweak sector, in particular the ones that affect the $WZ \to \ell\ell\ell\nu$ process.

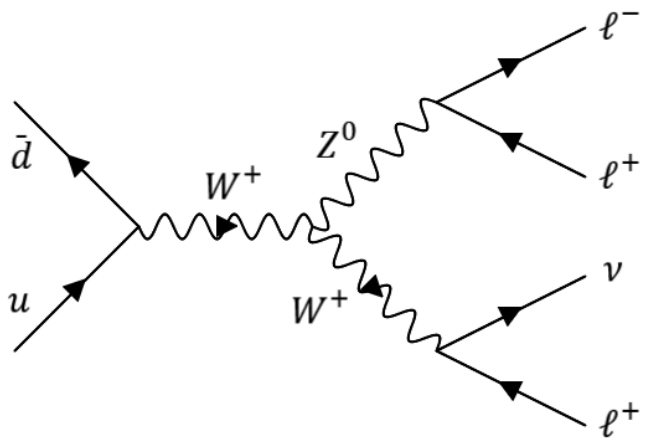

Figure 2.4: Feynman diagram of the s-channel $WZ \to \ell\nu\ell\ell$ process.

Looking at the Feynman diagram of the s-channel process in Figure 2.4 we can see that 4 couplings are involved:

- The coupling of two quarks to a W boson.

- The triple gauge coupling WWZ.
- The coupling of a Z boson to two same-flavored leptons.
- The coupling of a W boson to a lepton and a neutrino.

The t and u channels for this process are missing the triple gauge coupling, but add another coupling: the coupling of a Z boson to two same-flavored quarks. The Feynman rules of SMEFT [7] for these 5 couplings have the following dependencies:

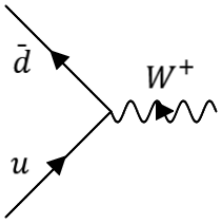

$$= f(C_{dW}, C_{Hq3}, C_{Hud}, C_{uW})$$

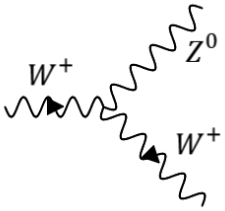

$$= f(C_W, C_{HWB}, C_{\tilde{W}}, C_{H\tilde{W}B})$$

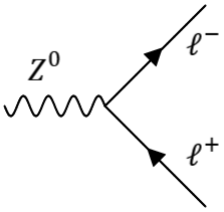

$$= f(C_{HWB}, C_{eW}, C_{eB}, C_{Hl1}, C_{Hl3}, C_{He})$$

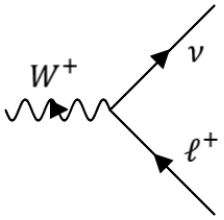

$$= f(C_{eW}, C_{Hl3})$$

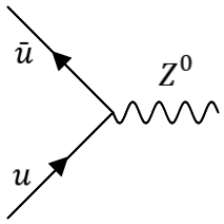

$$= f(C_{HWB}, C_{uW}, C_{uB}, C_{Hq1}, C_{Hq3}, C_{Hu})$$

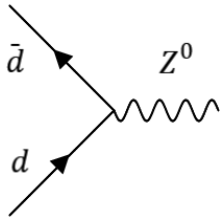

$$= f(C_{HWB}, C_{dW}, C_{dB}, C_{Hq1}, C_{Hq3}, C_{Hd})$$

In addition to these direct dependencies, there are two more parameters that affect the process: the Z boson mass (and in turn its propagator) depend on the C_{HD} parameter, while the parameter $C_{\ell\ell}$ introduces a SM-forbidden, 6-dimension 4 lepton vertex, which affects lepton self-energy and Z boson vertex corrections. Of these 20 parameters, preliminary studies showed that only 12 show sensitivity in the $WZ \to \ell\ell\ell\nu$ process. The parameters and their corresponding operators are:

$$\begin{aligned}
Q_{HD} &= (D^\mu H^\dagger H)(H^\dagger D^\mu H) & Q_{\ell\ell(prst)} &= (\bar{\ell}_p \gamma_\mu \ell_r)(\bar{\ell}_s \gamma^\mu \ell_t) \\
Q^{(1)}_{H\ell(pr)} &= (H^\dagger i \overleftrightarrow{D}_\mu H)(\bar{\ell}_p \gamma^\mu \ell_r) & Q_{HWB} &= H^\dagger \sigma^i H W^i_{\mu\nu} B^{\mu\nu} \\
Q^{(3)}_{H\ell(pr)} &= (H^\dagger i \overleftrightarrow{D^i_\mu} H)(\bar{\ell}_p \sigma^i \gamma^\mu \ell_r) & Q_{H\widetilde{W}B} &= H^\dagger \sigma^i H \widetilde{W}^i_{\mu\nu} B^{\mu\nu} \\
Q^{(1)}_{Hq} &= (H^\dagger i \overleftrightarrow{D}_\mu H)(\bar{q} \gamma^\mu q) & Q_W &= \varepsilon^{ijk} W^{i\nu}_\mu W^{j\rho}_\nu W^{k\mu}_\rho \\
Q^{(3)}_{Hq} &= (H^\dagger i \overleftrightarrow{D^i_\mu} H)(\bar{q} \sigma^i \gamma^\mu q) & Q_{\widetilde{W}} &= \varepsilon^{ijk} \widetilde{W}^{i\nu}_\mu W^{j\rho}_\nu W^{k\mu}_\rho
\end{aligned}$$

Where $H^\dagger i \overleftrightarrow{D}_\mu H = H^\dagger (iD_\mu H) - (iD_\mu H^\dagger) H$, $\widetilde{W}^{\mu\nu} = \frac{1}{2}\varepsilon^{\mu\nu\rho\sigma} W_{\rho\sigma}$, and the flavor indices *p, r, s, t* run over $\{1, 2, 3\}$ for leptons. In this work the tau interactions are not studied, so in the latter case only the indices $\{1, 2\}$ are considered. So, for $Q^{(1)}_{H\ell(pr)}$ and $Q^{(3)}_{H\ell(pr)}$ 4 cases are considered: $Q^{(1)}_{H\ell(11)}$, $Q^{(1)}_{H\ell(22)}$, $Q^{(3)}_{H\ell(11)}$ and $Q^{(3)}_{H\ell(22)}$, while for $Q_{\ell\ell(prst)}$ only $Q_{\ell\ell(1221)}$ is considered. It should be noted that some of these operators also affect the background processes of this study.

3 The ATLAS Experiment at the LHC

This work relies on data from the collisions of particles at high energies. Although these events can happen naturally when cosmic rays hit earth's atmosphere, we have no control over their energy or the rate at which they occur. As such, we need a more controlled environment in which we can manipulate those variables to our liking. This can be accomplished using large particle accelerators, which use strong electromagnetic fields to accelerate charged particles up to speeds close to the speed of light, and collide them against one another. The largest such machine ever built is the Large Hadron Collider (LHC), at CERN. Section 3.1 will give a brief overview of CERN and its history, section 3.2 will introduce the Large Hadron Collider and the stages used to accelerate the particles to their target energies, and finally section 3.3 will describe the ATLAS detector and its subsystems.

3.1 CERN

In 1954, 12 european countries founded a physics organization dedicated to research the nuclei of atoms. It was named "CERN" after its french acronym: *Conseil Européen pour la Recherche Nucléaire* (European Council for Nuclear Research), and while it has kept the name, over the years it shifted its main area of research to particle physics. The name CERN is nowadays used to refer to both the organization, and the laboratory, which is located in Meyrin, Geneva, on the French-Swiss border. In the 70 years since its foundation, CERN has expanded to include 25 member states, 9 associate states, and over 40 non-member states with cooperation agreements. Physicists at CERN have made several achievements throughout its history, just to name a few: the discovery of the W and Z bosons

in 1983, the discovery of direct CP violation in 1999, and more recently, the discovery of the Higgs boson in 2012. CERN has also played an important role in computer science, being the birthplace of the world wide web, in 1989. Currently, CERN operates various accelerators used for high energy physics research, the largest and most energetic of these being the Large Hadron Collider.

3.2 The Large Hadron Collider

The LHC is contained in a circular tunnel with a circumference of 26.7 km, at a depth over 50 metres underground, and it houses various experiments, as seen in Figure 3.1. It consists of two concentric beamlines, each containing a beam of particles that travel in opposite directions. The beams cross at 4 different points of the ring, where the particle collisions occur. Radiofrequency (RF) cavities use electric fields to accelerate the particle beams, while powerful magnets are used to steer and focus them. The LHC is the most powerful particle collider in the world at the time of writing, and can achieve energies of 13.6 TeV.

The protons used for the collisions at the LHC cannot be simply accelerated to their final energy, they must be accelerated in various stages. For this, negative Hydrogen ions (H^-) are injected into LINAC4, a smaller linear accelerator which feeds them into the Proton Synchrotron Booster (PSB), where they are stripped of their electrons leaving the bare protons. The protons are further accelerated to 2 GeV before being injected into the Proton Synchrotron (PS). Here, they are accelerated up to 26 GeV, and they are injected into the Super Proton Synchrotron (SPS), which accelerates them further up to 450 GeV. Finally, the protons are injected into the two opposite-going beamlines of the main LHC ring, where they are accumulated into bunches, and accelerated up to their final center-of-mass energies.

The proton bunches cross at 4 interaction points where the ATLAS, CMS, ALICE and LHCb detectors are located, at a rate of one bunch-crossing every 25 nanoseconds, or 40 million each second. The data obtained from the ATLAS detector has been used in this work.

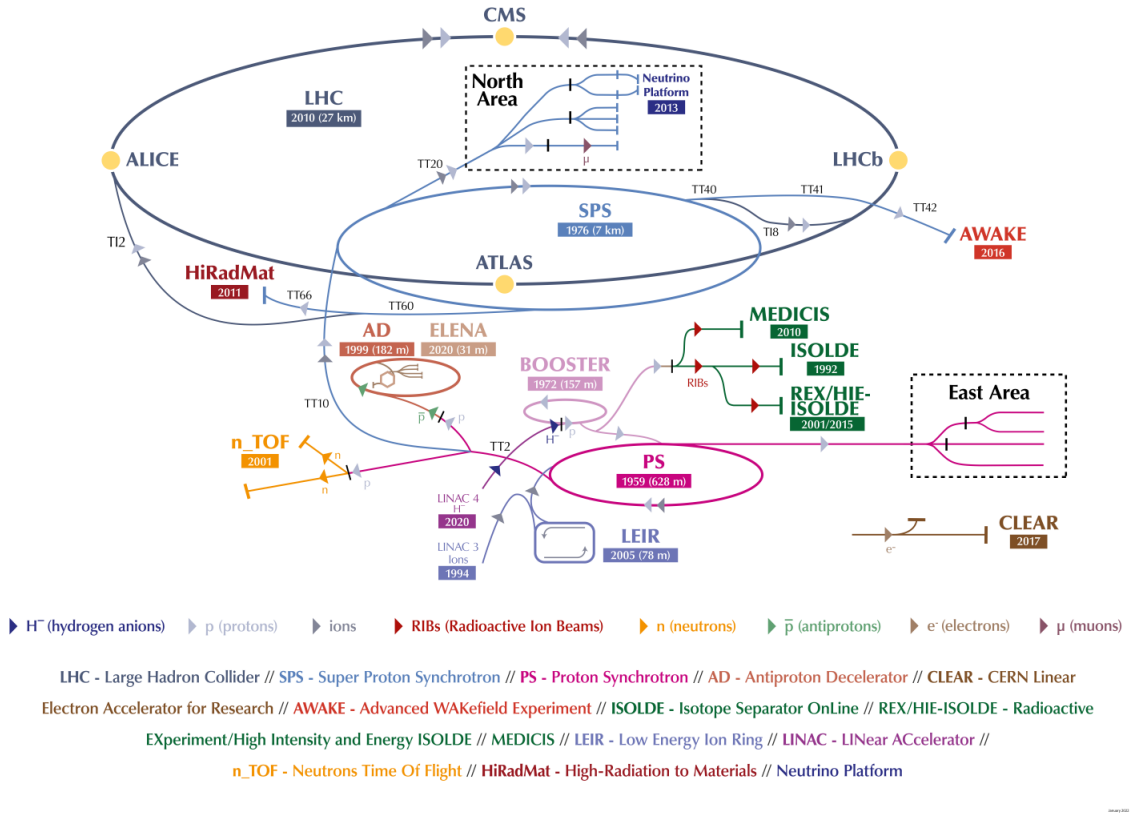

Figure 3.1: Graphic overview of the Large Hadron Collider, detailing the various experiments that form part of it. [8]

3.3 The ATLAS Experiment

The ATLAS Experiment is the largest general-purpose particle detector in the world. It is designed to measure as many particles as possible from the collisions at the interaction point. It is shaped like a barrel on its side, being 46 metres long, 25 metres in diameter, and weighs about 7000 tonnes. In order to be able to detect the paths taken by the particles, ATLAS uses a layered design. As the particles move from the interaction point outwards they cross multiple layers, and the points of each layer where a particle was detected are connected to reconstruct the path or "track" the particle took. Since different particles have different ways of interacting with matter, various subsystems are used to detect and distinguish different particle types.

Figure 3.2 shows this. All charged particles (like electrons, muons and protons)

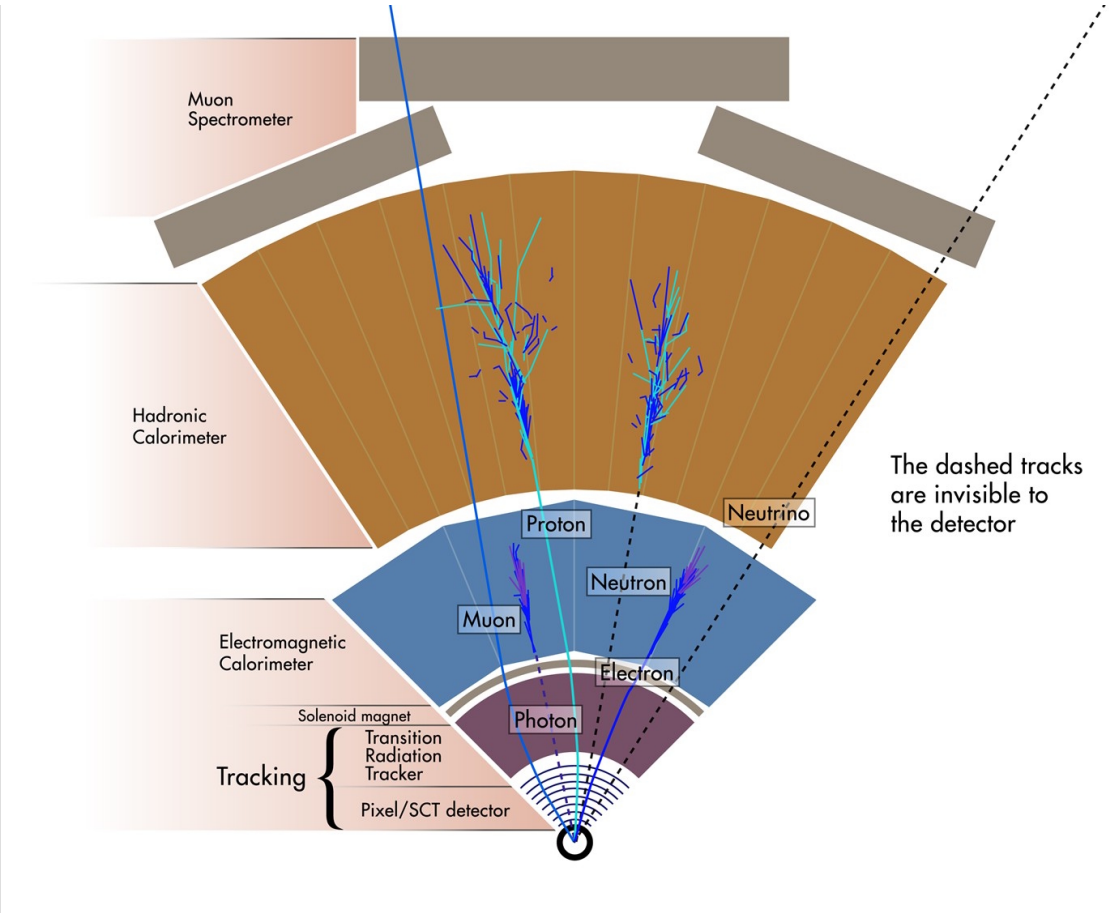

Figure 3.2: Diagram detailing how different particles interact with the different ATLAS systems. [9]

leave tracks in the inner detector. Particles that interact electromagnetically have their energy absorbed by the Calorimeters. Lighter ones like electrons and photons deposit their energy in the Electromagnetic Calorimeter, while heavier ones like protons and neutrons do so in the Hadronic Calorimeter. Muons and neutrinos pass through all detectors without being stopped, but muons leave tracks since they are charged, whereas neutrinos aren't detected at all.

3.3.1 Inner Detector

The Inner Detector is the component that is the closest to the interaction point of the collisions. It consists of the subsystems: the Pixel Detector, the Semiconductor Tracker (SCT), and the Transition Radiation Tracker (TRT), as seen in figure 3.3.

Its main function is to detect the traces left by charged particles as they move through the layers of the various subsystems (see figure 3.4).

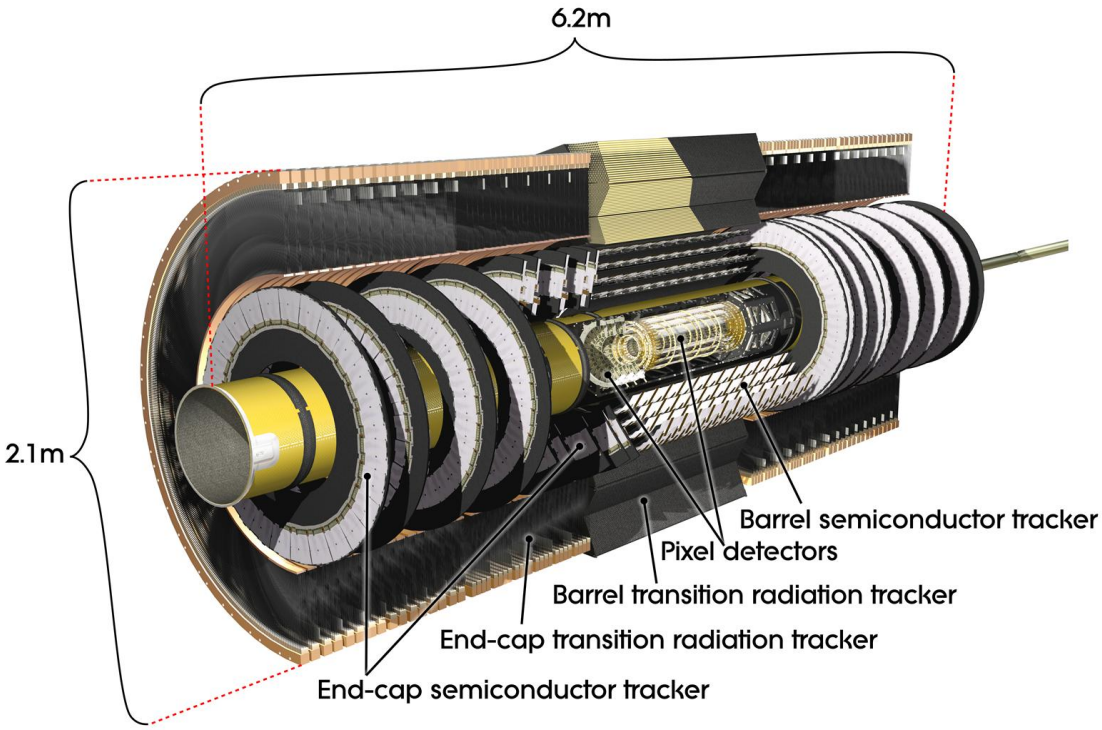

Figure 3.3: Diagram showing the subsystems of the Inner Detector. All subsystems have a barrel component, and an endcap component, conforming to ATLAS's barrel shape. [10]

Pixel Detector

The closest subsystem to the interaction point. It can be thought of as a cylindrical camera, but instead of capturing a flat photo, all the pixels point to its center, and it takes one "picture" every 25 nanoseconds. The barrel section has 4 concentric layers, whereas the endcap has 3 disks per side. It has about 2000 modules, with each module having about 46,000 pixels. In total, about 92 million pixels, or 92 MP. The pixels are 50×250 μm in the innermost layer (IBL), and 50×400 μm in the external layers, both smaller than the size of a grain of sand. All the pixels together add up to an effective detection area of 1.9 m^2.

Semiconductor Tracker (SCT)

The SCT is the next subsystem going outwards radially. It has a similar concept to the Pixel Detector, only instead of pixels it uses long strips to cover a larger area more practically. The barrel section has 4 concentric layers, and the endcap has 9 disks per side. The SCT has 4088 two-sided modules in total, with each module having 768 strips, for a total of about 6.3 million channels. Each strip has a width of 80 μm, or about the width of a human hair, and a length of 12 cm. All together, they make up an area of about 60 m^2. The strips' dimensions give the SCT the most critical tracking capabilities in the plane perpendicular to the beam axis.

Transition Radiation Tracker (TRT)

The final subsystem of the Inner Detector, the Transition Radiation Tracker, is the outermost component, and unlike the Pixel Detector and the SCT, which use silicon detectors, the TRT uses a technology called "drift tubes". These tubes, also called "straws", are 4 mm in diameter and up to 144 cm long, and have a gold-plated tungsten wire in their center, only 30 μm in diameter. The straws are filled with a non-flammable gas mixture of 70% Xe, 20% CO_2, and 10% CF_4, and the wire is held at 1500 V. When a charged particle crosses the gas, it ionizes it, and the electrons drift towards the wire and create a pulse signal. The various refraction indices of the materials in the TRT cause ultra-relativistic particles to produce transition radiation, which can be used to differentiate the lighter particles, like electrons and positrons, from heavier ones like pions. This is because the transition radiation energies depend on the speed of the particle, and since particles at a certain momentum will move faster the lighter they are, electrons and positrons will appear as having stronger transition radiation energies.

3.3.2 Calorimeters

Surrounding the Inner Detector are the Calorimeters. They consist of layers of high density material that absorbs the energy of the particles, interlaced with sampling layers, which measure the absorbed energy. It is subdivided into two subsystems based on the type of particle they can detect: the Electromagnetic (EM) Calorimeter, and the Hadronic Calorimeter. The EM Calorimeter is the one

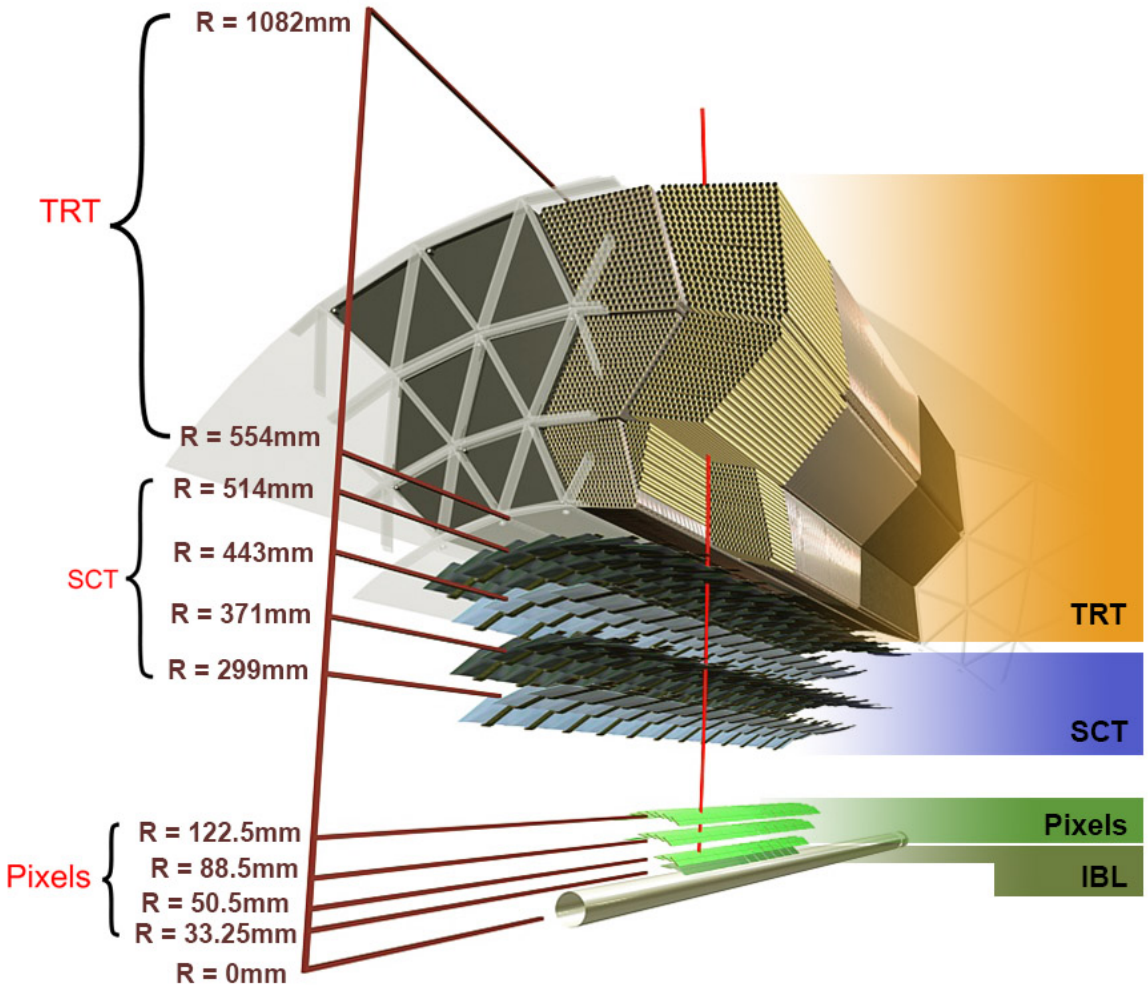

Figure 3.4: Diagram showing how a track would cross the various layers of the subsystems of the Inner Detector. The distances to the beam axis are also shown. [11]

closer to the interaction point, and it measures the energy of light particles that interact electromagnetically. The heavier particles that aren't stopped by the EM Calorimeter reach the Hadronic Calorimeter, where they are finally stopped (with a few exceptions). These calorimeters use two types of technology: Liquid Argon Calorimeters, and Tile Calorimeters.

Liquid Argon Calorimeter

The Liquid Argon (LAr) Calorimeter, as the name suggests, uses liquid argon to measure the energy of the particles that are absorbed by it. Metal layers absorb

the particles, creating showers of less energetic particles, which ionize the LAr between the layers and create the electric current that is measured. In order to keep the argon in a liquid state, the systems are cooled to −184°C. There are 4 different subsystems: the Electromagnetic Barrel Calorimeter (EMB, lead layers), the Electromagnetic Endcap Calorimeters (EMEC, lead layers), the Hadronic Endcap Calorimeters (HEC, copper layers), and the Forward Calorimeters (FCal, copper/tungsten layers).

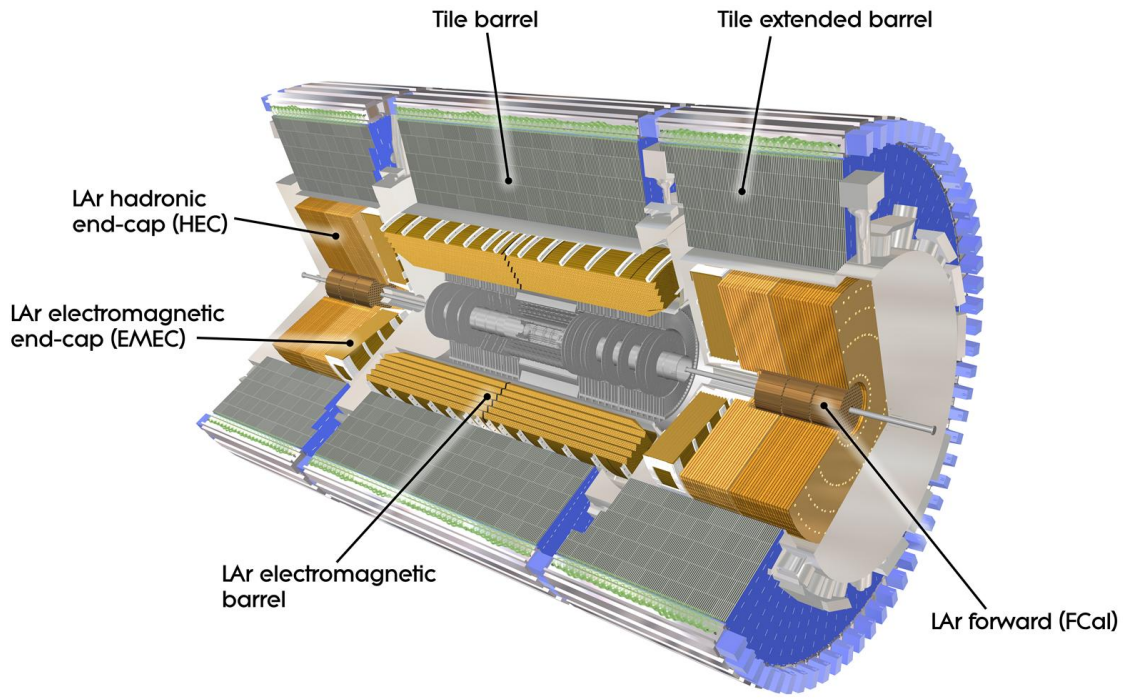

Figure 3.5: Diagram showing the ATLAS Calorimeter and its subsystems. [12]

Tile Calorimeters

The barrel section of the Hadronic Calorimeter uses a similar technology, but instead of liquid argon, the sampling materials are scintillating tiles, hence the name, Tile Calorimeter. It has a fixed central barrel, and one movable extended barrel to each side. It is made of alternating steel and scintillating tiles, where the steel absorbes the particles, and the scintillating tiles sample the energy deposited in the calorimeter.

3.3.3 Magnets

In order to measure the momenta of the charged particles produced in the events, ATLAS uses strong magnets to create a magnetic field, which makes the charges particles take curved trajectories. The curvature of the path is related to the strength of the magnetic field, as well as the charge, mass and velocity of the particle. There are 3 magnet subsystems that together create the magnetic field in ATLAS.

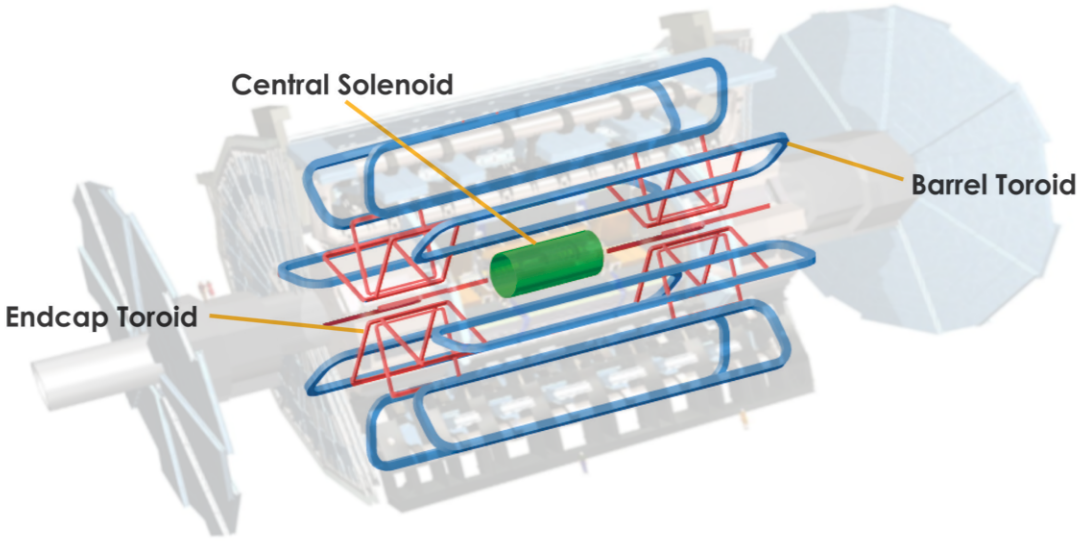

Figure 3.6: Diagram showing the magnets that make up the ATLAS magnet system.

Central Solenoid Magnet

This magnet surrounds the Inner Detector, creating inside of it a mostly uniform 2 Tesla magnetic field aligned with the beam line. It is a 5.8 m long cylinder, with a diameter of 2.56 m, a thickness of only 4.5 cm, and it consists of a single coil with over 1000 turns, using a total of 9 km of superconducting wire.

Barrel Toroid

The Barrel Toroid is used to create the magnetic field outside of the Inner Detector, in the barrel section. It consists of 8 superconducting coils arranged equidistant

from each other around the ID. The coils are housed inside individual cryostats to keep them at the right temperature. The 8 coils together, create a magnetic field that loops around the ID and the beam line. This magnetic field however, is not completely uniform, because the cost would be too expensive, and it would not leave enough room for the Muon Spectrometer. The coils are located just outside the calorimeters, but still within the volume of the Muon Spectrometer; they are 25.3 m long, use over 56 km of superconducting wire, and create a field of 2-6 Tesla in the $0.0 < |\eta| < 1.3$ pseudorapidity range[1].

Endcap Toroids

Similar to the Barrel Toroid, the 2 Endcap Toroids consist of 8 superconducting coils each, which create a magnetic field that loops around the beam line. These coils, however, are smaller and closer together, since they sit just outside the Inner Detector, in the endcap regions. The coils of each Endcap Toroid use about 13 km of superconducting wire, and are housed within the same cryostat, which gives them a distinctive "gear" appearance. These "gears" have a width of 5 m, a diameter of 10.7 m, and create a magnetic field of 4-8 Tesla in the $1.6 < |\eta| < 2.7$ range.

3.3.4 Muon Spectrometer

While most particles are stopped by the calorimeters, most muons can travel through them and escape detection completely. Thus dedicated detectors are placed in the outermost parts of ATLAS to be able to detect and characterize these muons. Various fast-response detectors are used as triggers, which include the Resistive Plate Chambers and the Thin Gap Chambers. Precision detectors are used for position and tracking measurements, which include the Monitored Drift Tubes and the Cathode Strip Chambers[2].

[1] Pseudorapidity is a spatial coordinate that represents the angle of a particle relative to the beam axis, and is defined as: $\eta \equiv -\ln\left[\tan\left(\frac{\theta}{2}\right)\right]$.

[2] The CSC, MDT and TGCs in the “Small Wheel" have since been replaced by the Micromegas and sTGCs to prepare for the High Luminosity LHC, forming the “New Small Wheel". Since the data used in this work was taken with the old detectors, the components of the NSW will not be described here, instead they are described in Appendix C.

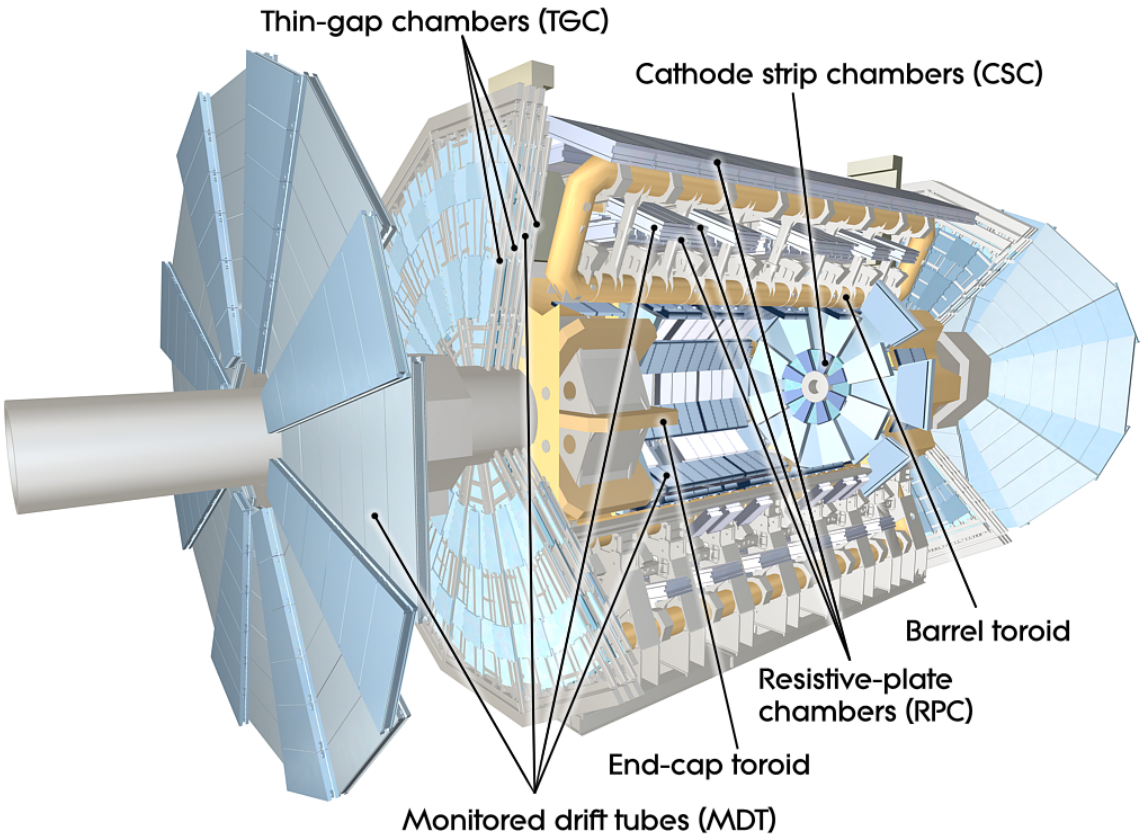

Figure 3.7: Layout of the subsystems of the muon spectrometer. [13]

Resistive Plate Chambers

The Resistive Plate Chambers (RPCs) are responsible for the fast-response detection of muons in the barrel area. They are gaseous parallel electrode-plate detectors, without wires. Each RPC has two resistive plates separated 2mm by a gas volume filled with a $C_2H_2F_4/C_4H_{10}/SF_6$ mixture. When functioning, a 4.9 kV/mm electric field is induced between the plates, so that when the incoming muons ionize the gas, the resulting ions drift to each of the plates. Here, they are detected by two sets of strips, which run perpendicular to each other, in ϕ and η. Three concentric layers of RPC provide 3 points of measurement (6 different measurements) for each muon track that crosses the three layers. This redundancy allows for a strong trigger robustness, rejecting fake muons and ensuring good detection efficiency.

Thin Gap Chambers

The Thin Gap Chambers (TGCs) on the other hand, are responsible for the fast-response detection of muons in the endcap area. Four sets of TGCs are used on each endcap: three forming part of the so-called "Big Wheel" right outside the endcap toroid, and one located in the "Small Wheel", between the calorimeters and the endcap toroid. The TGCs are multiwire proportional chambers, and get their name from the fact that the distance between the cathodes and the wire plane (1.4 mm) is smaller than the distance between the wires (1.8 mm). The cathodes are divided into strips that are oriented so that they point approximately to the beamline, while the wires run perpendicular to the strips, which allows a measurement of two orthogonal coordinates. The TGCs use a gas mixture of 55% CO_2 and 45% n-pentane and when in operation, a ~3 kV voltage is applied between the wires and the cathodes, so when the incoming muons ionize the gas mixture, the ions quickly drift to the wires and cathodes. This combination of geometry and highly quenching gas mixture give the TGCs an excellent time resolution, allowing for bunch crossing identification for the trigger system.

Monitored Drift Tubes

Monitored Drift Tubes (MDTs) are used for precision tracking in almost all of the muon spectrometer. The basic element of the MDTs are long (1-6 m) aluminum tubes, with a width of 3 cm, and a metal wire running through its center. The tubes are filled with an Ar/CO_2 (93%/7%) gas mixture, which is held at a pressure of 3 bar. The tubes are assembled into rectangular chambers that hold hundreds of tubes, and these chambers are placed in the entirety of the barrel, and most of the endcap. While they are placed over the entirety of the "Big Wheel" and the "Outer Wheel", in the "Small Wheel" they don't cover the pseudorapidity range $|\eta| > 2$, since the high counting rate expected in this area would exceed the MDT's safety limit. The chambers are positioned such that the incoming muons would cross the tubes perpendicularly (approximately). The incoming muons cross multiple tubes quickly, ionizing the gas, and the electrons drift to the wires. Given the cylindrical geometry, this ionization will be larger or smaller depending on the distance of the track to the center of the tube, since if the muon hits close to the shell of the tube, it can only ionize a small region of gas, while if it crosses the center, it will ionize a larger region. The distance of this ionized gas to the wire will also create

different shapes of pulses, since a hit close to the shell of the tube would create a short weak pulse, while a muon that crosses the center would create a longer pulse, since the track covers various distances to the center of the tube. All of this means that the hit information alongside the drift times of the hits of multiple tubes can be used to obtain a very precise track. At the same time, one disadvantage of this is that the longer pulse (up to 700 ns) of the tracks that pass close to the wire could create pulses that last for multiple bunch crossings. Similarly, for tracks that pass close to the outer radius the electrons have to travel all the way to the wire, creating shorter pulses but with later start times. These problems are solved by using a dead-time in the front-end of the readout chain.

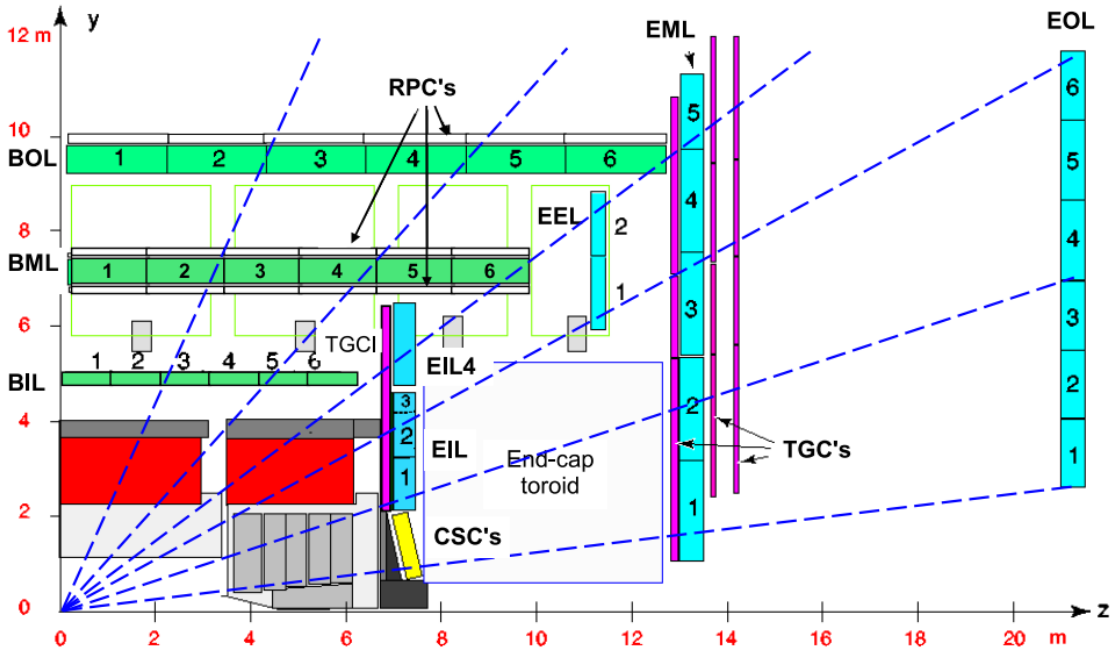

Figure 3.8: Diagram of the cross section of a quadrant of the Muon Spectrometer. The RPCs are represented with white boxes, while the TGCs are in pink. As for fast response detectors, in green are the barrel MDTs, in light blue the endcap MDTs, and in yellow the CSCs [14].

Cathode Strip Chambers

For the pseudorapidity region $|\eta| > 2$, which is expected to have the highest flux of particles, it is necessary to use a different technology, one which can operate properly in those conditions. ATLAS uses Cathode Strip Chambers (CSCs), which are multiwire proportional chambers that can operate at rates up to 1000 Hz/cm^2. The CSCs have segmented cathodes on both sides, one with strips oriented radially, parallel to the wires, and the other with strips oriented perpendicular to them. The chambers are filled with a gas mixture of Ar/CO_2 (80%20%), and they are operated with a voltage of 1900 V. Each chamber is made from four CSC planes, which results in four independent measurements for each track (the wire signals are not read out). The chambers come in two varieties, a small and large one, with each "wheel" having 8 of each. Unlike the other detectors in the endcap region, the CSCs are slightly tilted towards the interaction point, which improves the performance of the detector, since the avalanche is formed on a single point along the wire.

3.4 Phenomenology of $p\,p$ collisions

During a bunch-crossing in ATLAS, two protons moving in opposite directions might collide head on, producing a *hard* interaction. In this collision, the components of one proton interact with the components of the other one. These components are:

- **Valence quarks**: the quarks that give the proton its quantum numbers (two up quarks, and one down quark).
- **Gluons**: the particles being exchanged between the quarks, keeping the proton bound together.
- **Sea partons**: virtual quark-antiquark pairs that exist temporarily due to quantum fluctuations.

This composite nature of the proton means that although the total momentum of a proton in the LHC is known, the momentum of the individual partons is unknown. The only known fact, is that most of the momentum of the partons is in the longitudinal direction, since the total transverse momentum of the proton

is close to 0, thus making the transverse momentum of the partons negligible. This distribution of the momentum between the various partons is modeled using parton distribution functions (PDFs), that have the form $f_a(x, Q^2)$, where a is the parton type, x is the momentum fraction, and Q^2 is the energy scale at which this distribution occurs. An example of the PDFs of the partons of a proton can be seen in Figure 3.9. These PDFs can't be calculated analytically due to the non-perturbative nature of QCD, and must instead be determined experimentally. The PDFs obtained at a certain value of Q^2 can be used to obtain the PDF at a different value of Q^2.

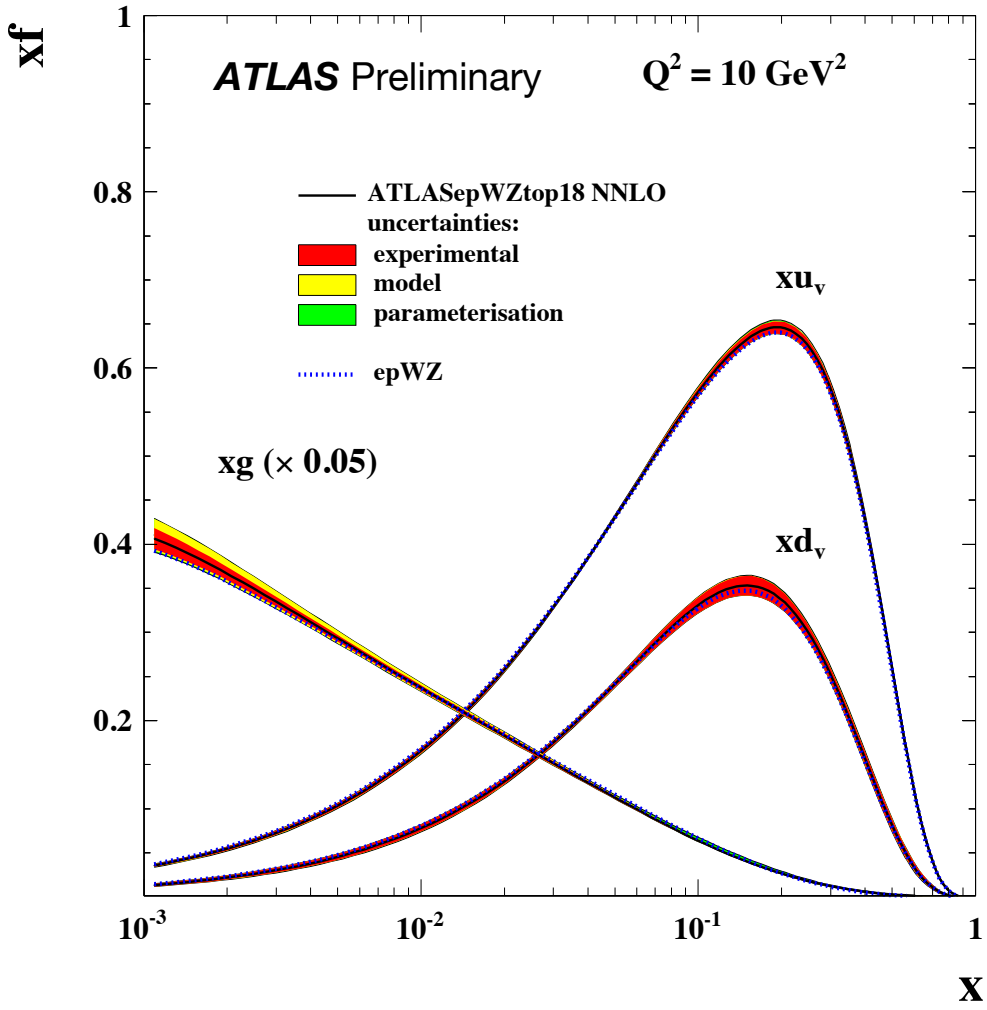

Figure 3.9: PDFs of up and down valence quarks, as well as gluons in a proton at an energy scale of 10 GeV [15]

In addition to a few hard interactions, each bunch crossing in ATLAS can have multiple *soft* interactions, where the momentum exchange is small. While these soft interactions can have interesting physics, most of the time the focus is on the hard interactions, making these extra soft ones a background. The mean number of interactions per bunch crossing is called *pileup*, it is written as $\langle\mu\rangle$, and in ATLAS, from 2015 to 2018, had a mean value of 33.7, as seen in Figure 3.10.

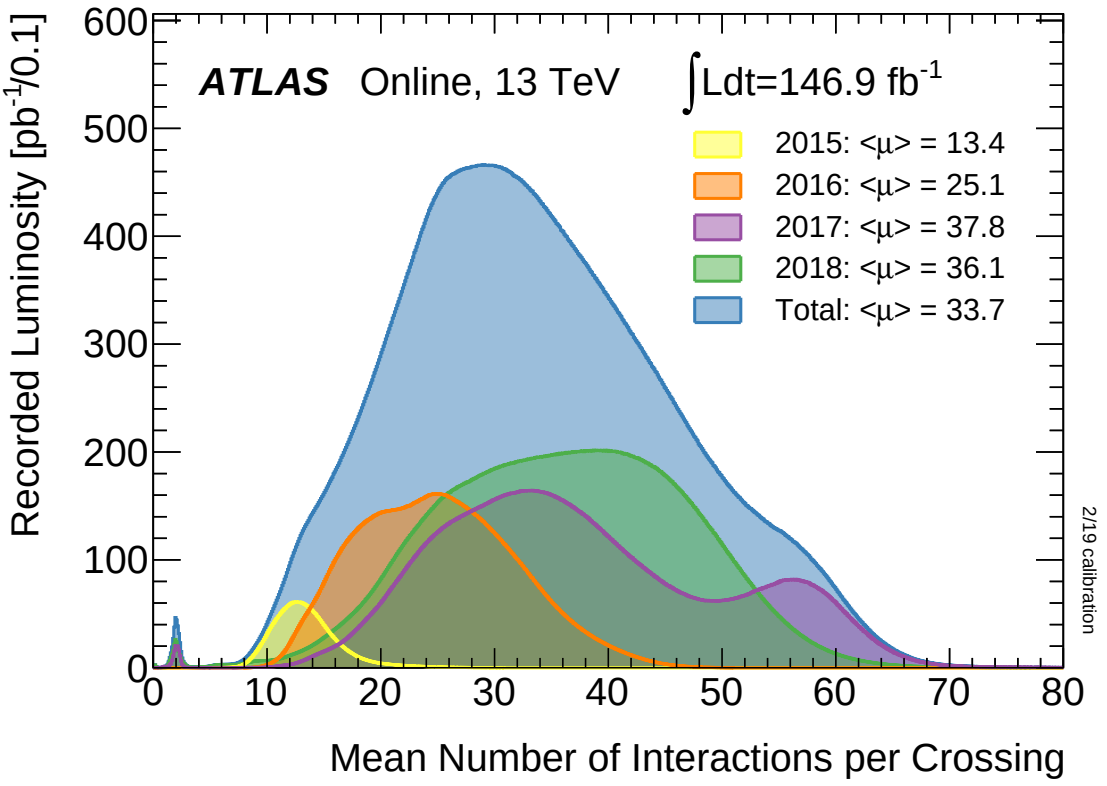

Figure 3.10: Pileup per year at ATLAS [16]

4 Data and Monte-Carlo samples

For this analysis, both "real" collision data (or just data) and simulated data are used. While in real data the sample events and background events are always together, for simulated samples one has control over what is generated. For example, signal samples and background samples can be generated separately, and models different from the SM can be used. This allows us to model our background, as well as compare the results of our measurements to both the SM and SMEFT using various values for the parameters of the model, both of which can in turn be used to set a limit on those parameters. In order to maximize the usefulness of our simulated SMEFT samples, a decomposition method is used for them. Section 4.1 describes the data, section 4.2 describes the simulated samples including SM samples, SMEFT samples, and background samples, while section 4.3 describes the decomposition method in more detail.

4.1 Data

This analysis uses data of pp collisions collected from 2015 to 2018 using the ATLAS detector, at a center-of-mass energy of $\sqrt{s} = 13$ TeV, and corresponds to an integrated luminosity of $139\,\text{fb}^{-1}$.

4.2 Monte Carlo samples

Multiple simulated samples, called *Monte Carlo (MC) samples* were used to model the signal and background processes involved. For our signal, one SM sample and various SMEFT samples were generated, whereas for the background, the following processes were simulated:

- Processes with two or more electroweak gauge bosons: ZZ, WW, VVV
- Processes with top quarks: $t\bar{t}$, $t\bar{t}V$, single top, tZj
- Processes with gauge bosons associated with jets or photons: $Z + j$, $Z\gamma$

The simulation of particle collision processes like the ones above is done in various steps, where often each step is performed using different software, which transforms the data from its most "theory-like" form to its more complex and "real-life" form. In order, they are:

- **Matrix element calculation**: the matrix element of the requested hard scatter process is calculated based on the chosen QCD and QED rules, which allows for simulating models different from the SM. Individual events are sampled from that result, producing a list of "hard" (high momentum) partons.
- **Parton shower/hadronization**: the partons from the hard scatter events go though a QCD simulation which emulates the processes that happen at lower energy scales, creating showers of particles all the way down to the formation of color-singlet bound states, a process called "hadronization". Due to the non-perturbative nature of low energy QCD, special functions called "parton distribution functions" (PDFs), which are obtained experimentally, must be used in the calculation. Data at this point is known as "truth" data, meaning all the particles that in theory get produced are still in the record, and no information has been smeared or lost. The data is also entirely model dependant, and not ATLAS-specific.
- **Detector simulation and digitization**: the paths of "stable" particles are simulated, alongside their interactions with the detector and the magnetic fields, sometimes producing new particles or decaying. Afterwards the simulated energy deposits are converted into digitized signals, equivalent to the raw data that is obtained with the ATLAS detector. At this step, some information is "corrupted" or "lost" on purpose, which is done because the detectors are not 100% efficient or accurate, but also because some particles will propagate to the blind spots of the detector. This is done to obtain a more accurate representation of what really happens in the detector.

- **Reconstruction**: the remaining digital signals are reconstructed into physics objects, like electrons and jets, in the same way that it is done for real ATLAS data.

With these steps in mind, there are two possible approaches to an analysis. The simplest and most common one is to compare the reconstructed simulated samples to the reconstructed data from the detector and work from there. Another possibility, is to model the effects of the detector on the data as accurately as possible, and then "revert" those effects on the reconstructed data, in order to obtain the "real" data, which can then be compared to the truth simulated data (before detector simulation). This second approach is called "unfolding", and it is what is used in this analysis [17].

4.2.1 SM sample

The SM predictions were simulated at NLO in QCD using the POWHEG BOX v2 [18–21] generator. The events were interfaced to PYTHIA 8.210 [22] for the simulation of the parton showering, hadronization, and underlying event, with the AZNLO [23] tune of parameters. The CT10NLO PDF set [24] was used for the hard-scattering processes, while the parton shower used the CTEQ6L1 PDF set [25].

In order to obtain the most accurate prediction possible, generation of higher order terms is necessary. For this sample, the effect of the NNLO QCD and NLO electroweak corrections is calculated using MATRIX 2.1 [26].

4.2.2 SMEFT samples

The samples that model the SMEFT effects were generated at LO with MADGRAPH 2.9.9 [27], using the SMEFTSIM [28, 29] model, which includes terms up to dimension 6, and for each sample only one parameter at a time was allowed to take non-zero values. Two samples were generated for each parameter, where the first one includes only the SM-SMEFT interference (linear in C_K), and the second one includes the purely SMEFT events (quadratic in C_K). For both samples the Wilson parameter was set to a value of 1, with the mass scale $\Lambda = 1$ TeV. The reasoning and validation of these samples is further explained in section

4.3. The generation was interfaced with Pythia 8.307 for the simulation of the parton showering and hadronization, using the NNPDF3.0nlo [30] PDF set. With the accuracy of the SM sample being NNLO, it becomes necessary to adjust the SMEFT sample to account for that difference. For this reason, a MC sample using the same configuration as the SMEFT samples (Madgraph with SMEFTsim model) is generated, only with all the parameters set to 0, which removes the SMEFT effects and creates just a SM LO sample. This sample is then compared bin-by-bin to the Powheg SM NNLO sample, and the scale factors obtained are applied to the SMEFT samples.

4.2.3 Background samples

Various generators were used to make the background samples. Sherpa 2.2.2 [31] was used to simulate ZZ events (both $q\bar{q}$ and gg initiated) using the NNPDF3.0nnlo PDF set, as well as the triboson (VVV, where $V = W, Z$) events, which used the NNPDF3.0nlo PDF set. The $t\bar{t}Z$ and $t\bar{t}W$ samples were generated with Madgraph interfaced with Pythia for the parton shower, and used the NNPDF3.0nlo PDF set. The $t\bar{t}$ was generated at NLO using Powheg interfaced with Pythia for the parton shower, using the NNPDF3.0 PDF set during the event generation, and NNPDF2.3 with the A14 tune [32] during the shower simulation. The tZj events were generated at LO using Madgraph interfaced with Pythia for the parton shower, with the NNPDF3.0nlo PDF set for the event generation and the NNPDF2.3lo PDF set for the parton shower simulation.

4.3 Decomposition method

By default, Monte-Carlo generators calculate the squared amplitude matrix of the process including all the terms of the calculation:

$$|\mathcal{A}_{SM} + \sum_i c_i \mathcal{A}_i|^2 = |\mathcal{A}_{SM}|^2 + 2\sum_i c_i \mathrm{Re}(\mathcal{A}_{SM}^* \mathcal{A}_i) + \sum_i c_i^2 |\mathcal{A}_i|^2 + 2\sum_{i,j,i\neq j} c_i c_j \mathrm{Re}(\mathcal{A}_i^* \mathcal{A}_j) \tag{4.1}$$

where the first term represents events that aren't affected by SMEFT, i.e. events that are purely SM. The second term represents the events that come from SM-SMEFT

interference, also sometimes referred to as the linear term, since it is linear in terms of c_i. The third term represents events that are purely from SMEFT effects, and is called the quadratic term, since it's quadratic in c_i. The last term represents the events that come from the interference between different SMEFT parameters, also called the cross term. For this analysis, we only study one parameter at a time, so this last term is always set to 0.

The downside of this type of generation is that if one wants to see how a distribution would look for a different value of c_i one would have to generate the events again, which depending on the size of our sample, could take hours or even days. This is due to the fact that SM events that aren't affected by SMEFT wouldn't scale at all, events that are the product of SM-SMEFT interference would scale linearly, and events that are purely SMEFT would scale quadratically. Since this information is not kept during the generation, we are unable to manipulate the sample to obtain this new estimate, and we are forced to generate a new sample at the value we want to test. One approach which is often used to solve this issue is to use a reweighting method, where at the time of generation, each event is assigned an event weight corresponding to each value of a preselected range of values of the parameter. These event weights can be later be used to interpolate/extrapolate to a new value to simulate how the distribution would look using a different value of the SMEFT parameter. This approach however, becomes inaccurate as the new value moves away from the original values used for the reweighting, since the statistical fluctuations of the original sample get amplified. So, in this analysis, each term of the sum is generated individually, so that we can scale them continuously and independently from each other. This method is called the decomposition method, and it must be validated against samples that are generated normally, with all terms included at the same time, as shown in figure 4.1.

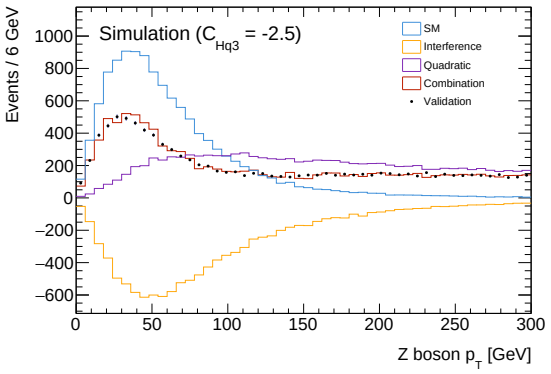

(a) Z boson p_T ($C_{Hq3} = -2.5$)

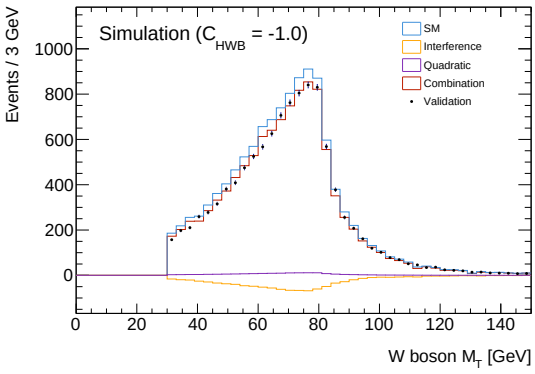

(b) W boson M_T ($C_{HWB} = -1.0$)

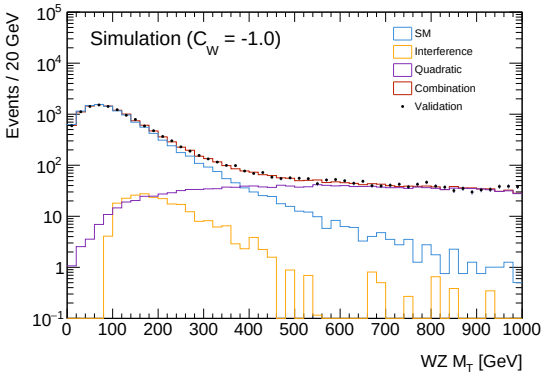

(c) WZ M_T ($C_W = -1.0$)

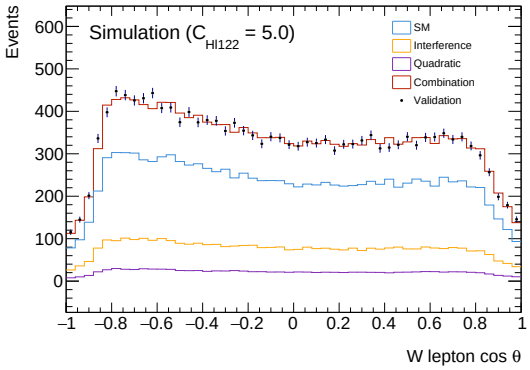

(d) W lepton $\cos\theta$ ($C_{Hl122} = 5.0$)

Figure 4.1: Examples of various validation plots. The different terms are generated as individual samples and rescaled to a certain value, and then combined and compared to a reference sample which was generated at that same value from the start and includes all the terms.

The validation of the decomposition method was made by taking various kinematic distributions and event topologies resulting from recombining the contributions of the different terms, and comparing them to the ones obtained by generating a sample in the usual way, with all terms included from the beginning. The comparison is performed for all the parameters at various values, to ensure agreement at various scales. The distributions were found to be in agreement up to statistical uncertainties.

In order to produce the separate sample terms, the specific generation options of MadGraph are used. An example of an event generation that includes all terms would be:

```
generate p p > l+ l- l+ vl NP<=1
```

where `NP<=1` indicates that the order of new physics at the amplitude level should be lower than or equal to 1. Using these options, we can generate a purely SM sample like this:

```
generate p p > l+ l- l+ vl NP==0 NP^2==0
```

Where `NP^2<=1` indicates that the order of new physics at the squared amplitude level has to be 0. An interference sample would look like this:

```
generate p p > l+ l- l+ vl NP^2==1
```

and a quadratic sample would look like this[1]:

```
generate p p > l+ l- l+ vl NP==1
```

The interference and quadratic samples should also specify the value of the parameter chosen, preferably having it set to 1, with all the others set to 0. This allows the samples to be rescaled more easily, by just multiplying the sample by C_i and C_i^2 respectively. One consequence of this is that while the quadratic sample is strictly positive, the interference sample can be negative depending on the value of C_i, as seen in plots (a) and (b) of figure 4.1. This means that the interference term acts as destructive interference with the rest of the events, leading to a lower combined cross section than that of the purely SM sample in some cases. This effect is only valid at small values of C_i, where the linear term dominates. At higher values of C_i, the quadratic term takes over, and the total cross section grows as C_i keeps growing. A consequence of this behavior, is that for all parameters there exists a value where the total cross section is the same as the cross section of a purely SM sample. Namely:

[1] A more detailed explanation of these options can be found in section 8.2.2 of reference [29].

$$\sigma_{SMEFT} = \sigma_{SM} + c_i \cdot \sigma_{INT} + c_i^2 \cdot \sigma_{QUAD} \tag{4.2}$$

$$\cancel{\sigma_{SM}} = \cancel{\sigma_{SM}} + c_i \cdot \sigma_{INT} + c_i^2 \cdot \sigma_{QUAD} \tag{4.3}$$

$$\Rightarrow c_i \cdot (\sigma_{INT} + c_i \cdot \sigma_{QUAD}) = 0 \tag{4.4}$$

$$\Rightarrow c_i = 0 \quad , \quad c_i = -\frac{\sigma_{INT}}{\sigma_{QUAD}} \tag{4.5}$$

The first solution is the trivial case where we recover the SM, and the second solution is the value in which the interference contribution cancels out exactly the quadratic contribution. This means that for fits based solely on cross section, there will be 2 solutions, or minima. This can be avoided by using variables that are independent of cross section.

In addition to the validation plots, the SMEFT samples were used to generate shape-analysis plots, where the distributions are reconstructed at various values of a parameter of choice to see the impact of this change in the shape of the distribution. These plots were used to study the sensitivity of each variable to the changes in the values of the SMEFT parameters.

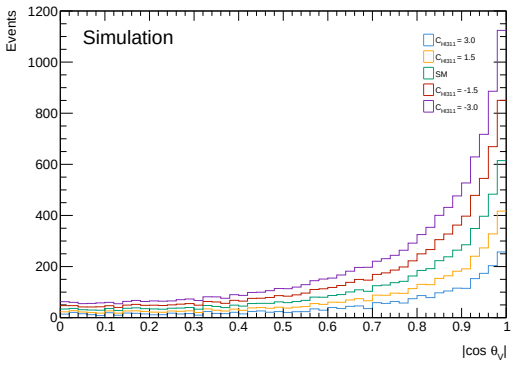

(a) $|\cos\theta_V|$ distributions for various values of the $C_{H\ell 311}$ parameter.

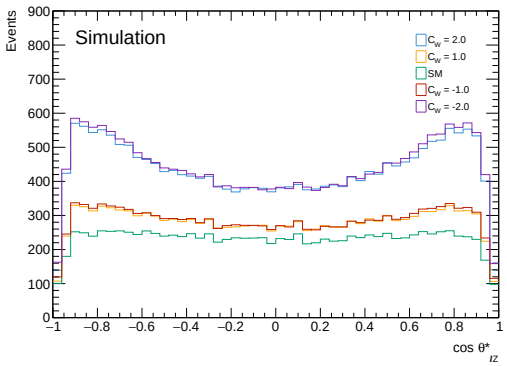

(b) $\cos\theta^*_{\ell Z}$ distributions for various values of the C_W parameter.

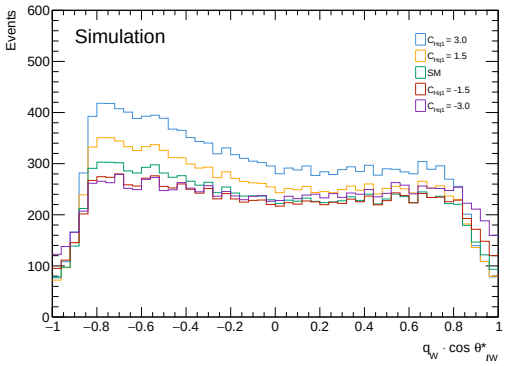

(c) $q_W \cdot \cos\theta^*_{\ell W}$ distributions for various values of the C_{Hq1} parameter.

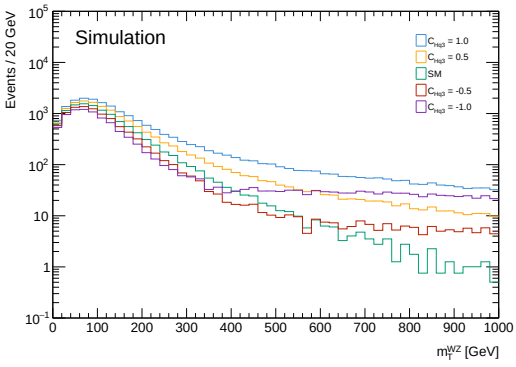

(d) m_T^{WZ} distributions for various values of the C_{Hq3} parameter.

Figure 4.2: Examples of shape-analysis plots. As the values of the parameters become more extreme, the difference between SM and SMEFT becomes more apparent.

5 Object and event selection

The raw data that ATLAS collects goes through various algorithms that convert the detector inputs into physics objects that can be used to do physics analyses. This is known as *reconstruction*. After that, we must choose which cuts to apply to the object in order to select the events of interest, and discard events that are unrelated. For this analysis, the final states that are possible for leptonic WZ events are:

- 3 electrons and a neutrino ($eee\nu$), where both the Z and the W decayed into electrons
- 2 electrons, 1 muon and 1 neutrino ($ee\mu\nu$), where the Z boson decayed into electrons and the W boson decays into a muon
- 1 electron, 2 muons and one neutrino ($e\mu\mu\nu$), where the Z boson decayed into muons, and the W boson decayed into an electron
- 3 muons and a neutrino ($\mu\mu\mu\nu$), where both the Z and the W decayed into muons

For this reason, appropriate triggers are selected, and kinematic cuts are applied to the leptons to select particles that are likely to have been produced by the decaying bosons of the event. Section 5.1 will describe the triggers used in the analysis. Sections 5.2 to 5.4 describe the reconstruction and selection cuts of the various objects used in the analysis, section 5.5 describes the phase space cuts used to ensure a correct final state, while section 5.6 describes the removal of overlapping objects.

5.1 Triggers

Given that all final states have leptons, the standard ATLAS single lepton triggers [33, 34] are used for this analysis:

Year	Electron triggers	Muon triggers
2015	`HLT_e24_lhmedium_L1EM20VH` *or* `HLT_e60_medium` *or* `HLT_e120_lhloose`	`HLT_mu20_iloose_L1MU15` *or* `HLT_mu50`
2016-2018	`HLT_e26_lhtight_nod0_ivarloose` *or* `HLT_e60_lhmedium_nod0` *or* `HLT_e140_lhloose_nod0`	`HLT_mu26_ivarmedium` *or* `HLT_mu50`

Table 5.1: Triggers by year of data taking.

5.2 Lepton object selection

Multiple leptons are produced in the collisions, which means that cuts must be applied to isolate our signal from the background. Similarly, some particles can be misidentified as leptons, so identification selections are applied to ensure the selected particles are the ones we want to study.

5.2.1 Electrons

Electrons in ATLAS are reconstructed from energy clusters in the EM calorimeter that have been matched to tracks in the Inner Detector. In order to determine whether the electron candidates are signal electrons or background objects (hadronic jets, converted photons), an algorithm for electron identification (ID) is applied [35]. The algorithm assigns working points based on a likelihood estimation, which uses the shape of the electromagnetic showers in the calorimeter, the track properties, as well as the track-to-cluster matching quality. In order of increasing background rejection, the identification working points are: *Loose*, *Medium* and *Tight*. For the baseline the Electrons are required to satisfy the *Medium* working point[1], which

[1] The choices of working points for electrons and muons were made in the ATLAS full Run-2 polarization paper [36, 37] which produced the HEPDATA that this analysis is based on.

gives us an identification efficiency of about 90%. Similarly to the ID selection, electron candidates are also assigned isolation working points, which indicate how well isolated from other particles the object is. There exist two classes of isolation working points: cut-based working points, which use only cuts on the calorimeter and track isolation cones, and efficiency-targeted working points, which instead are chosen so they ensure a target efficiency at given values of transverse energy (E_T) of the particle. Here, we use the *Gradient* working point from reference [35], of the second class, which ensures an efficiency of 90% at 25 GeV, and 99% at 60 GeV. Electron candidates are required to originate from the primary vertex of the event, have a transverse momentum (p_T) greater than 15 GeV, and have a pseudorapidity of $|\eta| < 1.37$ or $1.52 < |\eta| < 2.47$.

5.2.2 Muons

Muons in ATLAS are reconstructed using tracks measured in the MS that are then matched to tracks measured in the ID. Similarly to electrons, an algorithm is used to determine if the muon candidates should be categorized as signal or background [38]. Muons from W decays are considered signal, while muons from light-hadron decays are considered background. The algorithm assigns working points based on a likelihood estimation, which is calculated using the number of hits in the ID and the MS. Here we require muons to pass the “medium" identification selection, which gives an average selection efficiency of about 98%. The isolation working point for muons is again an efficiency-targeted working point called *Gradient* from reference [38], which ensures efficiency of 90% at $p_T > 25$ GeV and 99% at $p_T > 60$ GeV. Muons are also required to originate from the primary vertex, have a $p_T > 15$ GeV, and have a pseudorapidity $|\eta| < 2.5$.

5.3 Jet object selection

The quarks and gluons that are produced in the events create hadronic jets due to color-confinement, and while our final state particles don’t contain jets, they are necessary for the calculation of the missing transverse energy, which is used in the estimation of the neutrino p_T. In ATLAS, jets are reconstructed using a so-called “particle-flow" algorithm, which uses both tracking and calorimeter

information [39]. Tracks from the ID are selected and matched to topological clusters in the calorimeters, and the expected energy deposited (calculated from the track momentum) is subtracted from the calorimeter cells. If necessary, more topo-clusters are added to recover the full shower energy. This is applied to tracks in a descending p_T-order, until the remaining energy in the cells is consistent with shower fluctuations of a single particle, at which point the remaining topo-clusters are removed.

After the p-flow algorithm, the particles are bundled and reconstructed into jets using an anti-k_T algorithm [40] with radius parameter $R = 0.4$. All jets are required to have a $p_T > 25$ GeV and a pseudorapidity $|\eta| < 4.5$, and jets with $p_T < 60$ and $|\eta| < 2.4$ also required to pass a jet-vertex-tagger (JVT) [41] cut, which uses the tracks of the event and the vertex information to calculate the relative probability of a jet being of signal type. In particular, jets with a JVT value of 0.5 or higher are considered to be signal jets, and jets with lower values are considered pile-up.

5.4 Missing transverse energy

Since neutrinos pass through all the detector systems of ATLAS without being detected, a different approach is used. The colliding partons of the events are expected to have approximately 0 momentum in the transverse plane, since to an extremely good approximation, all of their momentum is in the longitudinal direction. A significant missing transverse energy E_T^{miss} would indicate the production of a particle that could not be detected by ATLAS, like neutrinos, or even some BSM particles. The E_T^{miss} is calculated as the negative vector sum of the momenta of all the hard objects (electrons, muons and jets), called the hard term, plus a contribution from soft-event signals, i.e. tracks associated with the primary vertex, but not with the hard objects, called the soft term.

$$\vec{E}_T^{\text{miss}} = -\sum_{\text{electrons}} \vec{p}_T^{\,e} - \sum_{\text{muons}} \vec{p}_T^{\,\mu} - \sum_{\text{jets}} \vec{p}_T^{\,\text{jet}} - \sum_{\substack{\text{soft}\\ \text{tracks}}} \vec{p}_T^{\,\text{track}} \tag{5.1}$$

While the longitudinal momentum p_Z^ν of the the neutrino can be reconstructed analytically using the W boson mass constraint, a better approach is to use a

neural network (NN). It has as inputs the transverse and longitudinal momentum of the charged lepton from the W boson decay, the E_T^{miss} components that are perpendicular and parallel to the direction of the lepton, as well as the analytical reconstruction of p_Z^ν mentioned previously. The NN is trained using WZ MC events, and is used to estimate the true longitudinal momentum p_Z^ν of the neutrino [36].

5.5 Phase space cuts

In addition to the selection cuts applied to the particles of the event, more cuts are used to ensure we have the correct final state particles and to suppress background events.

Events must contain exactly 3 lepton candidates satisfying the selection cuts mentioned above. Events are rejected if they contain a fourth lepton satisfying a set of looser criteria. If the 4th lepton has $p_T > 5$ GeV, and has *Loose* ID working point, then the event is rejected. This reduces background events with four leptons, like ZZ or $t\bar{t} + Z$.

Events are required to have a pair of same-flavored leptons with opposite charge, with an invariant mass ($m_{\ell\ell}$) consistent with the mass of the Z boson ($m_Z \approx 91.2\,\text{GeV}$) within 10 GeV. This pair is considered as the Z boson candidate. In case more than one pair can be formed (if all leptons have the same flavor, 2 pairs can be formed) the one whose $m_{\ell\ell}$ is closest to the Z boson mass pole is taken as the Z boson candidate.

The remaining lepton is assigned as a W boson decay product. In order to reduce background from misidentified leptons, this lepton is required to satisfy more stringent selection cuts: its $p_T > 20$ GeV, and must have the *Tight* ID working point. The transverse mass of the W boson is then calculated using the following formula:

$$m_T^W = \sqrt{2p_T^\ell p_T^\nu (1 - \cos\phi)} \tag{5.2}$$

Where p_T^ℓ is the lepton's transverse momentum, p_T^ν is the estimated transverse momentum of the neutrino based on the measured E_T^{miss}, and ϕ is the azimuthal

angle between the lepton and the $\vec{E}_T^{\text{miss}}$ vector. The transverse mass of the W boson must satisfy $m_T^W > 30$ GeV for the event to be selected.

5.6 Overlap removal

In order to avoid double counting objects, as well as eliminate fake or misidentified objects, a process of overlap removal is carried out, where reconstructed objects that are too close are removed. This is done in various steps:

- Jets within $\Delta R < 0.2$ of an electron decaying from a Z boson are discarded[2].
- Jets with fewer than 3 tracks and a distance $\Delta R < 0.2$ from the direction of a muon decaying from a Z boson are discarded.
- Baseline electrons sharing an ID track with a baseline muon are ignored.
- Electrons passing Z-selection cuts within $\Delta R < 0.4$ of a jet are discarded.
- Muons passing Z-selection cuts within $\Delta R < 0.4$ of a jet with at least 3 tracks are discarded.

[2] In ATLAS, ΔR is a measure of the angular distance between two objects, and is defined as: $\Delta R \equiv \sqrt{(\Delta\eta)^2 + (\Delta\phi)^2}$, where $\Delta\eta$ is the difference in pseudorapidity between the objects and $\Delta\phi$ is the difference between the azimuthal angles of the objects.

6 Systematic uncertainties

The samples used in this analysis are affected by various sources of systematic uncertainty. They can come from both experimental sources in the measurement of various particles, and from theoretical sources in the modeling of the simulations.

6.1 Experimental uncertainties

Experimental uncertainties arise from inaccuracies in a measurement, whether from an imperfect calibration or a limited detector resolution. In ATLAS, each source of experimental uncertainty is studied and characterized, so that the data-simulation agreement is as good as possible.

6.1.1 Luminosity

In the context of particle physics, luminosity is the ratio between the number N of events detected, with a given cross section σ during a certain period of time t:

$$L = \frac{1}{\sigma}\frac{\mathrm{d}N}{\mathrm{d}t} \tag{6.1}$$

This is also often called instantaneous luminosity, to differentiate it from integrated luminosity, another useful quantity, which is the integral of the previous formula with respect to time:

$$L_{int} = \int L \,\mathrm{d}t \tag{6.2}$$

Integrated luminosity can be used to describe the total amount of data collected by an experiment. This analysis used the Run 2 pp data of ATLAS, which after data-quality selections, recorded an integrated luminosity of $140.1 \pm 1.2\,\mathrm{fb}^{-1}$, with an uncertainty of 0.83% [42].

6.1.2 Electrons

Experimental uncertainties in electrons arise from energy calibration, identification, and isolation [43]. The uncertainty in energy calibration comes from the presence of detector material between the interaction point and the EM calorimeter, as well as pile-up noise, and amounts to 0.05% in the barrel and 0.15% in the endcap. The uncertainties from electron identification are dominated by background subtraction uncertainties at low E_T, and are ±7% at $E_T = 4.5$ GeV, decreasing with transverse energy, reaching ±1% at $E_T > 30$ GeV. The isolation uncertainties are obtained via tag-and-probe measurements of $Z \rightarrow ee$ and $J/\Psi \rightarrow ee$ events, and range from about 5% for electrons with $E_T < 7$ GeV, and reach less than 0.5% at higher E_T.

6.1.3 Muons

Experimental uncertainties in muons arise from momentum calibration, reconstruction, identification, and isolation [38]. Uncertainties in momentum calibration come from inaccuracies in the modeling of the magnetic field integral, inaccuracies in the dimension of the detector in the direction perpendicular to the magnetic field, and inaccuracies in the simulation of energy loss in the calorimeter and detector materials between the IP and the MS. These uncertainties amount to a minimum of 0.05% for $|\eta| < 1$ up to a maximum of 0.3% for $|\eta| \sim 2.5$. The uncertainties in identification and reconstruction are studied using tag-and-probe methods on $Z \rightarrow \mu\mu$ and $J/\Psi \rightarrow \mu\mu$ events, where an agreement better than 0.1% is observed at high p_T, growing at lower values of p_T up to 0.7%, where the background contribution is most significant. A larger effect is observed in the $|\eta| < 0.1$ region, where coverage of the MS is incomplete, up to a $1-2$% uncertainty. The $Z \rightarrow \mu\mu$ tag-and-probe method is also used for the muon isolation uncertainties, which are at the per mille level over most p_T values, only reaching a percent level at the high-p_T region.

6.1.4 Jets

The uncertainties regarding jets come from inaccuracies in energy scale, as well as energy resolution [44]. These are derived using various methods, which include

Z+jet balance, γ+jet balance, multijet balance, dijet η-intercalibration, and more. This adds up to 80 uncertainty sources, which for this study are reduced to 30 nuisance parameters (NPs) that affect the jet energy scale, and 8 NPs that affect the jet energy resolution.

6.1.5 Missing transverse energy

The uncertainties on the E_T^{miss} come from its energy scale and resolution, and depend on the composition of the hard terms and the magnitude of the corresponding soft term [45]. The contributions from the hard objects (electrons, muons and jets) are the same that have already been explained. The scale and resolution uncertainties from the soft term are obtained by comparing a spectrum of observables in data to MC samples, and measuring the contribution of the soft term to the overall E_T^{miss}.

6.1.6 Pileup

Simulated data are produced with a specific value of pileup. In order to more closely emulate real data, this pileup is reweighted so its distribution resembles the pileup of the period the data was taken. In addition to this reweighting, a variation is included to cover the uncertainty in the ratio between the predicted and the measured pp inelastic cross sections [46].

6.1.7 Unfolding

The unfolding process requires the generation of MC samples that are used to model detector effects as a response matrix, which transforms the "true" data into the measured data. To obtain the response matrix, the background is subtracted from the data, which is then corrected for detector resolution and efficiencies using simulated signal samples and an iterative Bayesian unfolding method [17], ranging from 2 to 4 iterations depending on the variable, giving as result a response matrix. This process has uncertainties that come from an imperfect description of the data by the MC samples, as well as from the size of the MC sample. The uncertainties

are evaluated using a data-driven method, based on truth-reco matched events [47].

6.2 Theoretical uncertainties

In addition to the experimental uncertainties, there are uncertainties arising from theory aspects, whether it be incomplete or truncated modeling, variations in the numerical models (PDF uncertainties), or uncertainties in the values of physical constants.

6.2.1 Scale uncertainties

To model the missing higher-order QCD corrections in the simulated samples, the renormalization and factorization scales (μ_R and μ_F) are scaled by 0.5 and 2, using 7 different combinations of them:

$$\{\mu_R, \mu_F\} = \{0.5, 0.5\}, \{1, 0.5\}, \{0.5, 1\}, \{1, 1\}, \{2, 1\}, \{1, 2\}, \{2, 2\} \tag{6.3}$$

The uncertainties of these 7 pairs are combined by taking an envelope of all of them, where the maximum of differences between the scale variations and the central value is taken. This follows the recommendations of the ATLAS Physics Modelling Group (PMG).

6.2.2 PDF uncertainties

The choice of PDF has an associated uncertainty, which is calculated by comparing various PDF sets, as recommended by the PDF4LHC group [48]. The formula used to calculate this is:

$$\delta^{PDF}\sigma = \sqrt{\frac{1}{N-1}\sum_{k=1}^{N}\left(\sigma^{(k)} - \langle\sigma\rangle\right)} \tag{6.4}$$

where $\delta^{PDF}\sigma$ is the 68% confidence level PDF uncertainty, σ is the observable of choice, N is the number of MC replicas that use the various PDF sets, and $\langle\sigma\rangle$ is the mean value of the observable over the MC replicas.

6.2.3 α_S uncertainties

The QCD running coupling α_S (related to the fundamental strong coupling g_S introduced in Subsection 2.1.2 by $\alpha_S = \frac{g_S^2}{4\pi}$) depends on the square of the energy scale of the process. The usual scale used to determine α_S is the mass of the Z boson m_Z, but this choice still has an uncertainty associated with it. The value used is:

$$\alpha_S(m_Z^2) = 0.1180 \pm 0.0009 \tag{6.5}$$

which is the PDF global average [49]. The effect of the α_S uncertainty in the PDFs is then obtained by using variations in $\pm 1\sigma$ of $\alpha_S \pm 0.001$.

7 Statistical analysis

The analysis of the samples is done using statistical methods to set limits on the Wilson coefficients of the various SMEFT couplings that are being studied. This chapter will explain the statistical model used in Section 7.1, then will explore the likelihood function used in Section 7.2, and finally will discuss the estimation of confidence intervals in Section 7.3.

7.1 Statistical model

This analysis uses binned distributions, where the expected differential cross section per bin is compared to the unfolded differential cross section in each bin. Given what has been explained in chapter 4, and assuming only one non-zero Wilson coefficient c_i at a time, the expected differential cross section per bin is:

$$\sigma_b^{\text{pred}} = \left(\sigma_b^{\text{SM}} + \sigma_b^{\text{int}}\, c_i + \sigma_b^{\text{quad}} c_i^2\right) \cdot \prod_j^{n_{syst}} (1 + \theta_j \delta_{jb}) \tag{7.1}$$

where σ_b^{SM} is the expected differential cross section of SM events per bin, σ_b^{int} is the expected differential cross section per bin coming from SM-SMEFT interference when c_i is assumed to be 1, σ_b^{quad} is the expected differential cross section of events per bin coming from SMEFT self-interaction when c_i is assumed to be 1, n_{syst} is the number of nuisance parameters used in the fit, θ_j is the j-th nuisance parameter, and δ_{bj} are the fractional uncertainties for the systematic j in the bin b.

7.2 Likelihood function

The limits of the Wilson coefficients are derived using a binned maximum likelihood, fitting the predicted differential cross section to the unfolded differential cross section. The fit is performed with the `eft-fun` framework [50], which uses a likelihood function given by a multivariate Gaussian representing the difference between measurements and predictions, that is multiplied by a Gaussian constraint term for each nuisance parameter included in the fit. So, assuming a distribution with n bins, the likelihood as a function of c_i, which will be minimized in the fit is then:

$$L(\sigma|c_i,\theta) = \frac{1}{\sqrt{(2\pi)^n|C|}} \cdot \exp\Big(-\frac{1}{2}\Delta\vec{\sigma}^T C^{-1}\Delta\vec{\sigma}\Big) \cdot \prod_j \text{Gauss}(\theta_j) \tag{7.2}$$

where C is the $n\times n$ covariance matrix between bins, $\text{Gauss}(\theta_j)$ is the Gaussian constraint of the j-th nuisance parameter, and $\Delta\vec{\sigma}$ is given by:

$$\Delta\vec{\sigma} = \vec{\sigma}^{data} - \vec{\sigma}^{pred} \tag{7.3}$$

and is the difference between unfolded differential cross section $\vec{\sigma}^{data}$ and the predicted differential cross section $\vec{\sigma}^{pred}$, both expressed as vectors of length n where each component represents the bin content of the distribution.

7.3 Profile likelihood test and confidence intervals

While the likelihood function can be used to find a minimum that produces the best fit between prediction and data, a profile likelihood test (PLT) is used to estimate confidence intervals of that result. This test is constructed as the following equation:

$$\lambda(c_i) = -2\log\frac{L(\sigma|c_i,\hat{\hat{\theta}})}{L(\sigma|\hat{c}_i,\hat{\theta})} \tag{7.4}$$

where $\hat{\hat{\theta}}$ is the best fit-value of the nuisance parameters for a fixed value of c_i, while $\hat{\theta}$ and $\hat{c}_i$ are the unconditional maximum likelihood estimates of the nuisance parameters and c_i respectively. This PLT is used to scan over a range of values of c_i, which results in a likelihood curve. This likelihood curve follows a χ^2 distribution with one degree of freedom, which at 95% confidence has a critical value of 3.84, meaning that the values of c_i at which the curve crosses this value of $\lambda(c_i)$ will be the 95% C.I.

8 Results

The results are obtained by comparing expected and unfolded distributions of 4 variables:

- $|\cos\theta_V|$: the absolute value of the cosine of the production angle (θ_V) of the bosons relative to the beam line, in the WZ rest frame.
- $\cos\theta^*_{\ell Z}$: the cosine of the angle of the negatively-charged lepton that resulted from the decay of the Z boson, with respect to the Z boson's direction, in the rest frame of the Z boson.
- $q_W \cdot \cos\theta^*_{\ell W}$: the charge of the lepton that resulted from the decay of the W boson, multiplied by the cosine of its angle with respect to the W boson's direction, in the rest frame of the W boson.
- m_T^{WZ}: the transverse mass-like of the WZ system, defined as:

$$m_T^{WZ} = \sqrt{\left(\sum_\ell p_T^\ell + E_T^{\text{miss}}\right)^2 + \left(\sum_\ell \vec{p}_T^{\,\ell} + \vec{E}_T^{\text{miss}}\right)^2}$$

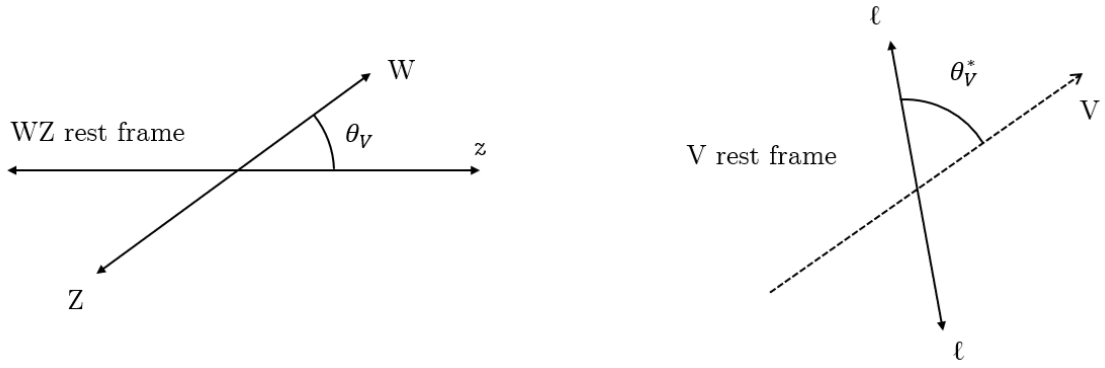

Figure 8.1: Diagram showing the angle θ_V in the WZ rest frame on the left, and $\theta^*_{\ell V}$ in the rest frame of the vector boson V on the right.

The three angular variables are defined to be completely uncorrelated with each other (with the exception of their dependence on the total cross section, which can be removed by normalizing the distributions). These distributions, along with the m_T^{WZ} distribution have been unfolded to particle level, to be compared to the expected decomposition SMEFT samples. The comparison uses the profile likelihood test from Section 7.3, and is repeated for the 12 parameters, and the 4 variables, giving a total of 48 tests. Some examples are given in Figure 8.2.

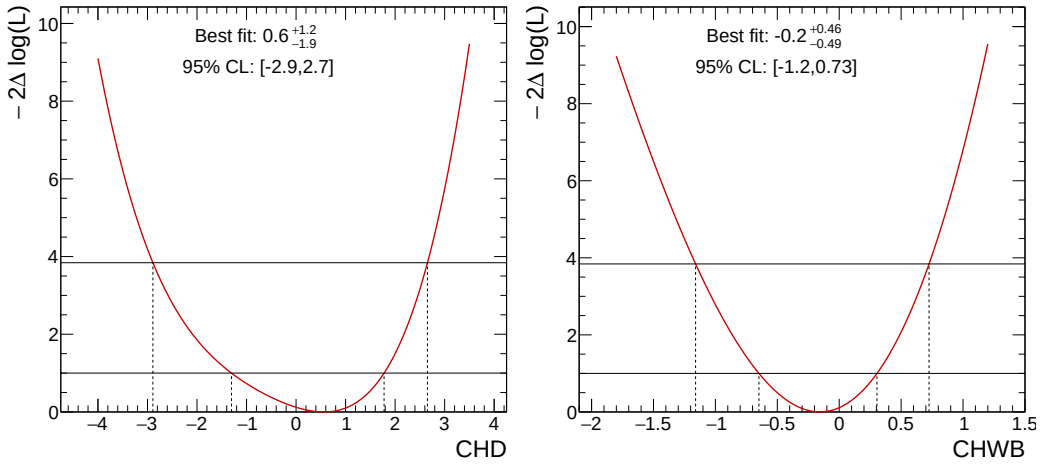

(a) PLT of C_{HD} using $|\cos\theta_V|$ distribution (b) PLT of C_{HWB} using $\cos\theta^*_{\ell Z}$ distribution

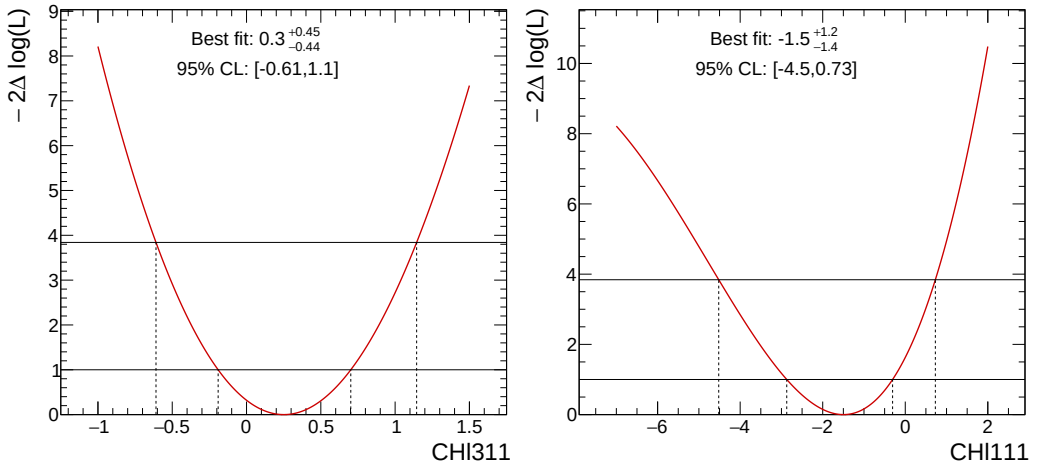

(c) PLT of C_{Hl311} using $q_W \cdot \cos\theta^*_{\ell W}$ distri-(d) PLT of $C_{H\ell 111}$ using m_T^{WZ} distribution
bution

Figure 8.2: Profile likelihood tests for various example parameters, with their corresponding best fits and 95% CL predictions. The full set of PLT can be found in Appendix A.

The first 3 variables make use of the entire dataset, as the `eft-fun` framework makes use of the distributions from the HEPDATA from the ATLAS full Run-2 polarization paper [36, 37]. The fourth variable, m_T^{WZ} only makes use of a partial Run-2 dataset of 36.1 fb^{-1} [51, 52].

As mentioned at the end of Chapter 4, some fits that are correlated to the total cross section will have 2 minima: one centered around 0, and one centered around the value where the interference term cancels out with the quadratic term. For illustration purposes, the HEPDATA distributions used in the PLT are compared to the 95% CL distributions, shown in Figure 8.3. The results of the 48 PLT are summarized in Figure 8.4.

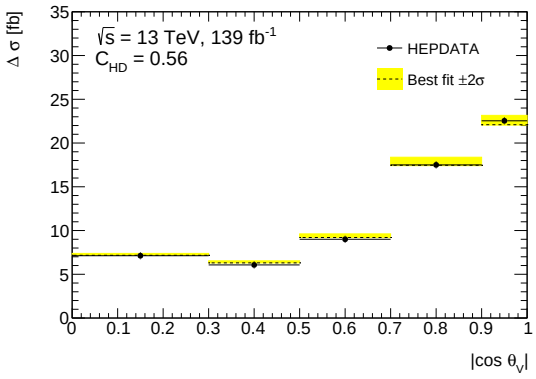

(a) $|\cos\theta_V|$, HEPDATA vs C_{HD} 95% CL

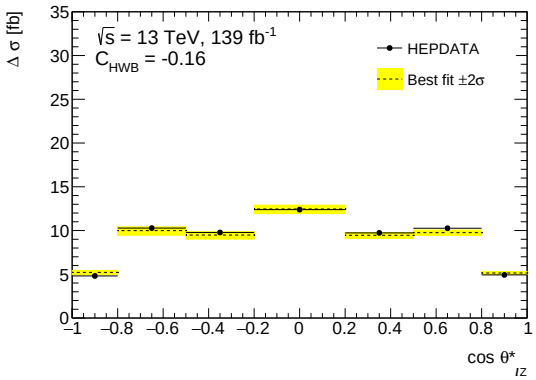

(b) $\cos\theta^*_{\ell Z}$, HEPDATA vs C_{HWB} 95% CL

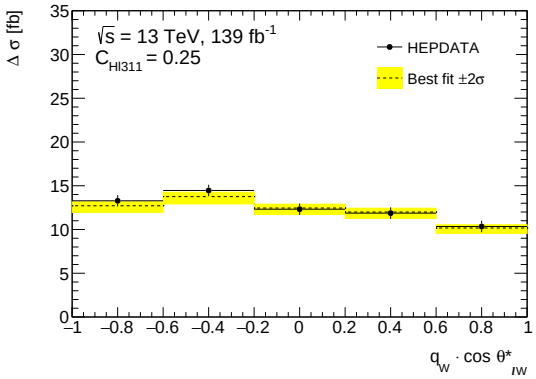

(c) $q_W \cdot \cos\theta^*_{\ell W}$, HEPDATA vs C_{Hl311} 95% CL

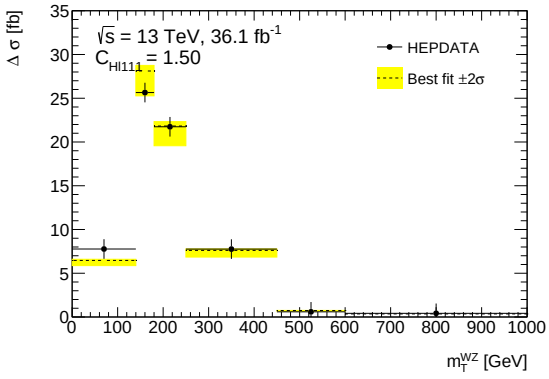

(d) m_T^{WZ}, HEPDATA vs $C_{H\ell 111}$ 95% CL

Figure 8.3: HEPDATA distributions of the ATLAS Run-2 data published in [37, 52] compared to the 95% CL predictions for various example parameters. The full set of plots can be found in Appendix B.

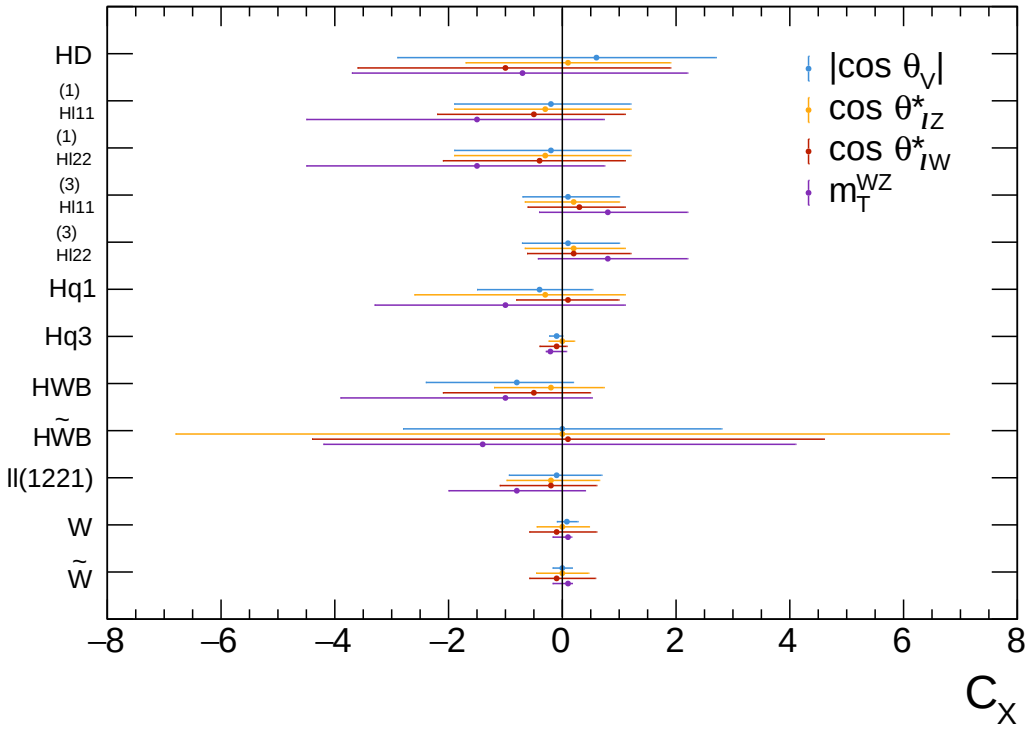

Figure 8.4: Summary plot of the best fits and 95% CL for the 12 SMEFT parameters, based on the PLT of the 4 variables.

It can be seen that the results are compatible with SM predictions. The limits for $C^{(1)}_{H\ell 11}$ and $C^{(1)}_{H\ell 22}$ are almost identical, and the same can be seen for $C^{(3)}_{H\ell 11}$ and $C^{(3)}_{H\ell 22}$. This can be explained by the fact that these operators affect production of pairs of leptons, and measure violations in lepton flavor universality. However, the HEPDATA dataset used assumes lepton flavor universality and doesn't separate the events based on the decay products, so the limits obtained are not independent. In most cases, the predictions based on angular distributions ($|\cos\theta_V|$, $\cos\theta^*_{\ell Z}$ and $q_W \cdot \cos\theta^*_{\ell W}$) provide more stringent limits than the prediction based on the kinematic variable m_T^{WZ}. This is explained by the difference in the dataset used, since the m_T^{WZ} fits use the distributions from [51, 52], which are unfolded to particle level but use only a partial Run-2 dataset, about a fourth of the total used for the other distributions. Given how the angular distributions have little dependence on the energy of the process when compared to kinematic variables such as m_T^{WZ} or the W and Z p_T, this approach would be advantageous in studies where the center-of-mass energy is the same but the integrated luminosity is increased, as is expected to be the case from the High-Luminosity-LHC. Even in

studies where the energy of the process is increased, angular distributions can be useful in multi-dimensional analyses, where two or more SMEFT parameters are allowed to vary at the same time. This is because while the distributions of the kinematic variables of SMEFT samples scale in similar ways, with increases in the high-pT tails, the angular distributions of different SMEFT samples will have different shapes (see Figure 4.2), allowing one to disentangle the SMEFT contributions from different SMEFT parameters.

9 Conclusions

With the discovery of the Higgs boson in 2012 at the LHC, the main lead that particle physicists had been following was reached, and since then, the focus has shifted to the search for new physics beyond the Standard Model, in what some call the precision era. This is being done through direct searches for new particles, as well as indirect searches, that look for any difference between the data and the SM predictions which could hint at new physics, akin to "stress-testing" the SM. The advantage of indirect searches is that they do not rely on specific assumptions about the nature of the new physics, which broadens the search. SMEFT is one such approach, where even small differences are parametrized and put to test in various experiments. This study focused on the electroweak parameters of SMEFT that affect the WWZ triple gauge coupling, using data from the ATLAS experiment.

The Standard Model has been very successful in explaining a multitude of phenomena in particle physics, but it unfortunately falls short of being a theory of everything, failing to explain one of the main forces of the universe, as well as various other phenomena. This is outlined in Chapter 2, where the Standard Model Effective Field Theory, or SMEFT is also introduced. This model, more than attempting to explain the unanswered questions of the SM, tries to expand the SM in a very general way, assuming that the high energy theory that explains everything is still out of our experimental reach, while still trying to measure the effects this theory could have at low energies. For this purpose, the ATLAS detector at the Large Hadron Collider, outlined in Chapter 3, was used to obtain data. This data was collected from 2015 to 2018 at $\sqrt{s} = 13$ TeV, with an integrated luminosity of 139 fb^{-1}. Three of the four variables used in the analysis were unfolded in another study using the entire dataset, while the remaining variable was unfolded in a different study, which used only a partial dataset. The Monte-Carlo samples used in the analysis consisted of various background samples (multiboson, top production, and gauge boson with jets of photons), while signal samples consisted of an NLO

SM sample with NNLO corrections, and one SMEFT interference sample and one SMEFT quadratic sample for each parameter in the analysis. These samples made use of the decomposition method, where the contributions of terms of different order in the new physics parameter are simulated independently, and can be rescaled and added together to obtain valid new samples. This decomposition method had to be tested, validated, and was compared to other methods such as reweighting, before being chosen as the method of this study. The data, the MC samples, and the decomposition method are explored in Chapter 4. Chapter 5 describes the four possible final states of the events of interest, as well as the various objects used in the analysis and how both the events and the objects are selected. Special consideration is given to electrons, muons and E_T^{miss}, since all final events are expected to contain 3 leptons and a neutrino. Triggers, jets, overlap removal, and phase space cuts are also explained. The object and event selections used for the unfolded samples was compared to detector-simulated samples that were analyzed with an Athena-based framework, as the analysis originally was meant to use reconstructed samples, before switching to unfolded distributions. Chapter 6 then provides an overview of the systematic uncertainties that affect this analysis. These include luminosity, electron, muon, jet, E_T^{miss}, pileup and unfolding uncertainties as sources of experimental uncertainties, as well as scale, PDF and α_s uncertainties as sources of theoretical uncertainties. The details about the statistical methods used in the analysis are described in Chapter 7. The statistical model is based on binned distributions describing the expected differential cross section. A likelihood function is constructed based on this statistical model, which is used to minimize the difference between the measured data and the predictions, giving a best fit for the value of each of the parameters of this study, as well as 95% confidence intervals.

This analysis measured limits on a large set of EFT coefficients. The limits obtained here are in line with previous results from ATLAS and other experiments, with 3 of the parameter limits being set quite tight: C_{Hq3}, C_W and $C_{\tilde{W}}$. Whereas past studies have focused on event counts at higher p_T, this study has focused on angular distributions. These provide new ways to observe deviations from the SM, and could indicate differences in symmetry group, spin, parity or polarization.

After Run 3, the LHC and its detectors will undergo several upgrades to reach an increase of 10 times of the current integrated luminosity. The average number of pileup interactions per bunch crossing is expected to increase up to 200, and to be able to keep optimal functions, ATLAS is scheduled to receive upgrades to

various detector subsystems, and these upgrades, alongside the enormous increase in collected data, are expected to improve even more the limits that can be obtained in this study and others similar to it. By increasing the number of events, it allows the usage of finer binning and also reduced statistical uncertainty. These improvements are necessary for the exploration of new frontiers for physicists, pushing the precision of the Standard Model to its limits, to find what has remained hidden thus far.

Bibliography

[1] Cush, *Standard Model of Elementary Particles*, https://en.wikipedia.org/wiki/File:Standard_Model_of_Elementary_Particles.svg, Public domain, via Wikimedia Commons, 2019.

[2] E. C. G. Sudarshan, *The fundamental theorem on the relation between spin and statistics*, Proceedings of the Indian Academy of Sciences - Section A **67** (1968) 284, ISSN: 0370-0089, URL: https://doi.org/10.1007/BF03049366.

[3] S. Navas et al., *Review of particle physics*, Phys. Rev. D **110** (2024) 030001.

[4] M. E. Peskin and D. V. Schroeder, *An Introduction to Quantum Field Theory*, Reading, USA: Addison-Wesley, 1995, ISBN: 978-0-201-50397-5, 978-0-429-50355-9, 978-0-429-49417-8.

[5] J. C. ROMÃO and J. P. SILVA, *A RESOURCE FOR SIGNS AND FEYNMAN DIAGRAMS OF THE STANDARD MODEL*, International Journal of Modern Physics A **27** (2012) 1230025, ISSN: 1793-656X, URL: http://dx.doi.org/10.1142/S0217751X12300256.

[6] B. Grzadkowski, M. Iskrzyński, M. Misiak and J. Rosiek, *Dimension-six terms in the Standard Model Lagrangian*, Journal of High Energy Physics **2010** (2010), ISSN: 1029-8479, URL: http://dx.doi.org/10.1007/JHEP10(2010)085.

[7] A. Dedes, W. Materkowska, M. Paraskevas, J. Rosiek and K. Suxho, *Feynman rules for the Standard Model Effective Field Theory in R -gauges*, Journal of High Energy Physics **2017** (2017), ISSN: 1029-8479, URL: http://dx.doi.org/10.1007/JHEP06(2017)143.

[8] F. Landua, *The CERN accelerator complex layout in 2022. Complexe des accélérateurs du CERN en janvier 2022*, (2022), General Photo, URL: https://cds.cern.ch/record/2813716.

[9] J. Pequenao and P. Schaffner, 'How ATLAS detects particles: diagram of particle paths in the detector', 2013, URL: https://cds.cern.ch/record/1505342.

[10] J. Pequenao, 'Computer generated image of the ATLAS inner detector', 2008, URL: https://cds.cern.ch/record/1095926.

[11] ATLAS Collaboration, 'Experiment Briefing: Keeping the ATLAS Inner Detector in perfect alignment', General Photo, 2020, URL: https://cds.cern.ch/record/2723878.

[12] J. Pequenao, 'Computer Generated image of the ATLAS calorimeter', 2008, URL: https://cds.cern.ch/record/1095927.

[13] J. Pequenao, 'Computer generated image of the ATLAS Muons subsystem', 2008, URL: https://cds.cern.ch/record/1095929.

[14] ATLAS Collaboration, *The ATLAS Experiment at the CERN Large Hadron Collider*, JINST **3** (2008) S08003, URL: https://dx.doi.org/10.1088/1748-0221/3/08/S08003.

[15] ATLAS Collaboration, *Determination of the parton distribution functions of the proton from ATLAS measurements of differential W± and Z boson production in association with jets*, Journal of High Energy Physics **2021** (2021), ISSN: 1029-8479, URL: http://dx.doi.org/10.1007/JHEP07(2021)223.

[16] ATLAS Collaboration, 'Public ATLAS Luminosity Results for Run-2 of the LHC', URL: https://twiki.cern.ch/twiki/bin/view/AtlasPublic/LuminosityPublicResultsRun2.

[17] G. D'Agostini, *A multidimensional unfolding method based on Bayes' theorem*, Nucl. Instrum. Meth. A **362** (1995) 487, ISSN: 0168-9002.

[18] P. Nason, *A new method for combining NLO QCD with shower Monte Carlo algorithms*, JHEP **11** (2004) 040, arXiv: hep-ph/0409146.

[19] S. Frixione, P. Nason and C. Oleari, *Matching NLO QCD computations with parton shower simulations: the POWHEG method*, JHEP **11** (2007) 070, arXiv: 0709.2092 [hep-ph].

[20] S. Alioli, P. Nason, C. Oleari and E. Re, *A general framework for implementing NLO calculations in shower Monte Carlo programs: the POWHEG BOX*, JHEP **06** (2010) 043, arXiv: 1002.2581 [hep-ph].

[21] P. Nason and G. Zanderighi, *W^+W^-, WZ and ZZ production in the POWHEG-BOX-V2*, Eur. Phys. J. C **74** (2014) 2702, arXiv: 1311.1365 [hep-ph].

[22] T. Sjöstrand et al., *An introduction to PYTHIA 8.2*, Comput. Phys. Commun. **191** (2015) 159, arXiv: 1410.3012 [hep-ph].

[23] ATLAS Collaboration, *Measurement of the Z/γ^* boson transverse momentum distribution in pp collisions at $\sqrt{s} = 7$ TeV with the ATLAS detector*, JHEP **09** (2014) 145, arXiv: 1406.3660 [hep-ex].

[24] H.-L. Lai et al., *New parton distributions for collider physics*, Phys. Rev. D **82** (2010) 074024, arXiv: 1007.2241 [hep-ph].

[25] J. Pumplin et al., *New Generation of Parton Distributions with Uncertainties from Global QCD Analysis*, JHEP **07** (2002) 012, arXiv: hep-ph/0201195.

[26] M. Grazzini, S. Kallweit and M. Wiesemann, *Fully differential NNLO computations with MATRIX*, Eur. Phys. J. C **78** (2018) 537, arXiv: 1711.06631 [hep-ph].

[27] J. Alwall et al., *The automated computation of tree-level and next-to-leading order differential cross sections, and their matching to parton shower simulations*, JHEP **07** (2014) 079, arXiv: 1405.0301 [hep-ph].

[28] I. Brivio, Y. Jiang and M. Trott, *The SMEFTsim package, theory and tools*, Journal of High Energy Physics **2017** (2017), ISSN: 1029-8479, URL: http://dx.doi.org/10.1007/JHEP12(2017)070.

[29] I. Brivio, *SMEFTsim 3.0 — a practical guide*,
Journal of High Energy Physics **2021** (2021), ISSN: 1029-8479,
URL: http://dx.doi.org/10.1007/JHEP04(2021)073.

[30] NNPDF Collaboration, R. D. Ball et al.,
Parton distributions for the LHC run II, JHEP **04** (2015) 040,
arXiv: 1410.8849 [hep-ph].

[31] E. Bothmann et al., *Event generation with Sherpa 2.2*,
SciPost Phys. **7** (2019) 034, arXiv: 1905.09127 [hep-ph].

[32] ATLAS Collaboration, *ATLAS Pythia 8 tunes to 7 TeV data*,
ATL-PHYS-PUB-2014-021 (2014),
URL: https://cds.cern.ch/record/1966419.

[33] ATLAS Collaboration,
Performance of electron and photon triggers in ATLAS during LHC Run 2,
Eur. Phys. J. C **80** (2020) 47, arXiv: 1909.00761 [hep-ex].

[34] ATLAS Collaboration, *Performance of the ATLAS muon triggers in Run 2*,
JINST **15** (2020) P09015,
arXiv: 2004.13447 [physics.ins-det].

[35] ATLAS Collaboration, *Electron efficiency measurements with the ATLAS detector using the 2015 LHC proton–proton collision data*,
ATLAS-CONF-2016-024, 2016,
URL: https://cds.cern.ch/record/2157687.

[36] ATLAS Collaboration,
Observation of gauge boson joint-polarisation states in $W^{\pm}Z$ production from pp collisions at $\sqrt{s} = 13$ TeV with the ATLAS detector,
Phys. Lett. B **843** (2023) 137895, arXiv: 2211.09435 [hep-ex].

[37] ATLAS Collaboration,
Observation of gauge boson joint-polarisation states in $W^{\pm}Z$ production from pp collisions at $\sqrt{s} = 13$ TeV with the ATLAS detector,
HEPData (collection),
https://doi.org/10.17182/hepdata.135074, 2023.

[38] ATLAS Collaboration, *Muon reconstruction performance of the ATLAS detector in proton–proton collision data at $\sqrt{s} = 13$ TeV*,
Eur. Phys. J. C **76** (2016) 292, arXiv: 1603.05598 [hep-ex].

[39] ATLAS Collaboration, *Jet reconstruction and performance using particle flow with the ATLAS Detector*, Eur. Phys. J. C **77** (2017) 466, arXiv: 1703.10485 [hep-ex].

[40] M. Cacciari, G. P. Salam and G. Soyez, *The anti-k_t jet clustering algorithm*, JHEP **04** (2008) 063, arXiv: 0802.1189 [hep-ph].

[41] ATLAS Collaboration, *Performance of pile-up mitigation techniques for jets in pp collisions at $\sqrt{s} = 8$ TeV using the ATLAS detector*, Eur. Phys. J. C **76** (2016) 581, arXiv: 1510.03823 [hep-ex].

[42] ATLAS Collaboration, *Luminosity determination in pp collisions at $\sqrt{s} = 13$ TeV using the ATLAS detector at the LHC*, Eur. Phys. J. C **83** (2023) 982, arXiv: 2212.09379 [hep-ex].

[43] ATLAS Collaboration, *Electron and photon performance measurements with the ATLAS detector using the 2015–2017 LHC proton–proton collision data*, JINST **14** (2019) P12006, arXiv: 1908.00005 [hep-ex].

[44] ATLAS Collaboration, *Jet energy scale measurements and their systematic uncertainties in proton–proton collisions at $\sqrt{s} = 13$ TeV with the ATLAS detector*, Phys. Rev. D **96** (2017) 072002, arXiv: 1703.09665 [hep-ex].

[45] ATLAS Collaboration, *Performance of missing transverse momentum reconstruction with the ATLAS detector using proton–proton collisions at $\sqrt{s} = 13$ TeV*, Eur. Phys. J. C **78** (2018) 903, arXiv: 1802.08168 [hep-ex].

[46] ATLAS Collaboration, *Measurement of the Inelastic Proton–Proton Cross Section at $\sqrt{s} = 13$ TeV with the ATLAS Detector at the LHC*, Phys. Rev. Lett. **117** (2016) 182002, arXiv: 1606.02625 [hep-ex].

[47] B. Malaescu, *An Iterative, Dynamically Stabilized (IDS) Method of Data Unfolding*, en, 2011, URL: http://cds.cern.ch/record/1365693.

[48] J. Butterworth et al., *PDF4LHC recommendations for LHC Run II*, J. Phys. G **43** (2016) 023001, arXiv: 1510.03865 [hep-ph].

[49] S. Navas et al., *Review of Particle Physics*, Phys. Rev. D **110** (3 2024) 030001, URL: https://link.aps.org/doi/10.1103/PhysRevD.110.030001.

[50] 'EFT-fun framework', URL: https://gitlab.cern.ch/eft-tools/eft-fun/blob/master/EFTfit.md.

[51] ATLAS Collaboration, *Measurement of $W^{\pm}Z$ production cross sections and gauge boson polarisation in pp collisions at $\sqrt{s} = 13$ TeV with the ATLAS detector*, Eur. Phys. J. C **79** (2019) 535, arXiv: 1902.05759 [hep-ex].

[52] ATLAS Collaboration, *Measurement of $W^{\pm}Z$ production cross sections and gauge boson polarisation in pp collisions at $\sqrt{s} = 13$ TeV with the ATLAS detector*, HEPData (collection), https://doi.org/10.17182/hepdata.83701, 2019.

[53] ATLAS Collaboration, *ATLAS Level-1 Muon Trigger Public Results*, URL: https://twiki.cern.ch/twiki/bin/view/AtlasPublic/L1MuonTriggerPublicResults.

[54] A. Canesse, 'Small-Strip Thin Gap Chambers for the Muon Spectrometer Upgrade of the ATLAS Experiment', *Proceedings of The Eighth Annual Conference on Large Hadron Collider Physics — PoS(LHCP2020)*, vol. 382, (2020) 245, URL: https://pos.sissa.it/382/245/.

[55] F. Lanni, 'ATLAS team with the first fully-assembled New Small Wheel', General Photo, 2021, URL: https://cds.cern.ch/record/2771290.

A Profile likelihood tests

A.1 $|\cos\theta_V|$

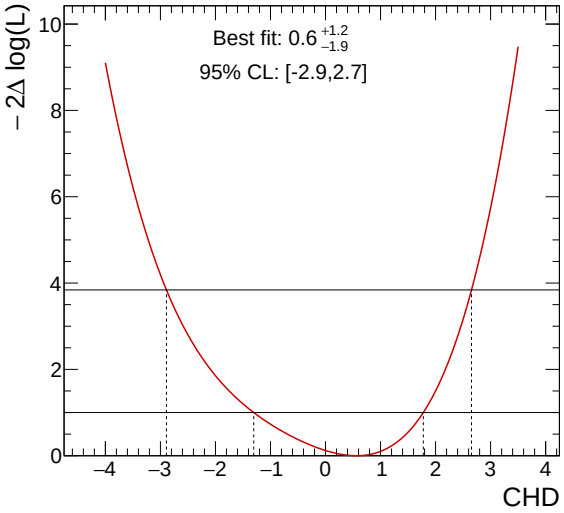

(A.1.1) PLT of C_{HD} using $|\cos\theta_V|$ distribution

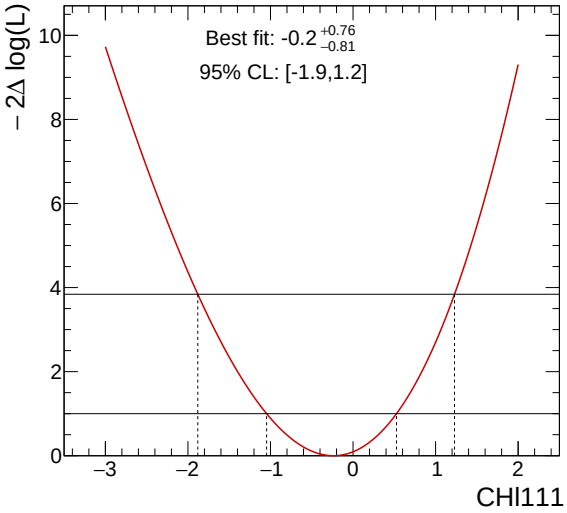

(A.1.2) PLT of C_{Hl111} using $|\cos\theta_V|$ distribution

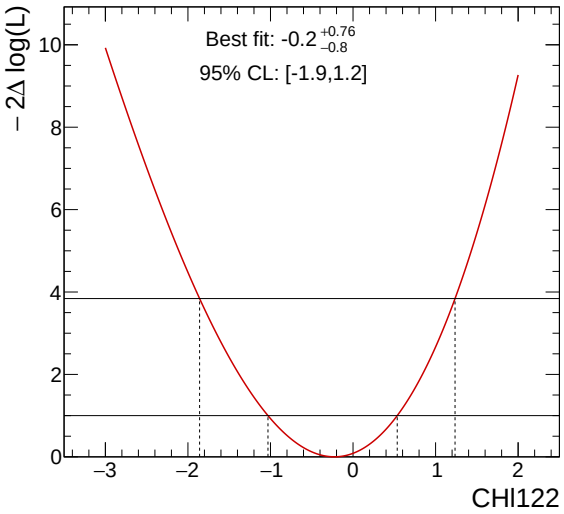

(A.1.3) PLT of C_{Hl122} using $|\cos\theta_V|$ distribution

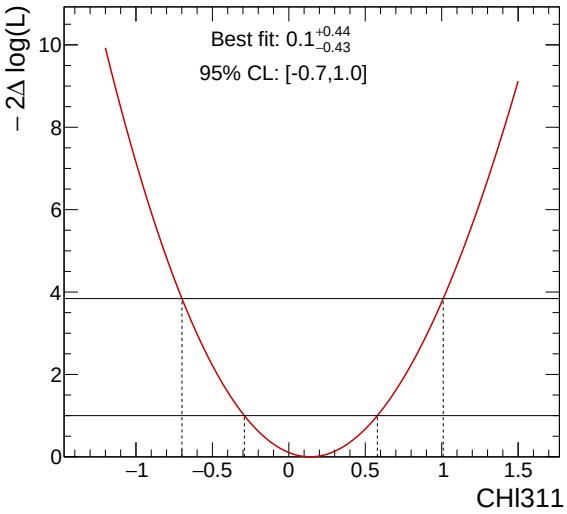

(A.1.4) PLT of C_{Hl311} using $|\cos\theta_V|$ distribution

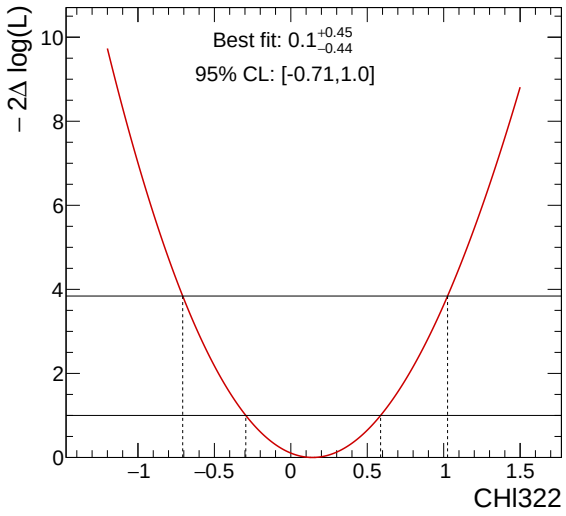

(A.1.5) PLT of C_{Hl322} using $|\cos\theta_V|$ distribution

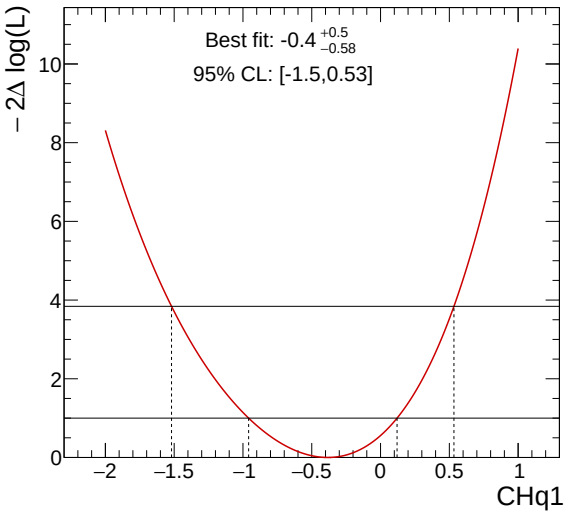

(A.1.6) PLT of C_{Hq1} using $|\cos\theta_V|$ distribution

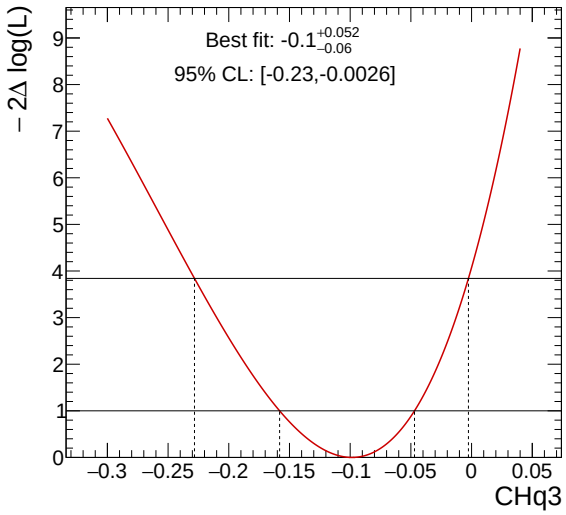

(A.1.7) PLT of C_{Hq3} using $|\cos\theta_V|$ distribution

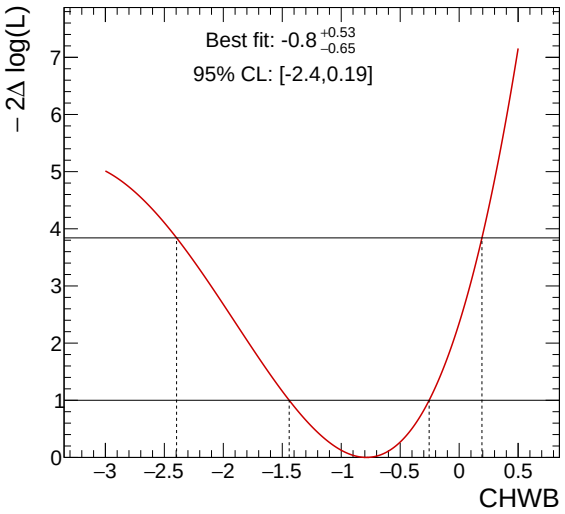

(A.1.8) PLT of C_{HWB} using $|\cos\theta_V|$ distribution

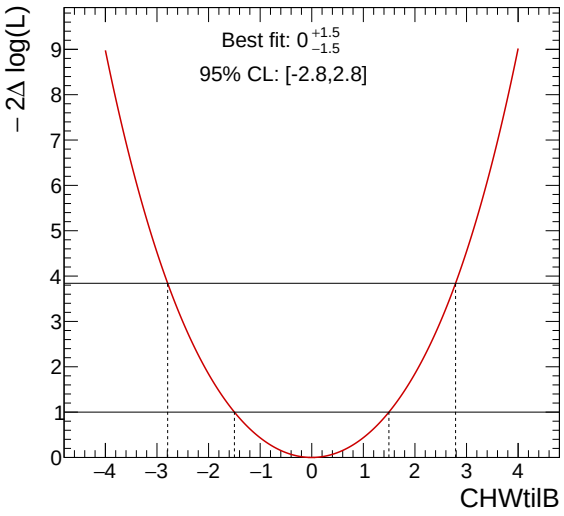

(A.1.9) PLT of $C_{H\tilde{W}B}$ using $|\cos\theta_V|$ distribution

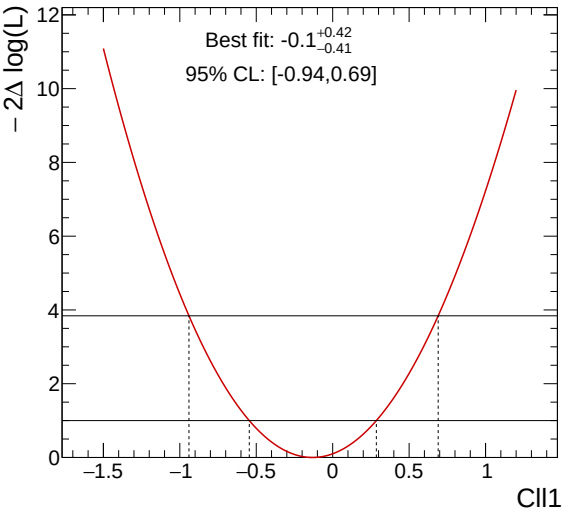

(A.1.10) PLT of C_{ll1221} using $|\cos\theta_V|$ distribution

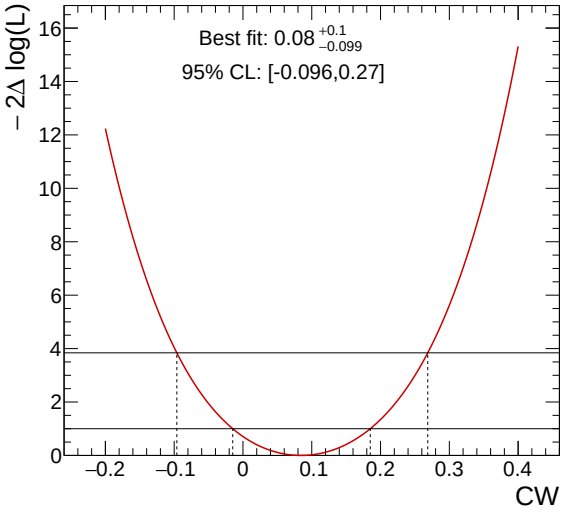

(A.1.11) PLT of C_W using $|\cos\theta_V|$ distribution

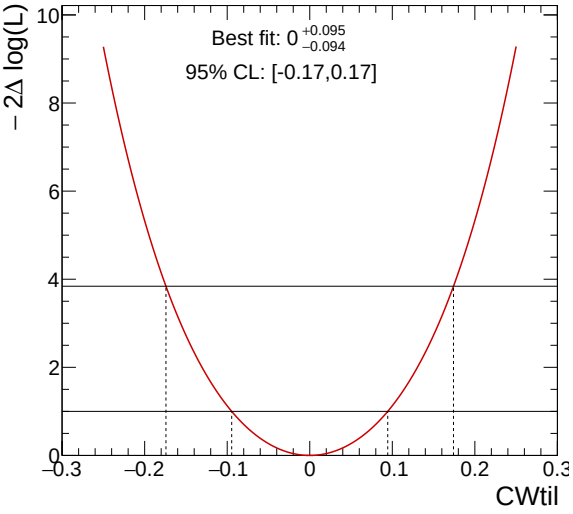

(A.1.12) PLT of $C_{\tilde{W}}$ using $|\cos\theta_V|$ distribution

A.2 $\cos\theta^*_{\ell Z}$

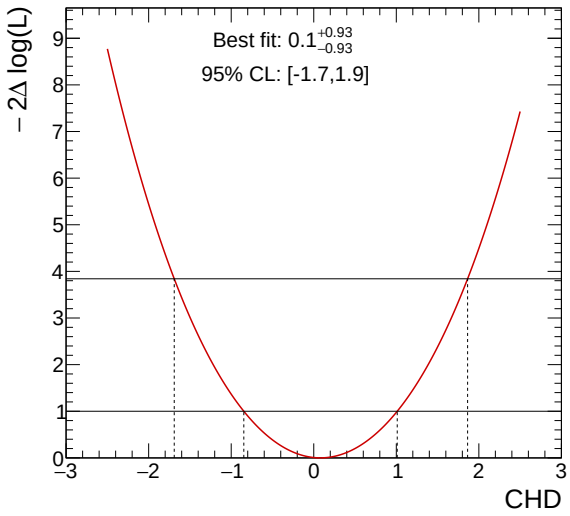

(A.2.1) PLT of C_{HD} using $\cos\theta^*_{\ell Z}$ distribution

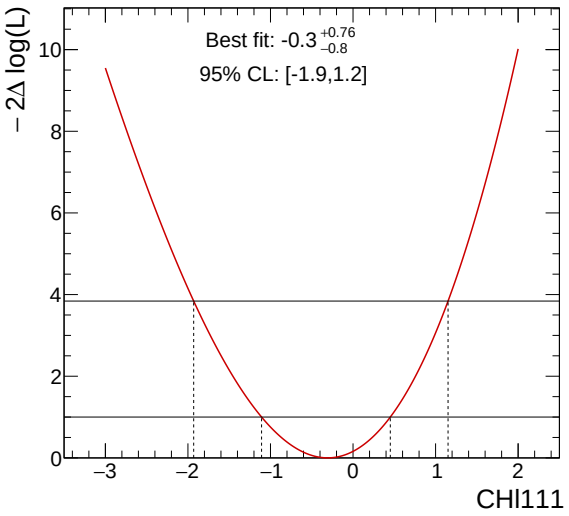

(A.2.2) PLT of C_{Hl111} using $\cos\theta^*_{\ell Z}$ distribution

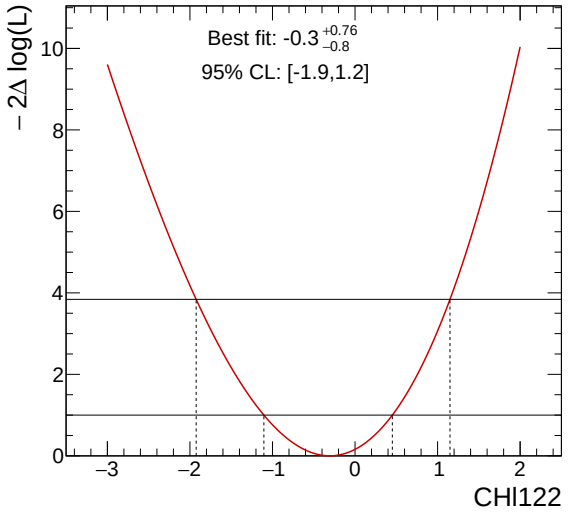

(A.2.3) PLT of C_{Hl122} using $\cos\theta^*_{\ell Z}$ distribution

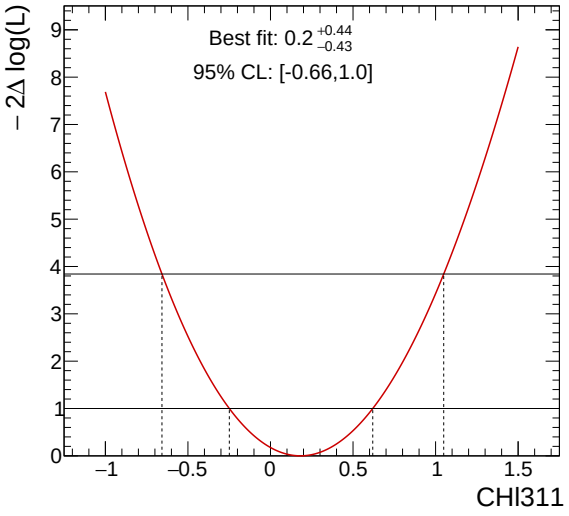

(A.2.4) PLT of C_{Hl311} using $\cos\theta^*_{\ell Z}$ distribution

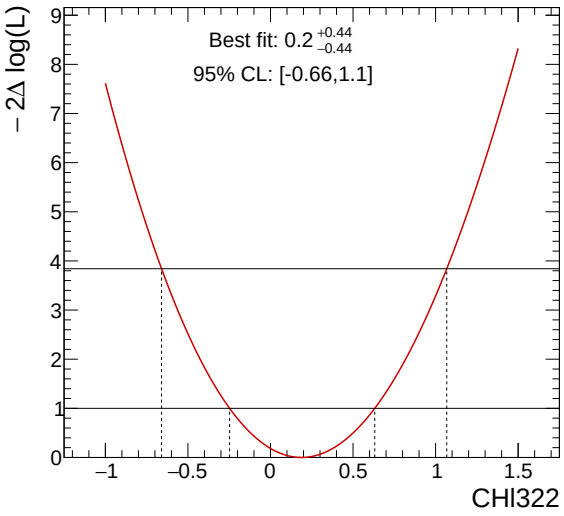

(A.2.5) PLT of C_{Hl322} using $\cos\theta^*_{\ell Z}$ distribution

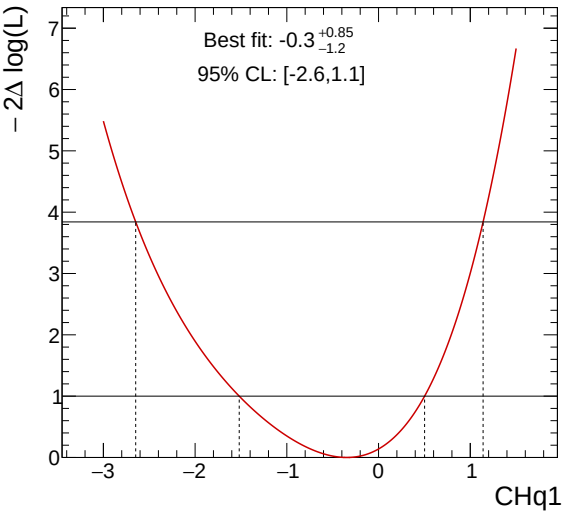

(A.2.6) PLT of C_{Hq1} using $\cos\theta^*_{\ell Z}$ distribution

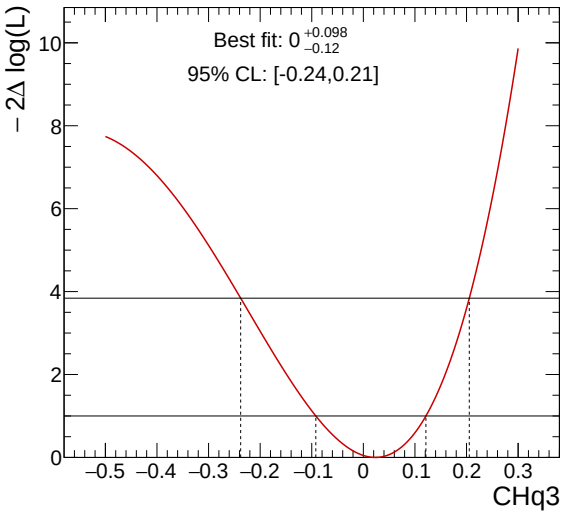

(A.2.7) PLT of C_{Hq3} using $\cos\theta^*_{\ell Z}$ distribution

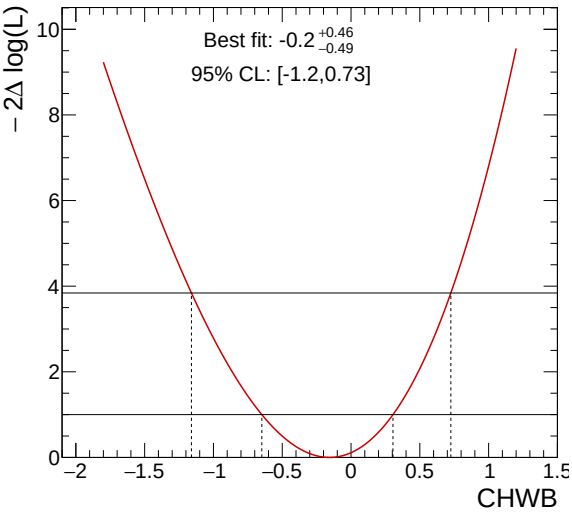

(A.2.8) PLT of C_{HWB} using $\cos\theta^*_{\ell Z}$ distribution

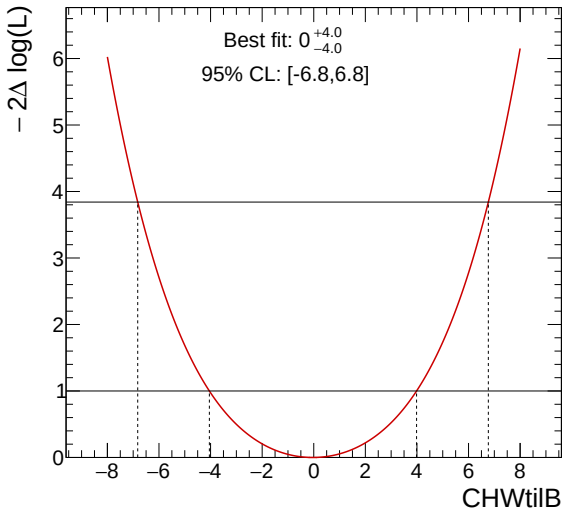

(A.2.9) PLT of $C_{H\tilde{W}B}$ using $\cos\theta^*_{\ell Z}$ distribution

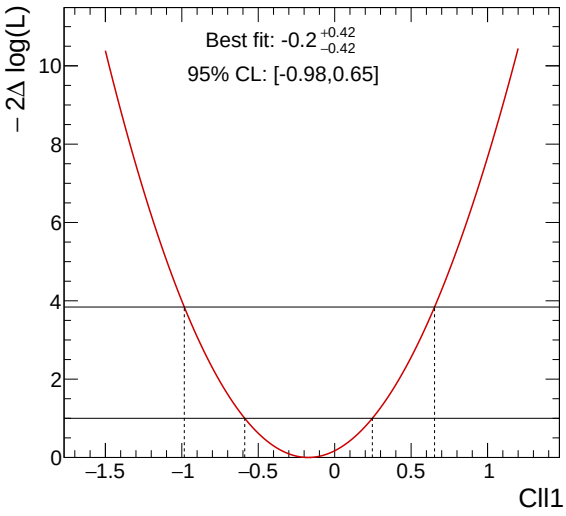

(A.2.10) PLT of C_{ll1221} using $\cos\theta^*_{\ell Z}$ distribution

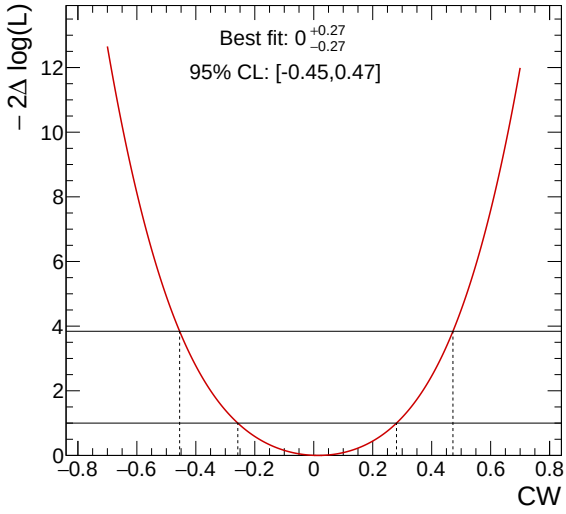

(A.2.11) PLT of C_W using $\cos\theta^*_{\ell Z}$ distribution

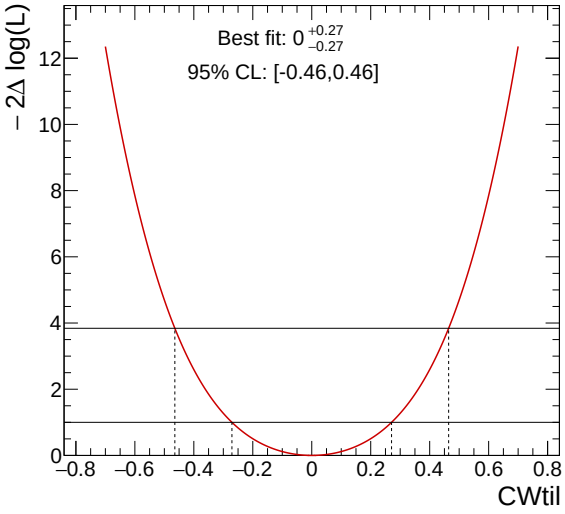

(A.2.12) PLT of $C_{\tilde{W}}$ using $\cos\theta^*_{\ell Z}$ distribution

A.3 $q_W \cdot \cos\theta^*_{\ell W}$

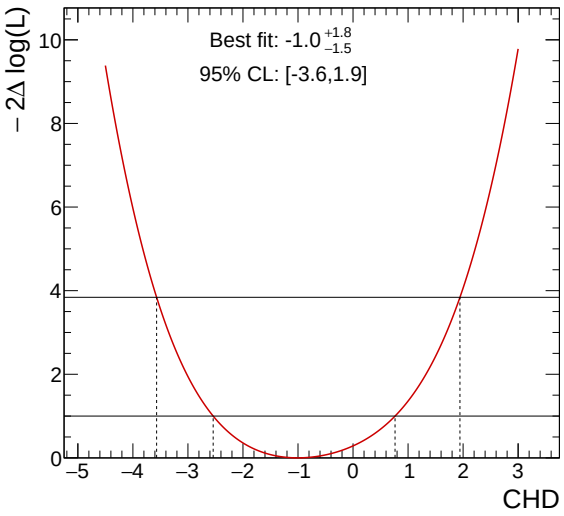

(A.3.1) PLT of C_{HD} using $q_W \cdot \cos\theta^*_{\ell W}$ distribution

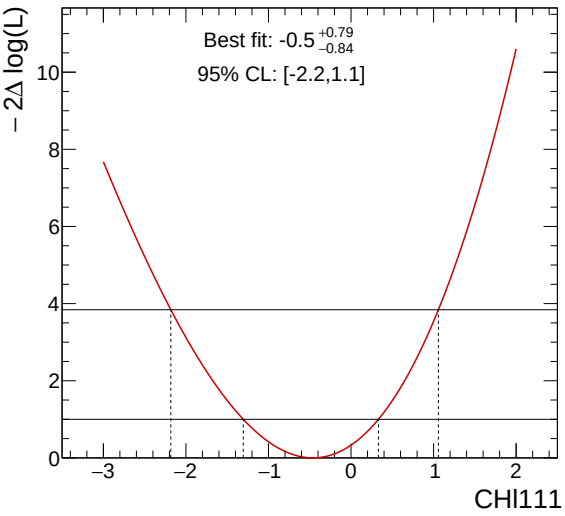

(A.3.2) PLT of C_{Hl111} using $q_W \cdot \cos\theta^*_{\ell W}$ distribution

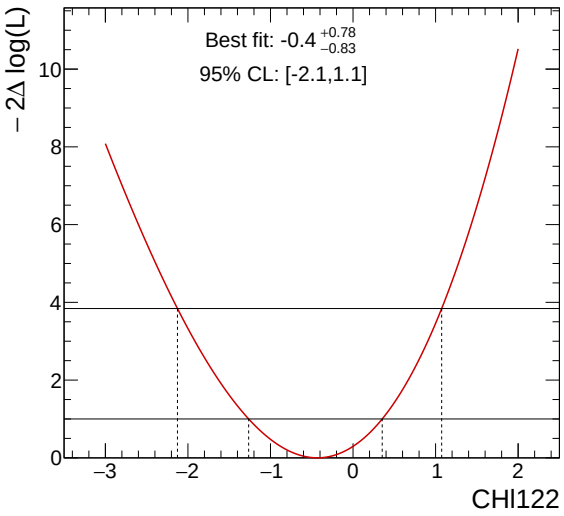

(A.3.3) PLT of C_{Hl122} using $q_W \cdot \cos\theta^*_{\ell W}$ distribution

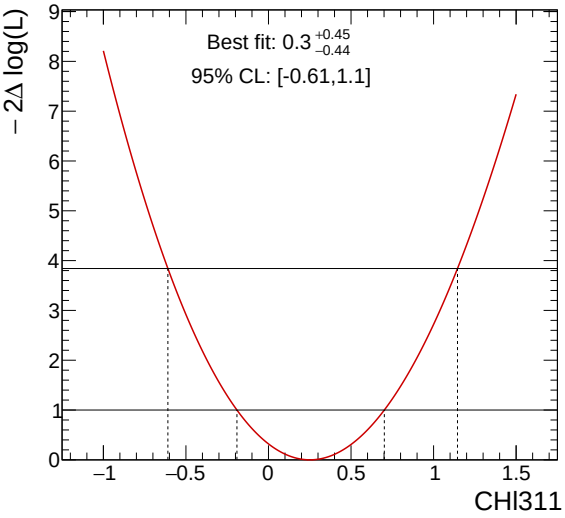

(A.3.4) PLT of C_{Hl311} using $q_W \cdot \cos\theta^*_{\ell W}$ distribution

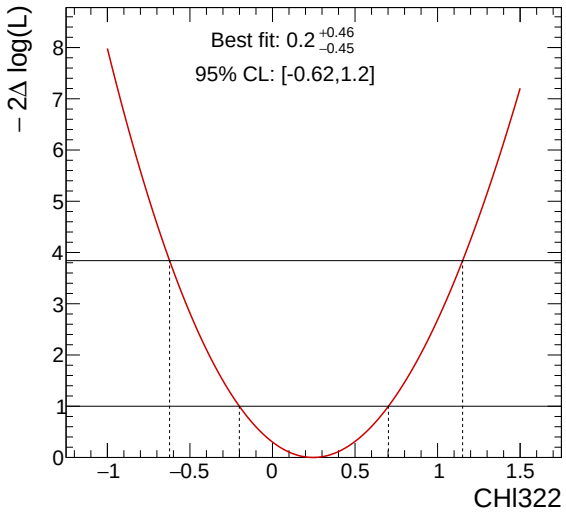

(A.3.5) PLT of C_{Hl322} using $q_W \cdot \cos\theta^*_{\ell W}$ distribution

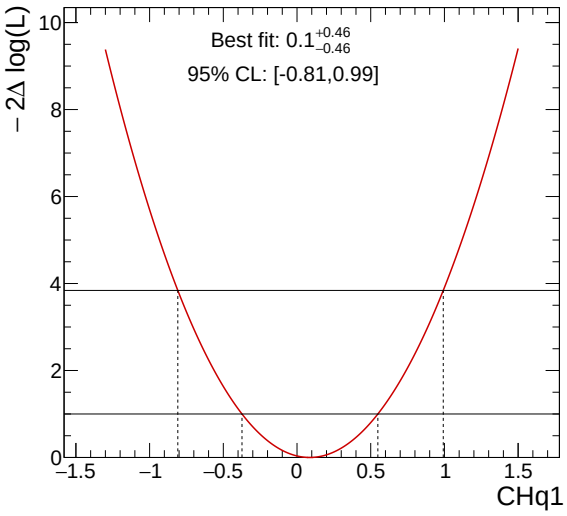

(A.3.6) PLT of C_{Hq1} using $q_W \cdot \cos\theta^*_{\ell W}$ distribution

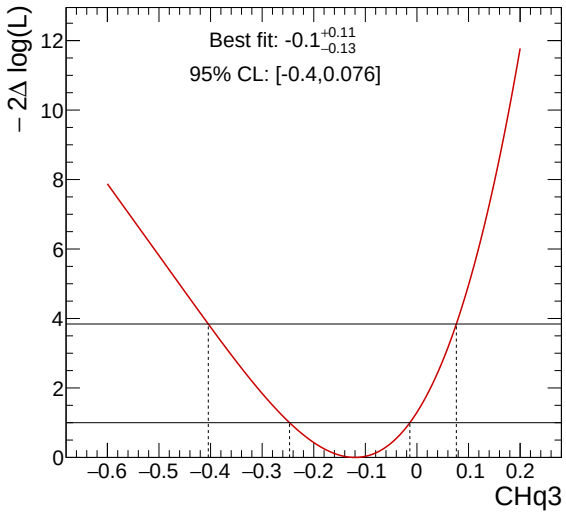

(A.3.7) PLT of C_{Hq3} using $q_W \cdot \cos\theta^*_{\ell W}$ distribution

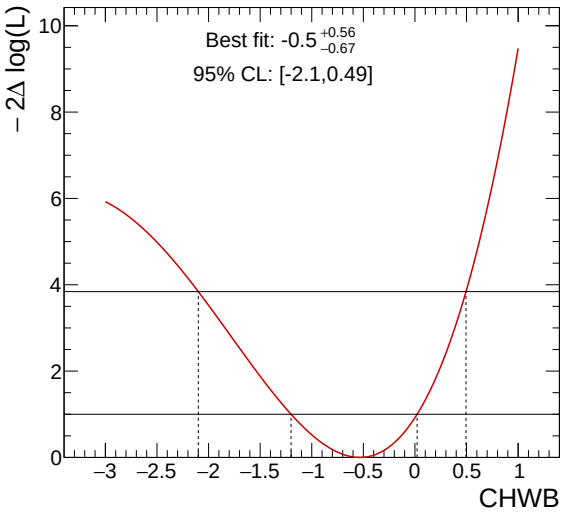

(A.3.8) PLT of C_{HWB} using $q_W \cdot \cos\theta^*_{\ell W}$ distribution

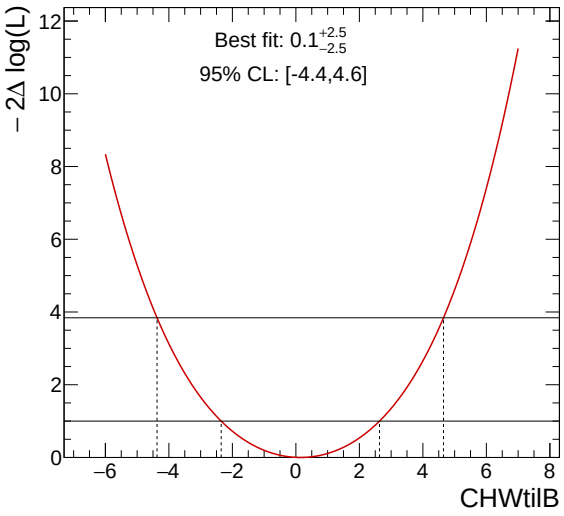

(A.3.9) PLT of $C_{H\tilde{W}B}$ using $q_W \cdot \cos\theta^*_{\ell W}$ distribution

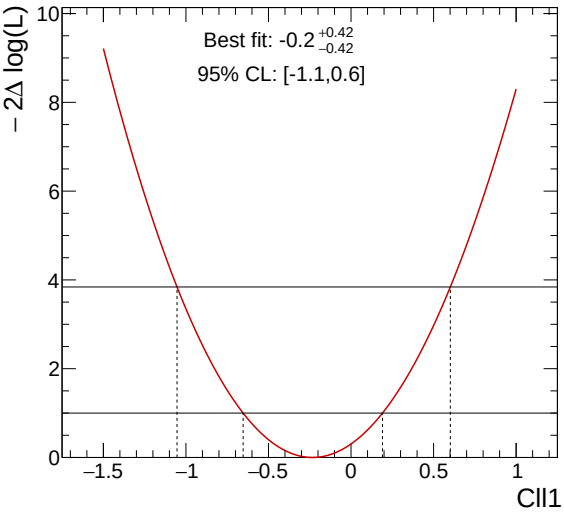

(A.3.10) PLT of C_{ll1221} using $q_W \cdot \cos\theta^*_{\ell W}$ distribution

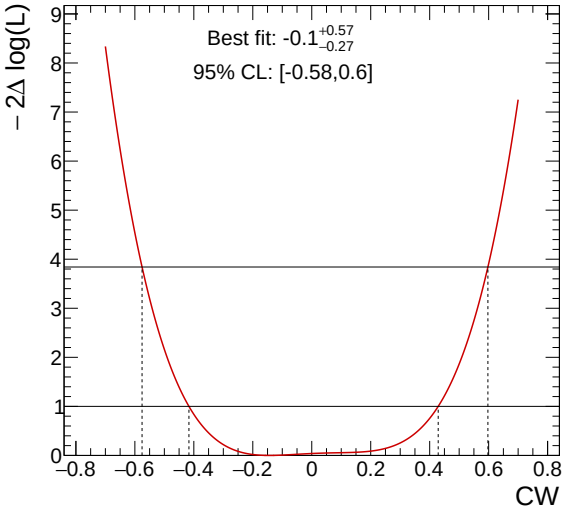

(A.3.11) PLT of C_W using $q_W \cdot \cos\theta^*_{\ell W}$ distribution

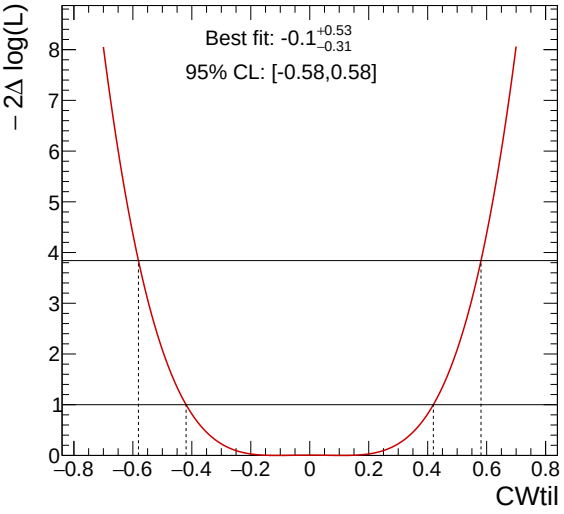

(A.3.12) PLT of $C_{\tilde{W}}$ using $q_W \cdot \cos\theta^*_{\ell W}$ distribution

A.4 m_T^{WZ}

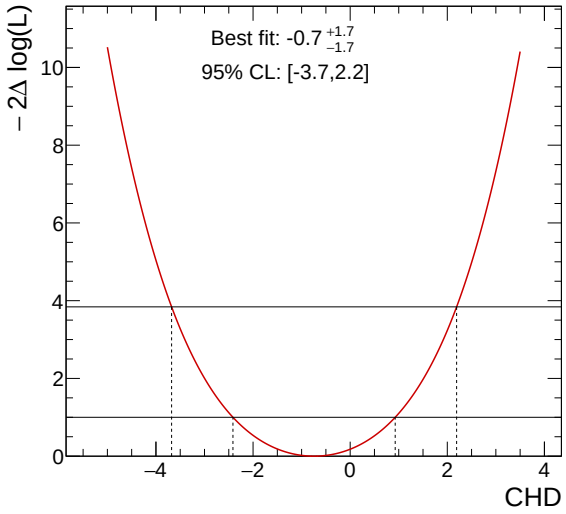

(A.4.1) PLT of C_{HD} using m_T^{WZ} distribution

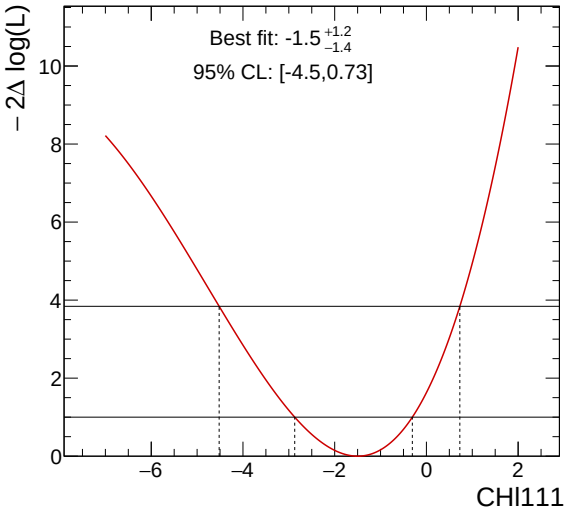

(A.4.2) PLT of C_{Hl111} using m_T^{WZ} distribution

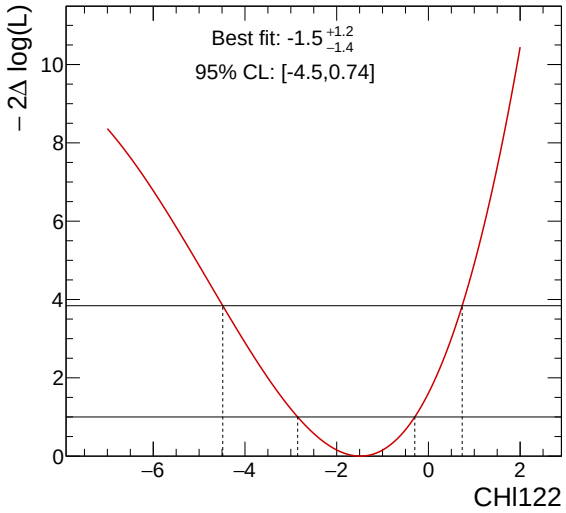

(A.4.3) PLT of C_{Hl122} using m_T^{WZ} distribution

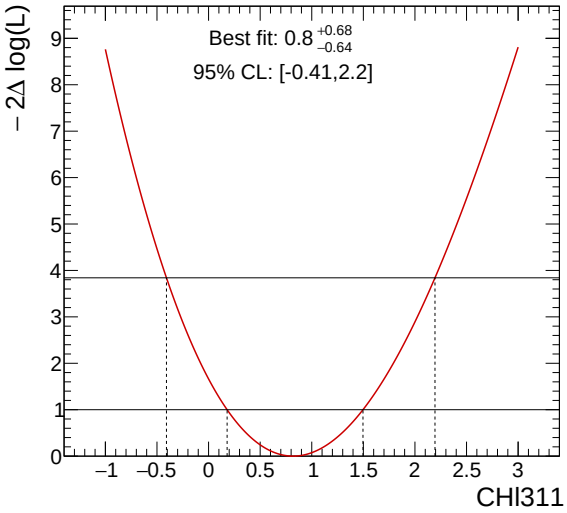

(A.4.4) PLT of C_{Hl311} using m_T^{WZ} distribution

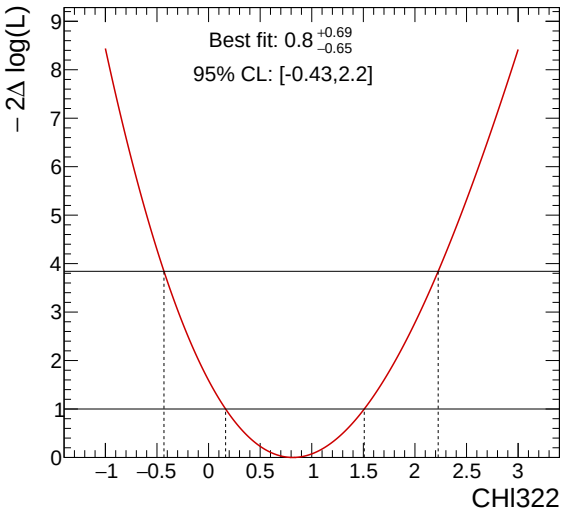

(A.4.5) PLT of C_{Hl322} using m_T^{WZ} distribution

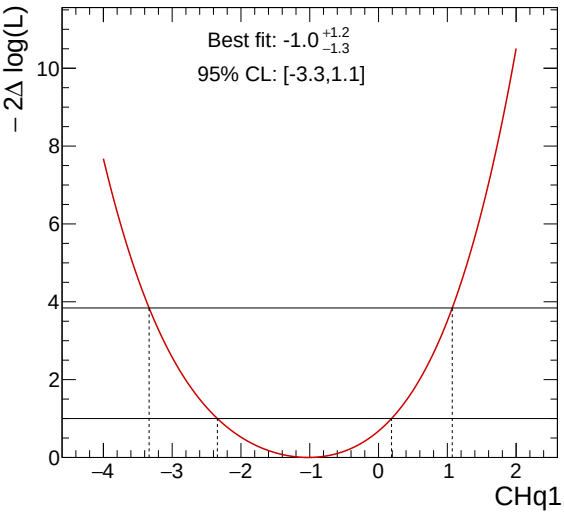

(A.4.6) PLT of C_{Hq1} using m_T^{WZ} distribution

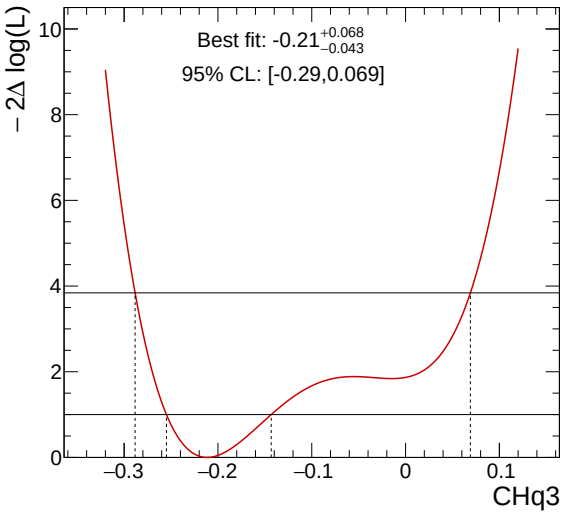

(A.4.7) PLT of C_{Hq3} using m_T^{WZ} distribution

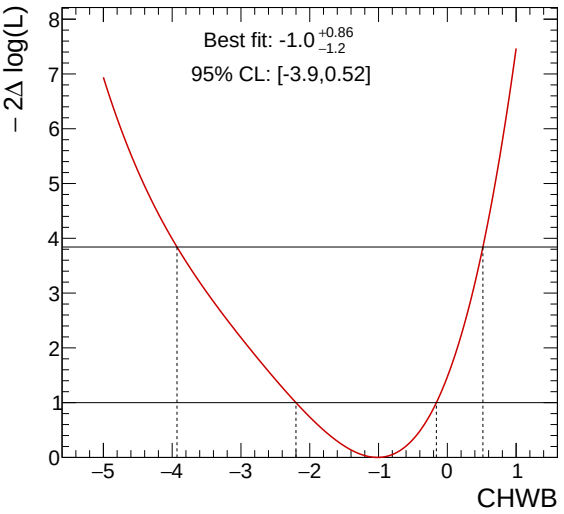

(A.4.8) PLT of C_{HWB} using m_T^{WZ} distribution

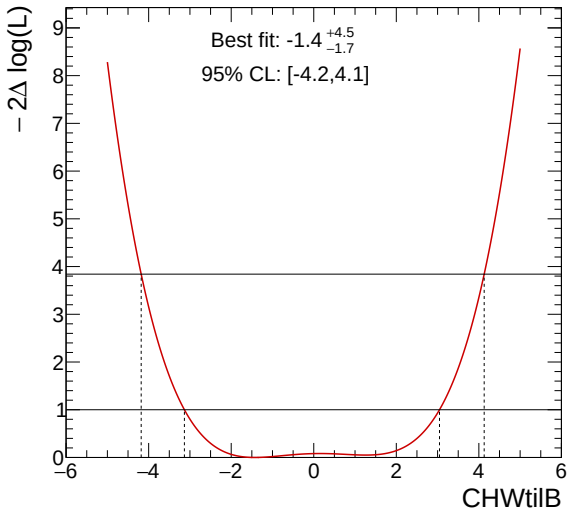

(A.4.9) PLT of $C_{H\tilde{W}B}$ using m_T^{WZ} distribution

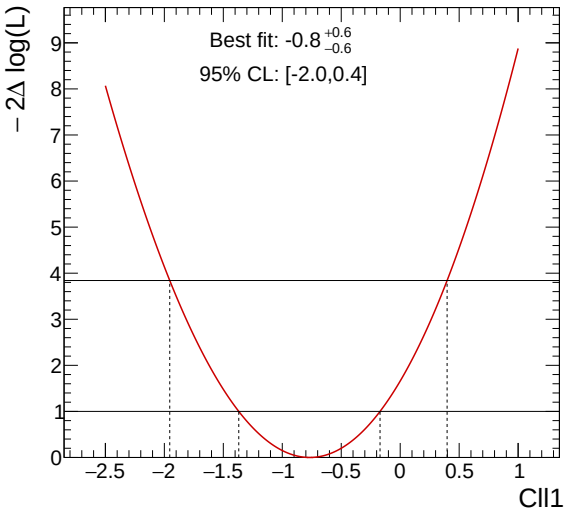

(A.4.10) PLT of C_{ll1221} using m_T^{WZ} distribution

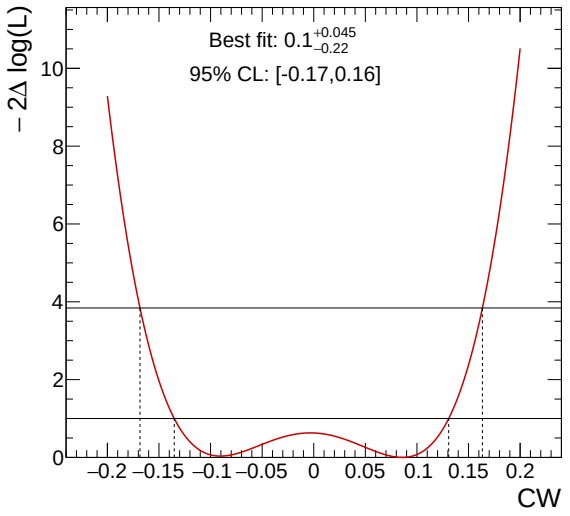

(A.4.11) PLT of C_W using m_T^{WZ} distribution

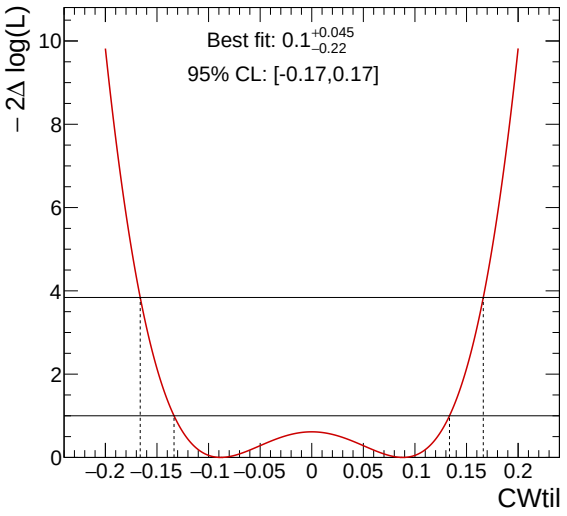

(A.4.12) PLT of $C_{\tilde{W}}$ using m_T^{WZ} distribution

B HEPDATA vs 95% CL

B.1 $|\cos\theta_V|$

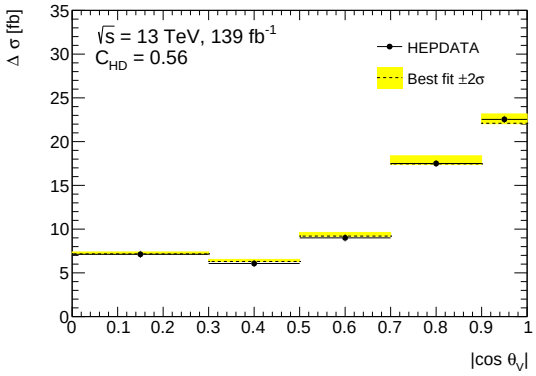

(B.1.1) $|\cos\theta_V|$, HEPDATA vs C_{HD} 95% CL

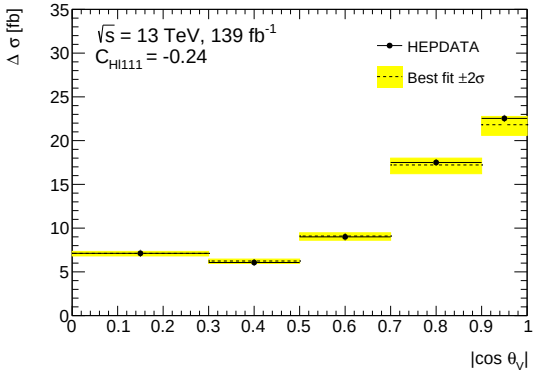

(B.1.2) $|\cos\theta_V|$, HEPDATA vs C_{Hl111} 95% CL

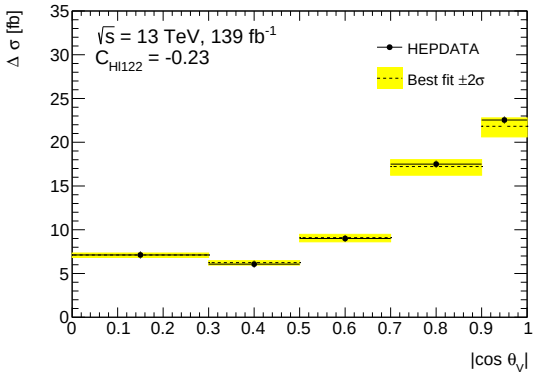

(B.1.3) $|\cos\theta_V|$, HEPDATA vs C_{Hl122} 95% CL

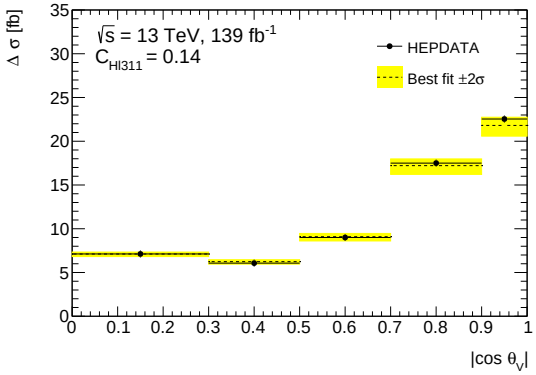

(B.1.4) $|\cos\theta_V|$, HEPDATA vs C_{Hl311} 95% CL

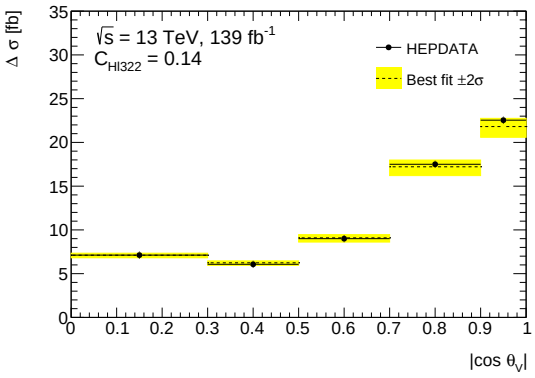

(B.1.5) $|\cos\theta_V|$, HEPDATA vs C_{Hl322} 95% CL

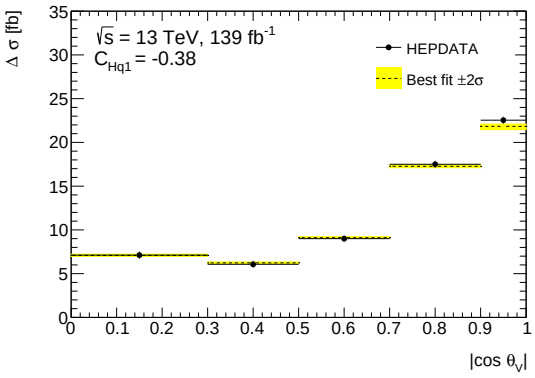

(B.1.6) $|\cos\theta_V|$, HEPDATA vs C_{Hq1} 95% CL

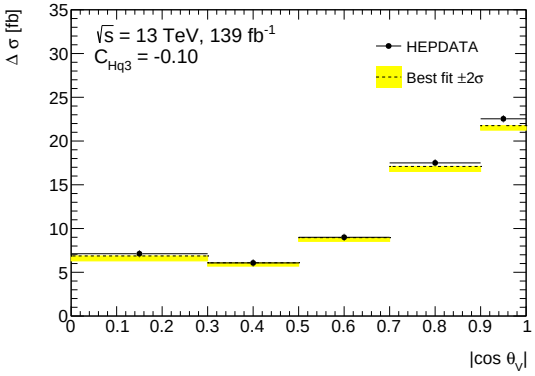

(B.1.7) $|\cos\theta_V|$, HEPDATA vs C_{Hq3} 95% CL

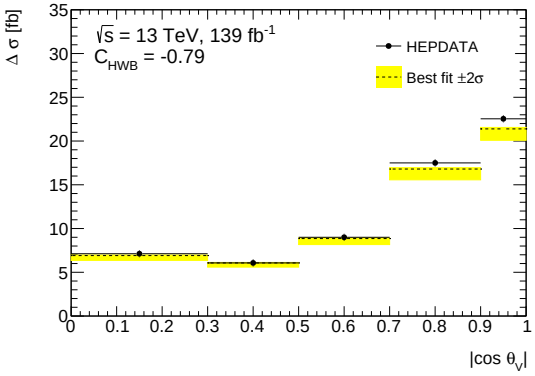

(B.1.8) $|\cos\theta_V|$, HEPDATA vs C_{HWB} 95% CL

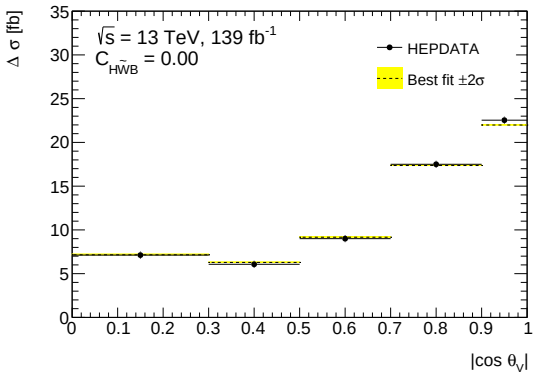

(B.1.9) $|\cos\theta_V|$, HEPDATA vs $C_{H\tilde{W}B}$ 95% CL

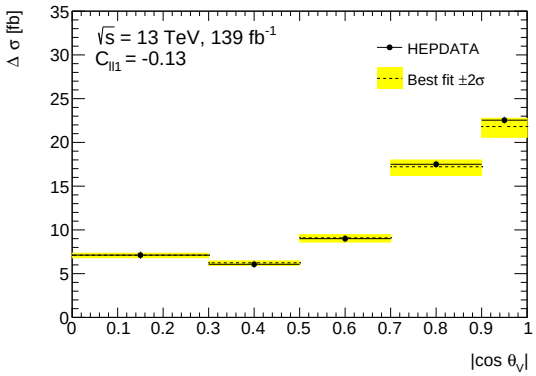

(B.1.10) $|\cos\theta_V|$, HEPDATA vs C_{ll1221} 95% CL

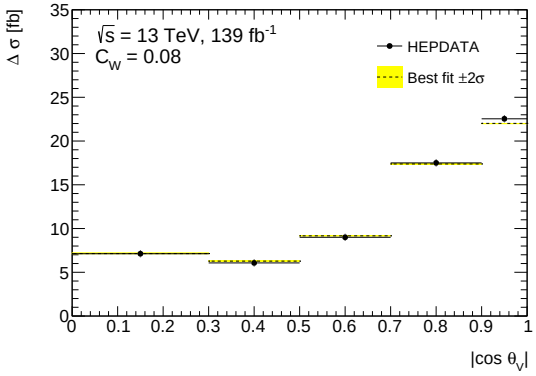

(B.1.11) $|\cos\theta_V|$, HEPDATA vs C_W 95% CL

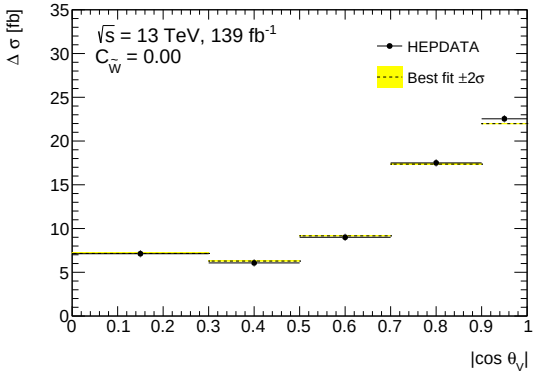

(B.1.12) $|\cos\theta_V|$, HEPDATA vs $C_{\tilde{W}}$ 95% CL

B.2 $\cos\theta^*_{\ell Z}$

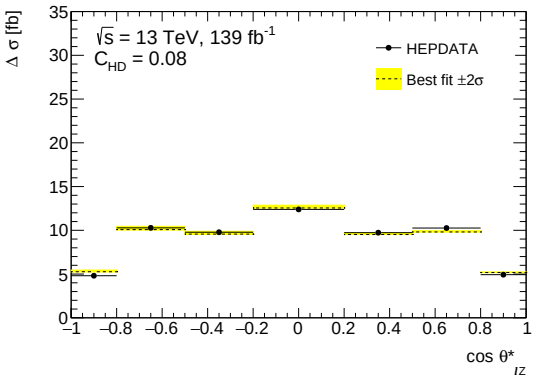

(B.2.1) $\cos\theta^*_{\ell Z}$, HEPDATA vs C_{HD} 95% CL

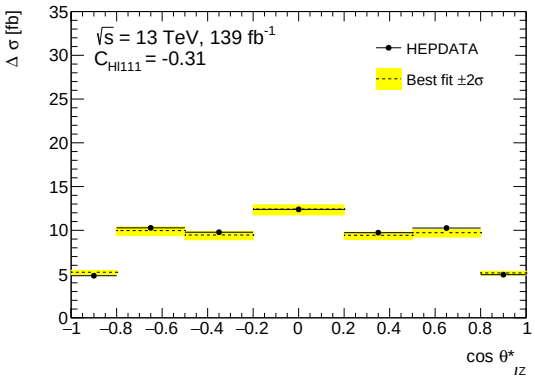

(B.2.2) $\cos\theta^*_{\ell Z}$, HEPDATA vs C_{Hl111} 95% CL

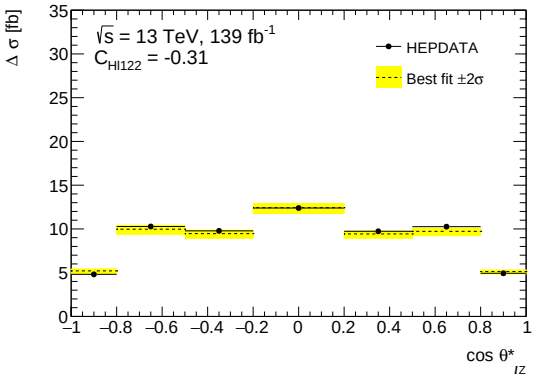

(B.2.3) $\cos\theta^*_{\ell Z}$, HEPDATA vs C_{Hl122} 95% CL

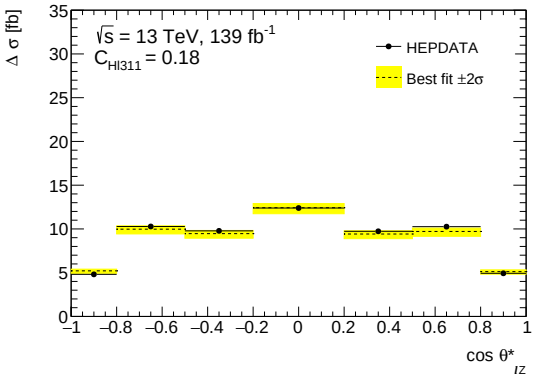

(B.2.4) $\cos\theta^*_{\ell Z}$, HEPDATA vs C_{Hl311} 95% CL

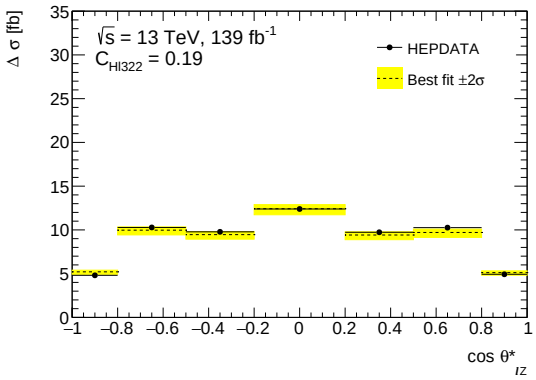

(B.2.5) $\cos\theta^*_{\ell Z}$, HEPDATA vs C_{Hl322} 95% CL

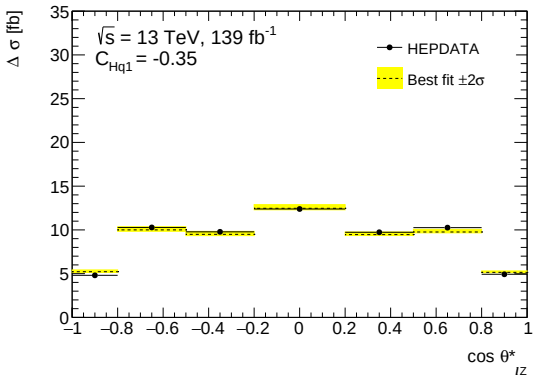

(B.2.6) $\cos\theta^*_{\ell Z}$, HEPDATA vs C_{Hq1} 95% CL

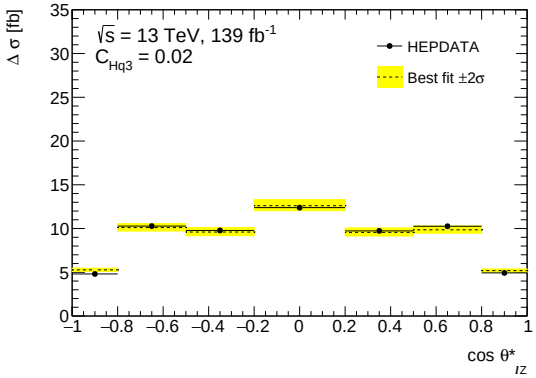

(B.2.7) $\cos\theta^*_{\ell Z}$, HEPDATA vs C_{Hq3} 95% CL

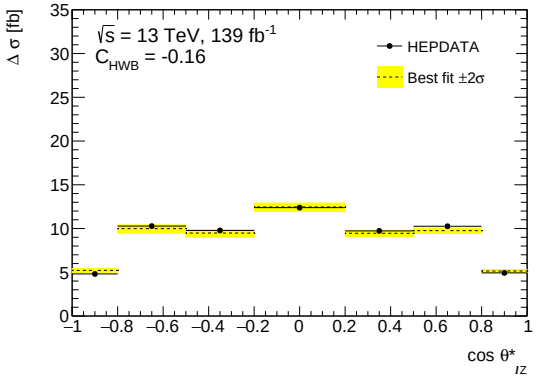

(B.2.8) $\cos\theta^*_{\ell Z}$, HEPDATA vs C_{HWB} 95% CL

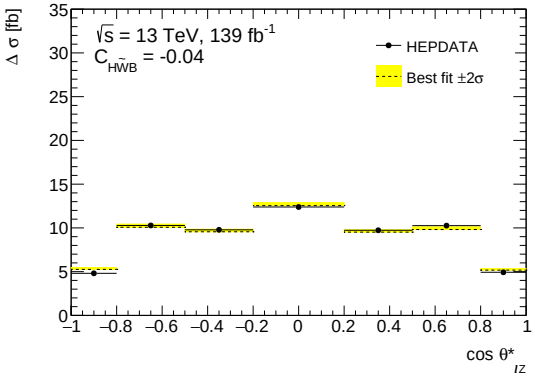

(B.2.9) $\cos\theta^*_{\ell Z}$, HEPDATA vs $C_{H\tilde{W}B}$ 95% CL

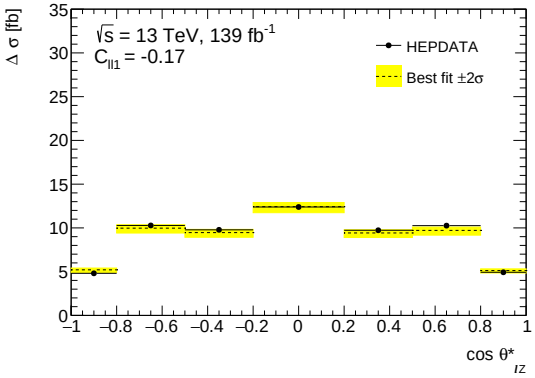

(B.2.10) $\cos\theta^*_{\ell Z}$, HEPDATA vs C_{ll1221} 95% CL

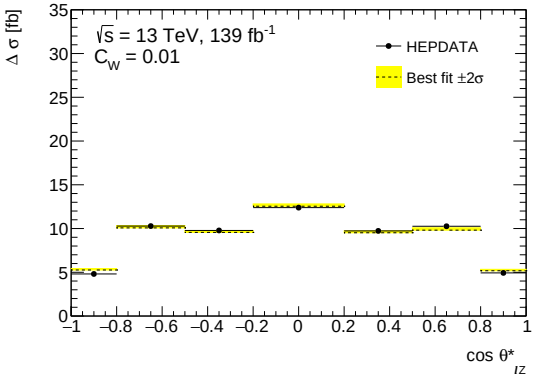

(B.2.11) $\cos\theta^*_{\ell Z}$, HEPDATA vs C_W 95% CL

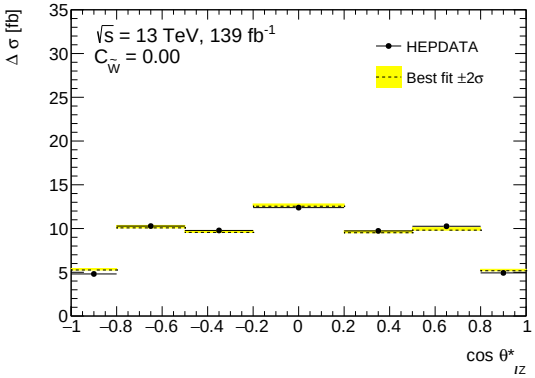

(B.2.12) $\cos\theta^*_{\ell Z}$, HEPDATA vs $C_{\tilde{W}}$ 95% CL

B.3 $q_W \cdot \cos\theta^*_{\ell W}$

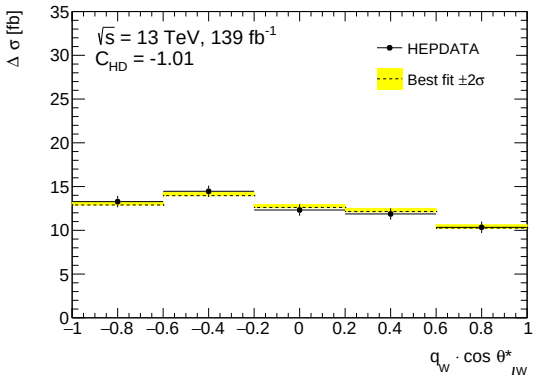

(B.3.1) $q_W \cdot \cos\theta^*_{\ell W}$, HEPDATA vs C_{HD} 95% CL

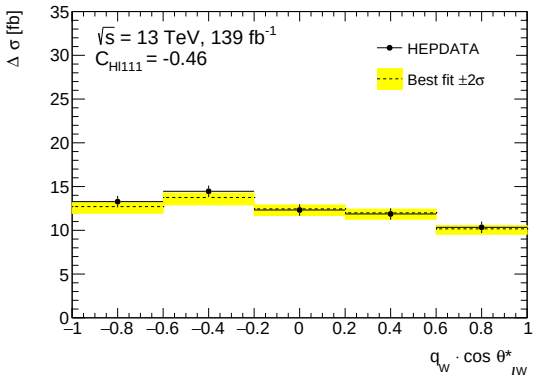

(B.3.2) $q_W \cdot \cos\theta^*_{\ell W}$, HEPDATA vs C_{Hl111} 95% CL

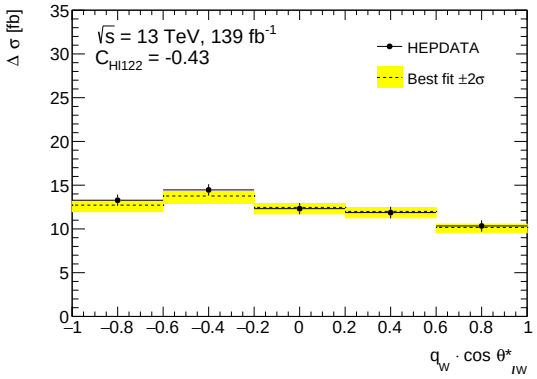

(B.3.3) $q_W \cdot \cos\theta^*_{\ell W}$, HEPDATA vs C_{Hl122} 95% CL

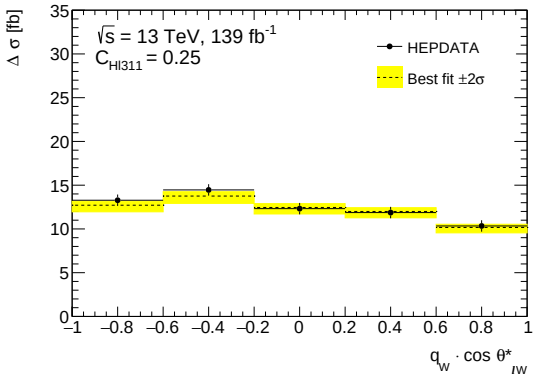

(B.3.4) $q_W \cdot \cos\theta^*_{\ell W}$, HEPDATA vs C_{Hl311} 95% CL

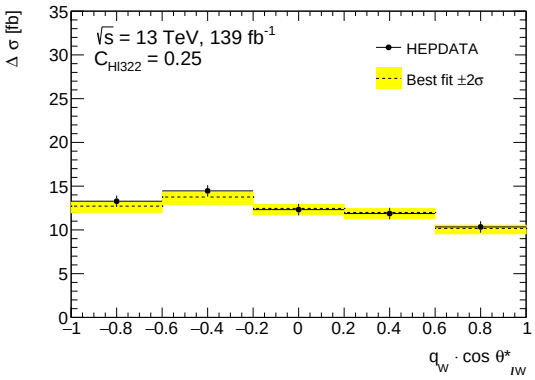

(B.3.5) $q_W \cdot \cos\theta^*_{\ell W}$, HEPDATA vs C_{Hl322} 95% CL

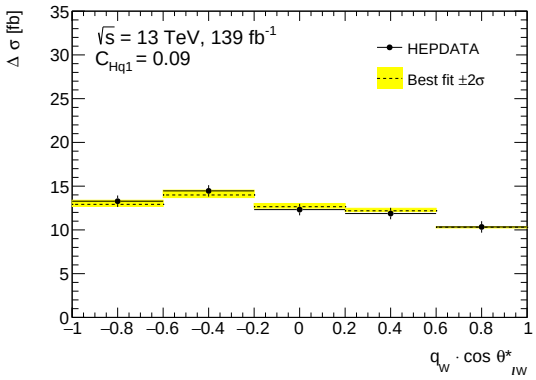

(B.3.6) $q_W \cdot \cos\theta^*_{\ell W}$, HEPDATA vs C_{Hq1} 95% CL

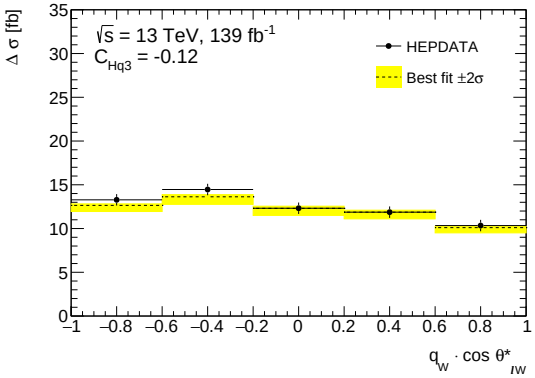

(B.3.7) $q_W \cdot \cos\theta^*_{\ell W}$, HEPDATA vs C_{Hq3} 95% CL

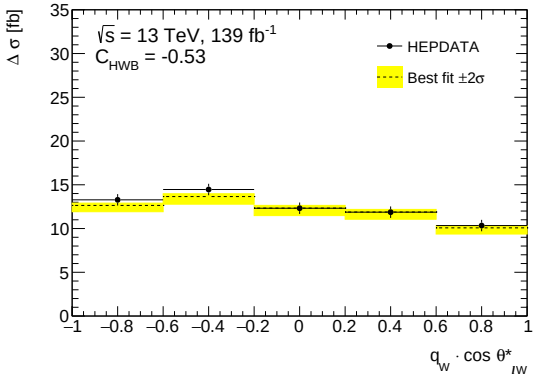

(B.3.8) $q_W \cdot \cos\theta^*_{\ell W}$, HEPDATA vs C_{HWB} 95% CL

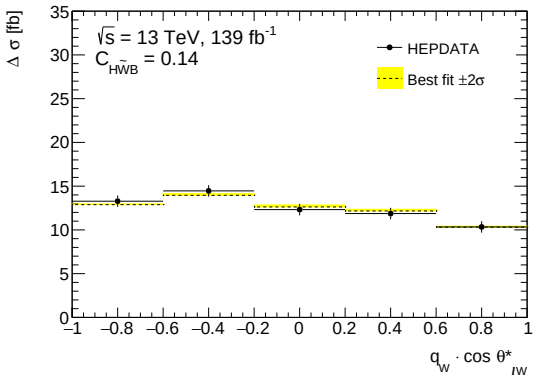

(B.3.9) $q_W \cdot \cos\theta^*_{\ell W}$, HEPDATA vs $C_{H\tilde{W}B}$ 95% CL

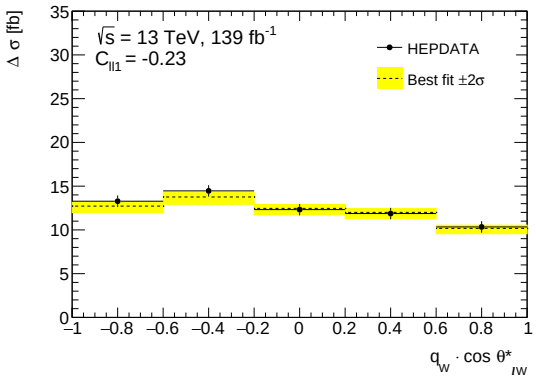

(B.3.10) $q_W \cdot \cos\theta^*_{\ell W}$, HEPDATA vs C_{ll1221} 95% CL

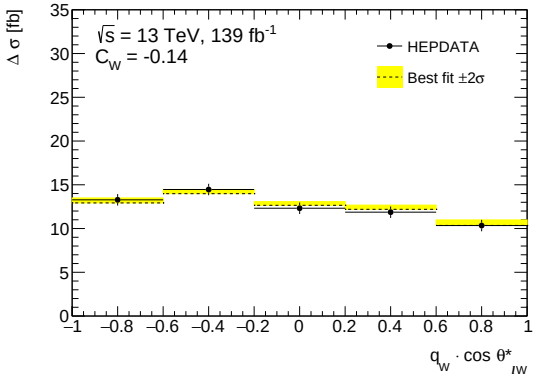

(B.3.11) $q_W \cdot \cos\theta^*_{\ell W}$, HEPDATA vs C_W 95% CL

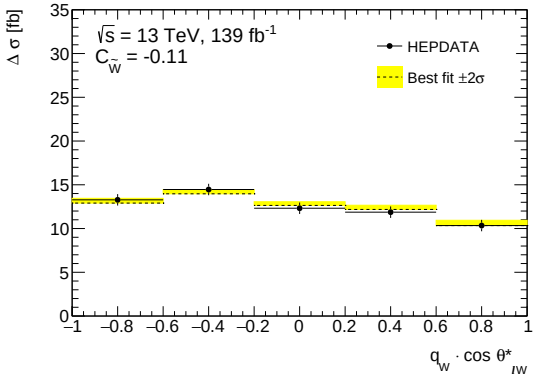

(B.3.12) $q_W \cdot \cos\theta^*_{\ell W}$, HEPDATA vs $C_{\tilde{W}}$ 95% CL

B.4 m_T^{WZ}

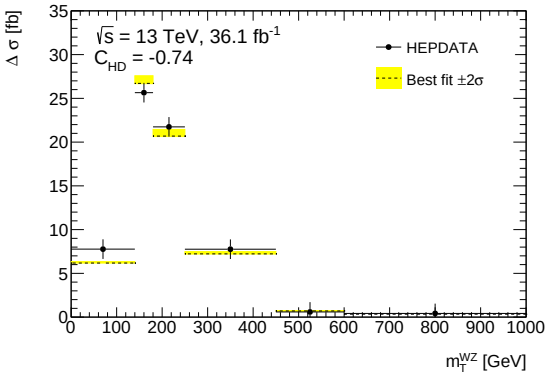

(B.4.1) m_T^{WZ}, HEPDATA vs C_{HD} 95% CL

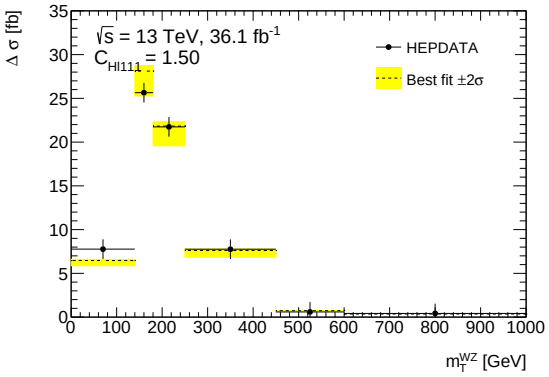

(B.4.2) m_T^{WZ}, HEPDATA vs C_{Hl111} 95% CL

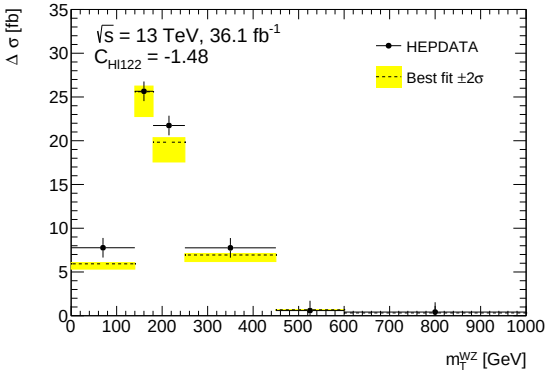

(B.4.3) m_T^{WZ}, HEPDATA vs C_{Hl122} 95% CL

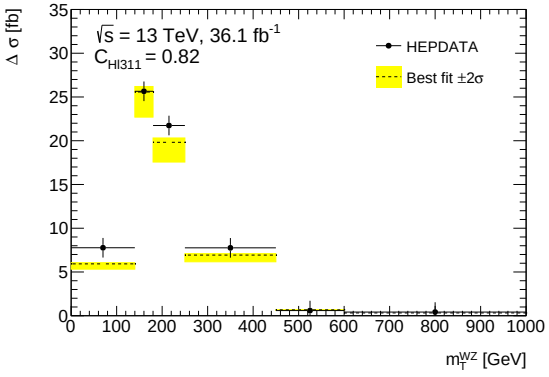

(B.4.4) m_T^{WZ}, HEPDATA vs C_{Hl311} 95% CL

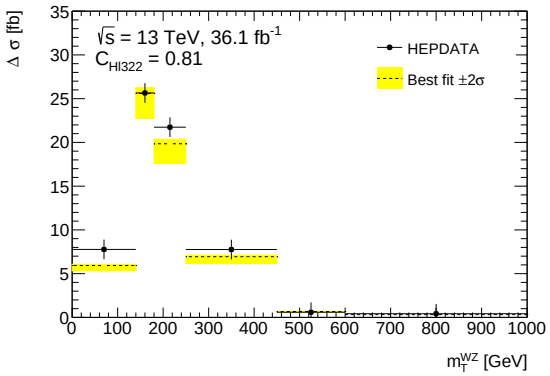

(B.4.5) m_T^{WZ}, HEPDATA vs C_{Hl322} 95% CL

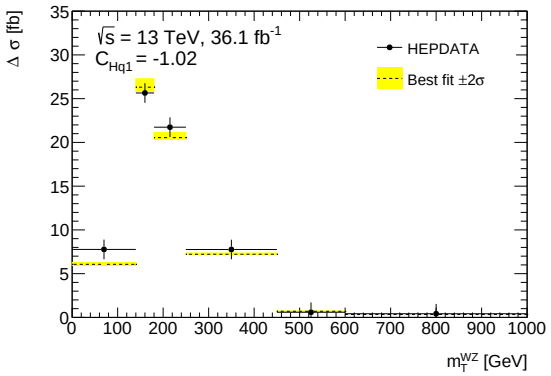

(B.4.6) m_T^{WZ}, HEPDATA vs C_{Hq1} 95% CL

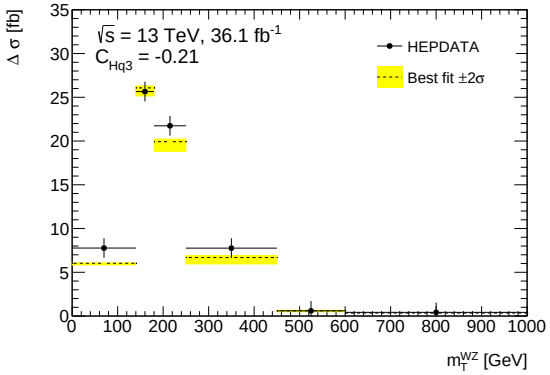

(B.4.7) m_T^{WZ}, HEPDATA vs C_{Hq3} 95% CL

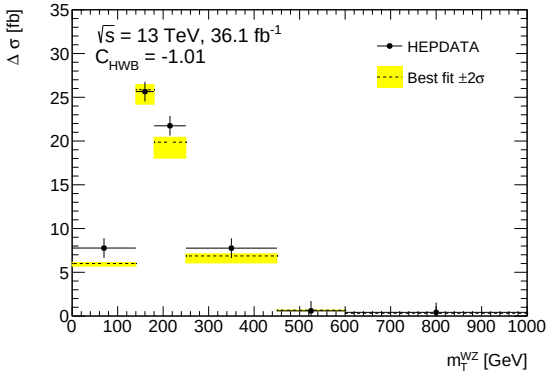

(B.4.8) m_T^{WZ}, HEPDATA vs C_{HWB} 95% CL

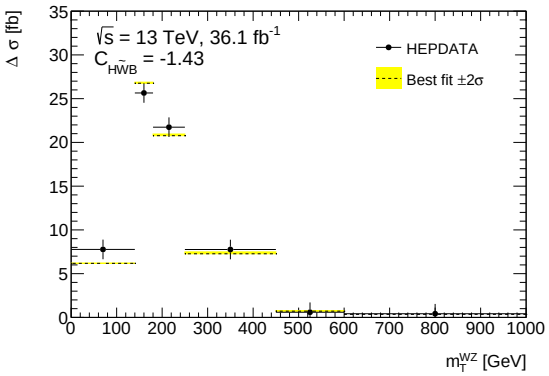

(B.4.9) m_T^{WZ}, HEPDATA vs $C_{H\tilde{W}B}$ 95% CL

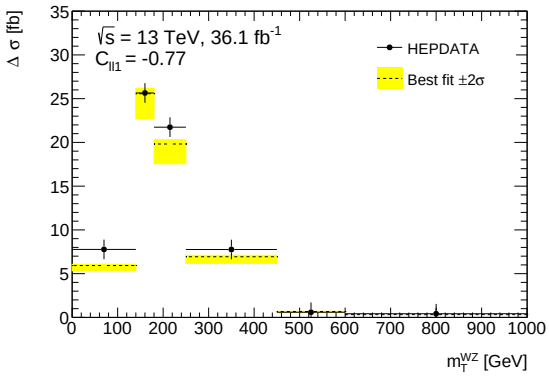

(B.4.10) m_T^{WZ}, HEPDATA vs C_{ll1221} 95% CL

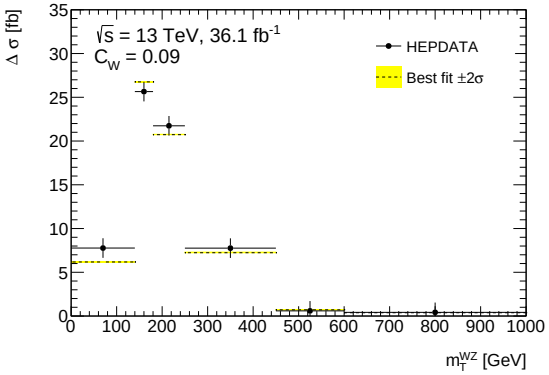

(B.4.11) m_T^{WZ}, HEPDATA vs C_W 95% CL

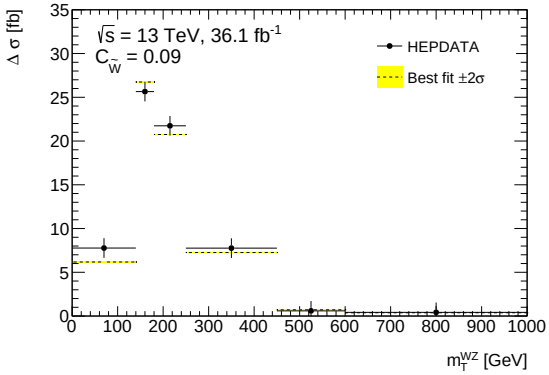

(B.4.12) m_T^{WZ}, HEPDATA vs $C_{\tilde{W}}$ 95% CL

C New Small Wheel commissioning

For two years (2020-2021) I worked on the New Small Wheel upgrade to the ATLAS experiment. This Appendix will detail what this upgrade is, its goals, and what work I did.

From 2026 to about 2029, the LHC is planned to have its third Long Shutdown, during which the systems will be upgraded to deliver a much higher luminosity by the time it restarts in 2030, an increase by a factor of 10, in what is called the High Luminosity-LHC (HL-LHC). This increase in luminosity demands that various systems in the detectors of the LHC ring be upgraded to be able to cope with it. Among these is the innermost muon detector in the endcap sections of ATLAS, the "Small Wheels", made out of CSC, MDT and TGC technologies, as detailed in section 3.3.4. These detectors has been replaced with the New Small Wheels, which use small-strip Thin Gap Chambers (sTGCs) for their fast response detection, and Micromegas (MM) for its precision tracking.

The NSW improves over the SW in various aspects, including a better spatial and time resolution, increased radiation protection for longer longevity, and most importantly, a greater precision muon triggering, leading to a drastic reduction of the trigger fake rates. Figure C.1 shows a comparison of the η distributions of the level-1 muon triggers before and after the integration of the NSW, which highlights the fake triggers that were generated in the endcap region. The rate of fake triggers was expected to increase substantially in the higher background environment of the HL-LHC if the SW had not been replaced.

My MSc included work in the construction of the QS1 sTGC modules in Chile (name convention explained below), so as a continuation of that, during my stay at CERN, I helped in the commissioning and integration of the sTGCs of the fully built sectors into the wheels. A fully built sector consists of two MM wedges "sandwiched" between two sTGC wedges, as shown in Figure C.2.

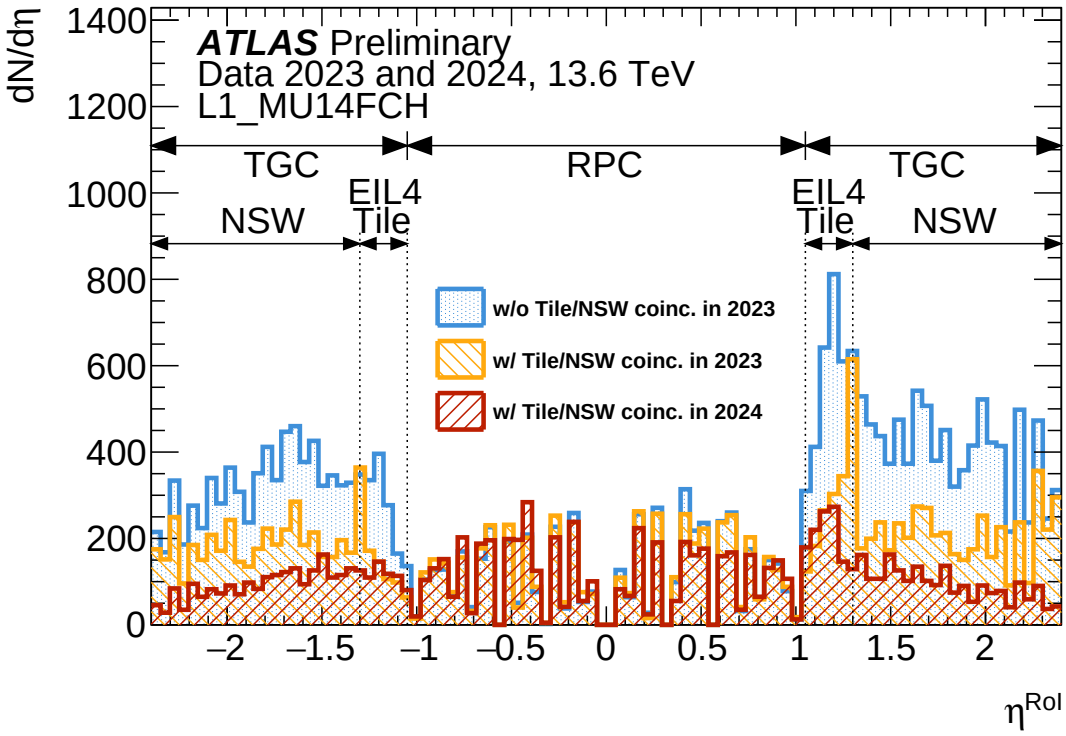

Figure C.1: η distribution of level-1 muon triggers before and after integrating coincidences between Big Wheel TGC and inner muon detectors (NSW and tiles). In 2023 70% of NSW trigger sectors had been integrated, while in 2024 full integration was achieved. [53].

There are two classes of sTGC wedges, the "small" (S) and "large" (L) wedges. Depending on their position in the sandwich, they also get the names "confirm" (C) for the wedges facing out, and "pivot" (P) for the wedges in between the confirm wedges. This means that for small sectors the confirm wedges face the wall of the cavern and the pivot wedges face the ATLAS interaction point, while for large sectors it's the opposite. Each wedge was assembled from 3 sections, numbered from 1 to 3 moving outward radially from the beam line. These sections are all quadruplets (Q), or quads, of sTGC layers, meaning a muon that intersects every layer would go through 8 sTGC layers: 4 on the pivot wedge, and 4 on the confirm wedge. So, for example, Chile was in charge of building the **QS1P** and **QS1C** quadruplets: the **Q**uadruplets in the **S**mall wedges, the innermost (**1**) of the three, and for both **P**ivot and **C**onfirm wedges.

Internally, each sTGC layer consists of a plane of wires sandwiched between

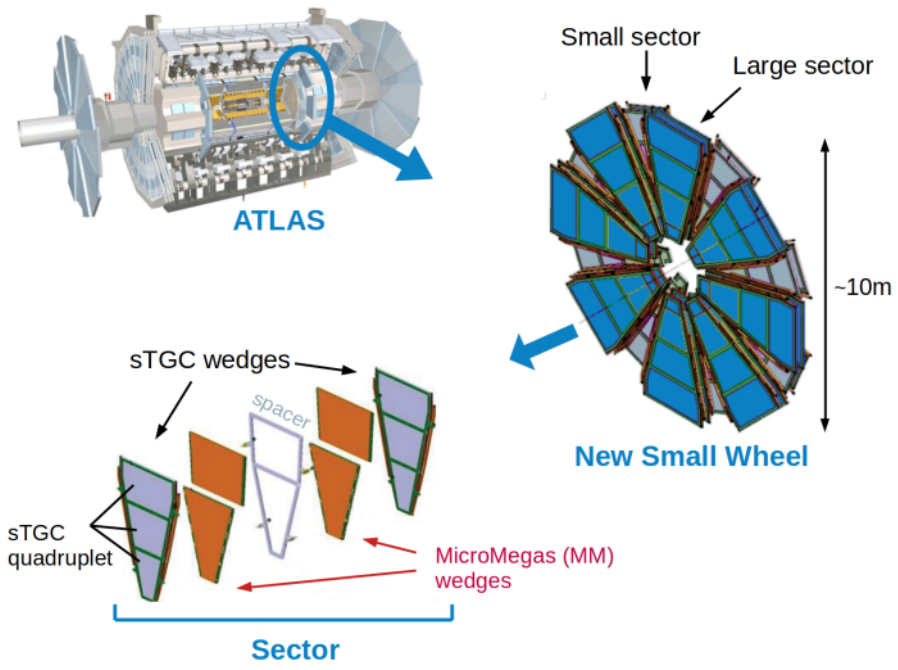

Figure C.2: Schematic diagram showing the structure of a NSW sector [54].

two cathode planes, where one of the cathodes is subdivided into large rectangular pads, and the other into thin strips, which give the sTGC its name (small-strip Thin Gap Chambers). The signals that are produced by the pads and strips on each layer on each quad get collected by their corresponding on-sector Front End Boards (FEBs). There is one FEB per layer per quad for the pads (pad-FEBs, or pFEBs), and same for the strips (strip-FEBs, or sFEBs), for a total of 24 pFEBs and 24 sFEBs per sector. The FEBs on each sector are controlled by another on-sector electronic board, the L1DDC, located on the outermost quadruplet (QS3 on small sectors and QL3 on large sectors). These L1DDCs are connected to all the FEBs of a single layer, one L1DDC per FEB type, so one L1DDC for all the pFEBs of a layer, and one L1DDC for all the sFEBs of a layer, for a total of 16 L1DDCs per sector. Another set of electronics are located on the back of the wheel itself, off-sector, in the so-called "Rim crate". This set of electronics handles the trigger response of the sTGCs, they are:

- Pad Trigger Board, which receives the signals from the pad FEBs, and then sends back the signal to the strip FEBs for them to be read out
- 8 Routers receive the signal back from the strip FEBs (one for each sector

layer)

- Rim-L1DDC controls the other boards in the rim crate and connects to the muon readout system.

One of these rim crate exists for each of the 16 sectors of a single wheel, so for both wheels A and C a total of 32 rim crates had to be populated and connected. Finally, a small fiber box (FSB) located on top of the rim crate received fiber connections from the 16 L1DDCs, and from the 10 boards on the rim crate, and routes them to a large fiber box (FLB) located on the upper side of the wheel.

Figure C.3: Rim crate with everything connected and with proper cable management. On top the small fiber box can also be seen.

After a sector was mounted on the wheel, all the services of its sTGCs had to be connected, which included:

- Water for the cooling of the electronics

- Gas that would circulate inside the chambers to enable muon detection.
- High voltage connection for the wires inside the chambers
- Rim crate had to be populated with its electronics, with thermal paste connections to ensure proper cooling during use
- Low voltage connections to power the electronics in the wedges as well as the rim crate electronics
- Coaxial cables from wedge FEBs to the rim crate electronics
- Fiber cables from FEBs to rim crate fiber boxes

Of these tasks, the water and gas connections were done by the technicians at building 191 (b191), while the rest were performed by me and the rest of my team. The cables had to not only be connected, but the proper cable routing from the wheel to the rim crate, as well as rim crate cable management had to be applied to ensure that the wheels respected the envelope restrictions within ATLAS, as seen in Figure C.3. After all the connections were finished, the sectors had to be tested to ensure that all the connections were made correctly, and in case there were issues, the cables had to be checked and replaced if necessary. These tests were also performed by me and my team, and included:

- Pulser tests, where internally produced pulses were sent to all pad, strip and wire channels on the boards to align the phases of the VMM chips on the FEBs.
- Baseline tests, where the baseline levels of the channels were measured to ensure that they are within tolerance, to identify dead channels, and to make a general check on the connections.
- Thresholds and trimmers, where the channels are calibrated to ensure they all have the same sensitivity.
- Noise tests, where after the channels have been calibrated, a pulser test is repeated, only this time the internal pulse generation is disabled.

I worked on the commissioning of both wheels A and C. After wheel A was completed (see Figure C.4), most of my team moved to work on the integration of wheel A into ATLAS, while I stayed behind to commission wheel C and help train the new people that had joined to work on commissioning. After wheel C

was completed, I rejoined the integration team in the underground detector cavern, where I worked for a couple of months inside the detector, making sure that all the connections had survived the move from b191 to the ATLAS cavern, repeating tests, replacing broken cables, reconnecting loose boards, and more.

Figure C.4: ATLAS team after the installation of the last sector of wheel A [55].